SAPIENZA
UNIVERSITÀ DI ROMA

On the Development of the Convective Boundary Layer in a Shear-Free Thermally Forced Stably Stratified Fluid Setting:

a 2D and 3D experimental investigation using image analysis techniques coupled with temperature measurements

Facoltà di Ingegneria
Dipartimento di Idraulica Trasporti e Strade
Dottorato in Ingegneria Idraulica XXII CICLO

Candidato
Valentina Dore
n° matricola 791692

Tutor
Prof. Antonio Cenedese

Co-tutor
Dott. Ing. Monica Moroni

Acknowledgments

This thesis would not have been possible without the support of many people.

I am heartily thankful to my supervisor Prof. Antonio Cenedese and my co-supervisor Dr Monica Moroni, whose encouragement, guidance and support from the initial to the final level have been of fundamental importance for the completion of the project.

I am deeply grateful to all the past and present PhD and visiting students in the Fluid Mechanics Laboratory at Sapienza University for their sharing, friendship and support. A special thank to Martin for his great help in taking measurements.

Many thanks to the whole Lab staff, researchers, assistants, and technicians for their advices, suggestions and contributions. Without all of them the experience in the lab would not have been so pleasant and impressive.

Lastly, I would like to offer my acknowledgements to all of those who supported me in any respect during all these years. I remain indebted to my family, my friends and my partner for their unconditional love and understanding.

Introduction

The motion of buoyancy driven plumes is, on all scales, the most common heat and momentum transfer mechanism in geophysical flows, well known as Free Convection. Similarly, density stratification due to heating inequalities is also an ordinary scenario in nature. Free Convection phenomenon coupled with a density stratified fluid setting leads to the so-called Penetrative Free Convection (PFC).
When a fluid, in static equilibrium, is stably stratified a thermal forcing can produce an unstable configuration ensuing internal waves formation of increasing amplitude. If the perturbation is strong enough, it can definitely erode the initial stratification and cause the motion of turbulent buoyant updrafts, dome-shaped, compensated by denser downdrafts. The entrainment phenomenon occurring at the interface between the turbulent and non-turbulent region justifies the penetrative feature of convection and causes the non linear growth of the Convective Boundary Layer (CBL) of well mixed fluid against the adjacent stably stratified region.

In addition to the wide engineering applications, the environmental impact mostly motivates PFC studies. The upper lakes and oceans, under calm conditions, usually exhibit a continuous, moderately stable density distribution. Turbulent convective flow can be generated both by the free-surface cooling and wind shear-stress, eroding the stable stratification on a daily or seasonal time scale (Kato and Phillips, 1969; Imberger and Ivey, 1991). Domes with large downward velocities are generated at the free surface, balanced by updrafts with lower velocity but larger area. Because of the relatively rapid mixing, the density distribution is approximately uniform in the upper layer and it deepens with time as a result of the entrainment and erosion of the underlying denser water. An analogous phenomenon is observed in the lower troposphere when surface heating due to solar radiation results in a growing unstable layer adjacent to the ground which replaces a nocturnal inversion from below. In this case, the initially stable environment near the ground is affected by convection characterized by relatively narrow and fast plumes of rising horizontal surfaces balanced by larger regions of downward slower motion (Deardorff, 1979; Stull, 1988). Resulting internal waves generated within the stable layer take place at or below the Brunt-Väisälä frequency, which is related to the vertical temperature gradient (Stull, 1976). Penetrative convection also occurs in stars (Miesch et al., 2000). Stars of mass less than approximately one solar mass present a radiative core and a convective envelope; more massive stars have a

convective core and a radiative envelope. Turbulent motion in the convective region may penetrate the stably stratified radiative regions.

In nature, the dynamics of the CBL influences the transport and mixing features of a given stratified fluid-body. The amount of materials being mixed due to penetrative convection is a crucial issue as in water or air quality monitoring and forecast as in stellar evolution theories with important implications both in environmentally-friendly studies and in astrophysics. Focusing on the environmental aspect, the pollutant dispersion is a matter of particular importance. On one hand, mixing processes inside the CBL help increasing dispersion with some positive consequences: the concentration of potential harmful pollutants in high risk zones tends to decrease, the turnover and the redistribution of vital substances, like oxygen and nutrients, is guaranteed; the latter plays a major role in large water bodies. These advantages are essential for the safety of populations living close to urban or industrial areas, or for preserving coastal human activities and ecosystems. On the other hand each pollutant, released inside the CBL mainly by human activities, remains confined inside it because of the interface with the non-turbulent region, which acts as a barrier for outward transport. Considering the proximity of the CBL with biosphere, a deeper insight into dispersion and entrainment processes appears mandatory either for engineering design or for monitoring purposes.

The applications discussed above motivated the large amount of investigations on CBL development in a continuously and linearly stratified fluid setting. The topic has been extensively studied during field campaigns, in laboratory models, with bulk convective boundary layer models and by numerical simulations. Fedorovich *et al.* (2004) present a nice and complete review of the literature published on this issue. It appears there is a lack of consensus about the dependence of integral parameters of convective entrainment (in particular the CBL growth rate) on the initial stratification strength and convective phenomenon evolution.

Driven by all these premises the main aims of the present research are related to better understanding dispersion of a passive scalar inside the CBL with a lagrangian and non-local approach. When turbulent convection occurs, in fact, dispersion is mostly due to transport by large organized structures while molecular diffusion can be neglected. Given this assumption, a non local approach based on a fully advective-like behaviour of the tracer is necessary and a lagrangian description of flow may be more suitable (Stull, 1993). Moreover, the knowledge of the horizontal and vertical extension of the structures dominating the flow field appears to be mandatory. Furthermore, turbulence is fully three-dimensional on the scales of motion characterising the phenomena in nature. In order to better understanding and likely describing the evolution of turbulent structures inside the convective layer, a three dimensional experimental technique is strongly required. In the present work a laboratory model is designed to reproduce the penetrative shear-free convection phenomenon, to predict the CBL growth as a function of initial and boundary conditions, to compute the dimensions of turbulent structures, to understand the interaction between the turbulent and non-turbulent regions and to describe the fate of a passive tracer dissolved within

the fluid phase through a transilient turbulence approach applied to a lagrangian framework. Field experiments aimed at measuring the turbulence budget of the CBL have shown that the mechanical generation of kinetic energy by wind shear is often confined close to the heat source supporting the validity of laboratory models in which no wind is present (Deardorff et al., 1969, Deardorff, 1970). According to this assumption, the similarity proposed by Deardorff (1970) is employed here to compute scaling parameters and to make results comparable. Through normalizing the quantities measured at different stages of the experiment, the phenomenon can be considered as a succession of steady states, according to an evolution of the variables of interest that may be defined quasi-steady (Cenedese and Querzoli, 1994). The experimental apparatus employed to run the experiments is the same as in Cenedese and Querzoli (1994), Querzoli (1996), Cenedese and Querzoli (1997) and Moroni and Cenedese (2006). The spatial resolution of velocity data is largely increased here by means of 2D and 3D image analysis techniques (Feature Tracking, FT, and 3D Particle Tracking Velocimetry, 3D-PTV) used instead of Laser-Doppler Anemometry or 2D Particle Tracking Velocimetry as in Cenedese and Querzoli, 1994; Querzoli, 1996 and Cenedese and Querzoli, 1997. Moreover the photogrammetric 3D-PTV here applied allows fully three-dimensional descriptions of both the Eulerian velocity field and Lagrangian particle trajectories for a more likely understanding of the phenomenon than through the 2D approach used in Moroni and Cenedese (2006). Furthermore, the combined use of thermocouples and flow visualization techniques allows cross-validating different methods to estimate the evolutions of the key parameters (Moroni and Cenedese, 2006; Dore et al., 2009a) and the plume characteristic dimensions (Dore et al., 2009b).

Two different experimental arrangements were set-up, 2D and a 3D models. A large set of data were firstly acquired using a 2D model and employing FT. The preliminary investigation was mainly focused on better understanding the physics of the phenomenon, finding a time scaling law, testing different methods to compute the variables of interest and comparing results with classical methods found in literature. FT algorithms are based on pixel luminosity intensity gradients distributed within each image, recalling the "image brightness constancy constraint" and assuming the hypothesis of tracer particles behaving as Lambertian surfaces. The intensity gradients are likely distributed around the particle border and those are tracked frame by frame. The issues of properly separating a particle from the image background and computing its centroid are overcome (Moroni and Cenedese, 2005). FT is suitable for analyzing any particle density images and it does not require a priori velocity estimates to identify particle trajectories. The technique employed for this investigation implements a pure translation model (Miozzi, 2004; Moroni and Cenedese, 2005; Miozzi et al., 2008).

When 2D techniques are employed to detect the velocity field, the flow is illuminated with a thin light sheet and only the velocity components within this sheet can be evaluated. Driven by the idea that only a fully three-dimensional technique can significantly improve our laboratory model in term of a more likely description of free convection structures we run a second set of experiments, by using a stereoscopic

arrangement of cameras focused on an illuminated volume. Although some methods do exist for reconstructing 3D velocities in a point (3D laser Doppler Anemometry; Hinsch and Hinrichs, 1996) or plane (3D stereo-PIV; Stuer et al., 1999), only a fully 3D technique based on the illumination of a flow volume rather than a flow sheet will give the information needed to construct the instantaneous 3D velocity fields. A number of imaging-based measurement techniques exist for determining 3D velocity fields in an observation volume. Among these are:

- *"scanning" techniques (Guezennec et al., 1994; Moroni and Cushman, 2001);*
- *holographic techniques (Hinsch and Hinrichs, 1996; Zhang et al, 1997);*
- *defocusing techniques (Willert and Gharib, 1992);*
- *photogrammetric techniques (3D-PTV; Kasagi and Nishino, 1990; Maas, 1992).*

We will focus on 3D-PTV which is a 3D extension of the 2D particle-tracking methods. 3D-PTV is based on reconstructing 3D trajectories of reflecting tracer particles through a photogrammetric recording of image sequences. The 3D particle trajectories obtained can be used to calculate the 3D velocity field. Because the actual path of the particles is analyzed, particle-tracking techniques are generally more accurate than PIV-based techniques (Cowen and Monismith, 1997; Moroni and Cenedese, 2005). The 3D-PTV optical system has been designed with the following capabilities: image a volume far away the boundary walls, lengthen the trajectories, and improve the accuracy of the procedure through a careful test on synthetically generated data. A physically-based photogrammetric calibration of the stereoscopic arrangement was employed and its accuracy tested. The effects of multimedia geometry on calibration parameters are taken into account. The combination of image- and object-space based information was employed to establish the correspondences between particle positions (structure from stereo reconstruction). A particle tracking algorithm was then employed to reconstructed 3D trajectories.

The thesis is organized as follows. The first three chapters are focused on describing the state of art in term of:

1. *physical knowledge of the phenomenon and the governing equations;*
2. *existing methods for detecting the variables of interest (i.e. the spatial extension of convective structures) and similarity issues;*
3. *motivations and broader impact of the research mostly due to its environmental implications.*

Chapter 4 presents the description of the experimental set-up and the two different arrangements used for 2D and 3D measurements. The results discussion represents the core of the manuscript from chapter 5 to 7 and it is subdivided as follows:

1. *results of 2D model are discussed in chapter 5;*
2. *results of synthetic generated data for the 3D model are discussed in chapter 6;*
3. *In chapter 7 results of real 3D data are discussed and comparisons with other experimental investigations and a LES model are presented.*

Finally conclusions are reported in the last section.

Symbol significance

Symbol	Definition	Unit
A	Constant	
b	buoyancy	m/s^2
B	Buoyancy flux	m^2/s^3
c	Specific heat	J/(kg K)
C	concentration	kg/m^3
C	Concentration matrix	kg/m^3
d	Horizontal scale	m
D	Diameter of particles	m
D_A	Dissipation factor	
e	TKE/m	m^2/s^2
g	Gravity acceleration	m/s^2
Gr	Grashof number	
h	Generic height	m
H	Reference height	m
K	Tensor of turbulent dispersivity	
L	Lagrangian integral time scale	s
m	mass	Kg
M	Mixing potential	
N	Brunt Väisälä frequency	1/s
Nu	Nusselt number	

p	Joint probability density function	
P	pressure	Pa
P	Transilient Matrix	
Pr	Prandtl number	
q	Kinematic heat flux	m K/s
$\mathbf{r}=\mathbf{x}_{i+1}-\mathbf{x}_i$	Displacement vector	m
R	Correlation coefficient	
Ra	Rayleigh number	
Ri	Richardson flux number	
R	Gas constant	
S	Generic scalar	
t	Time	s
T	Temperature	K
u	Velocity vector i=1,2,3	m/s
w	Vertical velocity component	m/s
x	Position vector	m
V	Volume	m^3
z	Cartesian vertical direction	m
z_i	CBL height	m
Greek symbols		
β	Thermal volumetric expansion coefficient	1/K
γ	Temperature gradient	[K/m]
δij	Kronecker delta	
Δ	Interval	
ε	dissipation	
θ	Potential temperature	K
κ	Thermal diffusivity	m^2/s
K	Thermal conductivity	W/(m K)

μ	Dynamic viscosity	Pa s
ν	Kinematic viscosity	m^2/s
ν_s	Diffusivity for the scalar S	m^2/s
ν_t	Turbulent viscosity	m^2/s
ρ	Density	kg/m^3
σ	Velocity standard deviation	m/s
Up-scripts		
‘	Parameter fluctuation part	
-	Parameter mean part	
~	Deviation from hydrostatic equilibrium	
^	Non-dimensional parameter	
Subscripts		
*	Convective scaling parameter (function of q_s)	
0	Reference variable	
c	critic	
C	Cold temperature	
C	concentration	
i, j, k	Vector generic component i=j=k=1,2,3 (or matrix indexes)	
e	entrainment	
f	Final value	
n_w	Near wall scaling parameter (function of q_s)	
o	Near wall scaling parameter (function of θ)	
P	constant pressure	
pa	particle	
θ	Convective scaling parameter (function of θ)	
s	Bottom surface	
t	Top boundary	

V	Constant volume
W	Vertical velocity component
W	Warm temperature

1

The Onset of Instability for Thermally Forced Stratified Fluids

1.1. Penetrative Convection

A stratified fluid consists of fluid parcels of various densities. Stratification can be induced for example by temperature, pressure or salinity gradients, which tend, under gravity (rotation effects are neglected), to arrange themselves into layers of decreasing density upward.

If the fluid system is in static equilibrium, the lack of motion requires the absence of lateral forces and, consequently, horizontal homogeneity establishes. The stratification is then purely vertical. The stratification is stable if heavier fluid particles lay under lighter ones, and the fluid tends to persist in its equilibrium state according to Le Chantelier's principle; the inverse stratification can imply, on the contrary, unstable conditions, and the system tends naturally to overturn in order to reach stability (Fig 1.1).

We can simply verify this intuition using both mathematical and physical arguments. We can imagine, in fact, to move upward (or downward) a volume V of a vertically stratified fluid, from a layer defined by a reference height and density (respectively z and $\rho(z)$) to a layer defined by z+h (or z-h) height and $\rho(z+h)$ (or $\rho(z-h)$) density. If the fluid is uncompressible, it can be assumed that parcels at the new level maintains their original density even if the pressure has changed.

At that new height, because of the density anomaly with the environment, the fluid parcel feels a buoyancy force equal to:

$$g[\rho(z+h)-\rho(z)]V \tag{1.1}$$

Applying the Newton's law we have:

$$\rho(z)V\frac{d^2h}{dt^2} = g[\rho(z+h)-\rho(z)]V \tag{1.2}$$

(A)  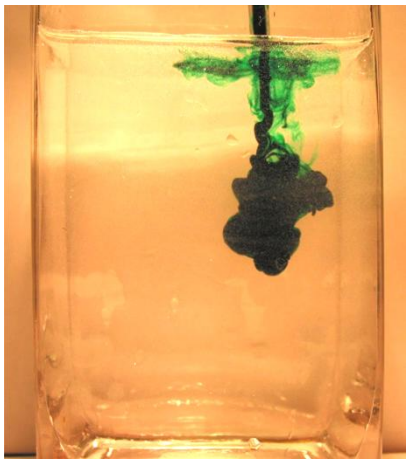 (B)

Fig. 1.1 (A) Buoyant plume of dyed alcohol rises through an interface between corn syrup and water (Copyright © Jessica Todd, College of Engineering, University of Colorado, Boulder, 2002. All rights reserved.) (B) Negative buoyancy experiment (Copyright © Cody Taylor and Gala Camacho, University of Colorado, Boulder, 2005. All rights reserved)

Approximating the density difference in the right side of eq. 1.2 with a Taylor expansion and rearranging :

$$\frac{d^2h}{dt^2} - \frac{g}{\rho_0}\frac{d\rho}{dz}h = 0 \qquad (1.3)$$

Two different situations can occur according to the sign of the density gradient:

- If $\frac{d\rho}{dz}$ is negative, the solution is a wave equation with frequency equal to $N = \sqrt{-\frac{g}{\rho_0}\frac{d\rho}{dz}}$ (called Brunt- Väisälä frequency); physically, it means that the perturbation of the original equilibrium brought by the fluid parcel displacement, produces a natural motion of fluid, driven by buoyancy forces, toward its original level. Upon reaching that equilibrium stage, inertia forces push particle further away from it, resulting in an oscillatory movement (internal waves) around its equilibrium position with a frequency, function of the stratification gradient. This solution proves the stability of stratification.
- If $\frac{d\rho}{dz}$ is positive, the solution of the equation corresponds to an exponential growth. In this case, the fluid parcel, after the perturbation, moves further

and further away from its original position, proving the instability of the initial stratification. Under a small and time limited forcing, all the fluid parcels participate in a general overturning, until a new, more stable, stratification is reached. If, however, a permanent forcing is applied (as heating from below or cooling from above), the fluid will maintain a constant agitation, resulting in a process called convection.

In general, convection mechanism refers to the motion of vertical turbulent plumes or domes, which may occur when a quiet stratified fluid is submitted to buoyancy forces caused by a permanent energy input, like heat transfer or mechanical forces. When a fluid, in equilibrium, is stably stratified the external forcing can produce an unstable configuration resulting in the increasing of internal waves amplitude, and, if it is strong enough, it can definitely erode the stratification, involving a fluid volume of increasing thickness. The entrainment phenomenon justifies the penetrative feature of convection and causes the growth of the so-called convective boundary layer (CBL) against the adjacent stable stratified layer.

As described above, convection can easily arise when the equilibrium of the fluid occurs in an un-stably stratified setting, in this case the fluid goes along with perturbation and turbulent motion arises even for very small forcing. If again the so formed domes encounter stably stratified layers, thanks to the entrainment process described above, turbulence can penetrate inside it and propagate for increasing levels, resulting in penetrative convection.

We will focus our investigation on the study of the onset of thermal instability in horizontal layers of fluid, initially stably stratified, heated from below. We intentionally neglect the effects of rotation and magnetic field, which introduce other conflicting tendencies to which the fluid can be subjected. We want to consider, in fact, the phenomenon at the micro-scale of motion, where turbulence has a dominant role.

Consider then a fluid in its initial condition of stable stratification characterized by a certain temperature gradient. An adverse temperature gradient between a hot surface placed at the bottom and the layer of fluid in touch with it is maintained by heating the underside (Fig. 1.2). The temperature gradient thus maintained is qualified as adverse if, on account of thermal expansion, the fluid at the bottom will be lighter than the fluid of the layer immediately above; and this is a top- heavy arrangement which is potentially unstable. Because of the instability there will be a tendency of the fluid to redistribute itself and remedy the weakness in that arrangement. However, this natural tendency of the fluid is inhibited by its own viscosity. In other words, we expect that the adverse temperature gradient must exceed a certain value before the instability can manifest itself. We can describe the changing from stable to unstable condition through the numerical value of the Rayleigh number, a non-dimensional parameter representing the relation between convection, driven by buoyancy and conduction driven by viscosity (see Rayleigh Benard problem in Chandrasekhar, 1981).

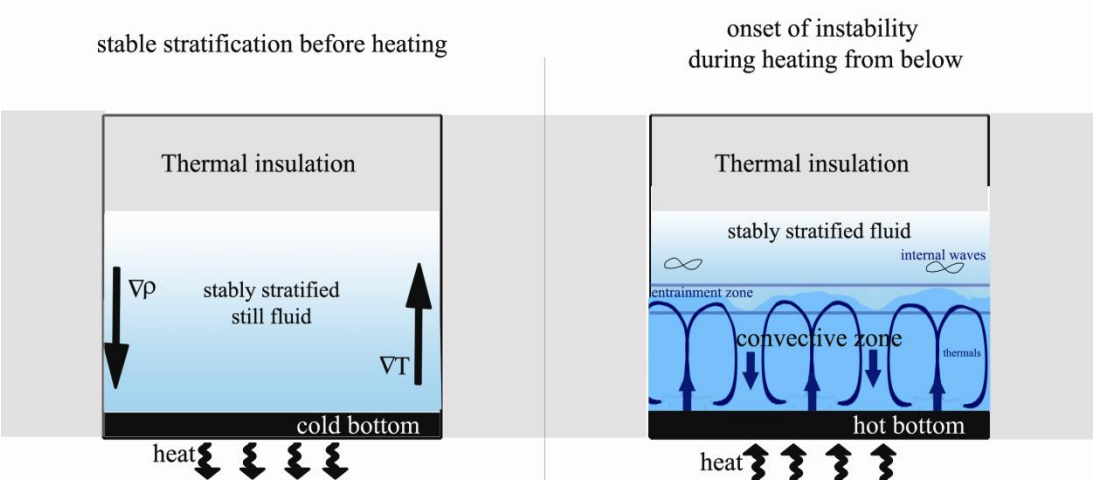

Fig. 1.2 Sketch of the fluid setting studied. The fluid is stably stratified in its initial condition. Then an adverse temperature gradient between a hot surface placed at the bottom and the layer of fluid in touch with it is maintained by heating the underside.

Define the Rayleigh number as:

$$\mathrm{Ra} = \mathrm{Gr}\,\mathrm{Pr} = \frac{g\beta(\Delta T)H^3}{k\nu} = \frac{t_\kappa t_\nu}{t_g{}^2} \tag{1.4}$$

where:

$$\mathrm{Ra} = \mathrm{Rayleigh\,number} = \frac{\mathrm{convection}}{\mathrm{conduction}}$$

$$\mathrm{Gr} = \mathrm{Grashof\,number} = \frac{\mathrm{buoyancy}}{\mathrm{viscosity}} = \frac{g\beta(\Delta T)H^3}{\nu^2}$$

$$\mathrm{Pr} = \mathrm{Prandtl\,number} = \frac{\mathrm{momentuum\ \ diffusivity}}{\mathrm{thermal\ diffusivity}} = \frac{\nu}{k}$$

$$t_\kappa = \mathrm{thermal\,diffusion\ time} = \frac{H^2}{\kappa}$$

$$t_\nu = \mathrm{visosity\ diffusion\ time} = \frac{H^2}{\nu}$$

$$t_g = \mathrm{buoyancy\,time} = \sqrt{\frac{H}{g\beta\Delta T}} = \frac{1}{N}$$

$H = \mathrm{characteristic\ length\ (layer\ depth)}$

$\Delta T = \mathrm{temperature\,difference\ over\ the\,horizontal\ layer\,of\,thickness\ H}$

To study the onset of instability according to the Rayleigh-Benard problem we can compute Ra relatively to the layer closer to the hot surface. Instability arises when Ra exceeds a certain critical value Ra_C, according to which convection dominates over conduction. For rotating fluids, the effect of viscosity on the convection mechanism is reversed. Therefore, an inviscid fluid in rotation should be expected to be thermally stable for all adverse temperature gradients. Indeed only without neglecting viscosity, thermal instability can arise and the Taylor-Proudman theorem [1] can be violated (Chandrasekhar, 1981).

1.1.1. The governing equations

The approximation of Oberbeck (1879) and Boussinesq (1903)[2] is used when the density is nearly constant but density differences exist due to temperature changes, causing an imbalance of the hydrostatic equilibrium. Such a situation is verified in convection problems (Feireisl and Novotny, 2007).
According to these approximations and neglecting Coriolis acceleration we can write the system of the governing equations at the turbulence scale, based on the classical balance equations of fluid dynamics:

1. $$\begin{cases} P = \rho R T = P_0 + \tilde{P} & \text{gas} \\ \rho \cong \rho_0 (1 - \beta(T - T_0)) = \rho_0 + \tilde{\rho} & \text{liquids} \end{cases}$$ State equation (1.5)

2. $$\frac{\partial u_i}{\partial x_i} = 0$$ Mass conservation (Continuity equation) (1.6)

3. $$\frac{\partial u_i}{\partial t} + u_j \frac{\partial u_i}{\partial x_j} = -g \frac{\tilde{\rho}}{\rho_0} \delta_{i3} - \frac{1}{\rho_0} \frac{\partial \tilde{P}}{\partial x_i} + \nu \frac{\partial^2 u_i}{\partial x_j^2}$$ Momentum budget (Navier Stokes) (1.7)

[1] The Taylor-Proudman theorem states that in an inviscid and homogeneous fluid that is steadily rotated with a high Ω, the fluid velocity will be uniform along any line parallel to the axis of rotation and the flow can be considered two-dimensional. The theorem is valid for a small Rossby number.

[2] Newtonian fluid; and $\frac{\partial \rho(\text{or } \mu, \kappa, \beta, c_v)}{\partial t} << \frac{\partial u_i}{\partial t}$; $\frac{\partial \rho(\text{or } \mu, \kappa, \beta, c_v)}{\partial x_j} << \frac{\partial u_i}{\partial x_j}$

4. $\frac{\partial T}{\partial t} + u_i \frac{\partial T}{\partial x_i} = K \frac{\partial^2 T}{\partial {x_i}^2} + \text{source} - \text{sink}$ [3] Heat budget (1.8)

5. $\frac{\partial S}{\partial t} + u_i \frac{\partial S}{\partial x_i} = \nu_s \frac{\partial^2 S}{\partial {x_i}^2} + \text{source} - \text{sink}$ Generic scalar budget (humidity, salinity, concentration…) (1.9)

The above equations are written in terms of density and pressure deviations ($\tilde{\rho}(x,y,z,t), \tilde{P}(x,y,z,t)$) from the hydrostatic equilibrium ($\rho_0(z), P_0(z)$), which is the reference state for the fluid at rest.

In the kind of problem described in the previous section, the fluid is confined between two horizontal planes, in which certain boundary conditions must be satisfied. First of all, regardless of the nature of these boundary surfaces, we must require both at the bottom (z=0) and top boundaries ($z=z_t$):

$$u_3 = 0 \quad \text{for } z = 0 \text{ and } z = z_t$$

There are two further boundary conditions, which depends on the nature of bounding surfaces:

- rigid surface condition, on which no slip condition occurs, i.e.
  $u_1, u_2 = 0$; (thus eq. 1.6 become $\frac{\partial u_3}{\partial z} = 0$);
- free surface condition, on which no tangential stresses act, i.e.
  $\frac{\partial u_1}{\partial z} = \frac{\partial u_2}{\partial z} = 0$; (thus eq. 1.6 become $\frac{\partial^2 u_3}{\partial z^2} = 0$);

[3] Potential temperature θ instead of absolute temperature T is often used for practical problems. The potential temperature of a parcel of fluid at pressure P is the temperature that the parcel would acquire if adiabatically brought to a reference pressure P_0 (usually 1 atm). For water (or when the density changes as a function of pressure can be neglected), it approximates to the absolute temperature and for air is defined as:

$$\theta = T\left(\frac{P_0}{P}\right)^{\frac{R}{c_p}}$$

The equations written above form a closed system but an analytical solution is not known.

Instead of considering instantaneous variables, we can write the same equations for mean variables after using the Reynolds decomposition, based on the stochastic interpretation of turbulence, according to which variables defining the spatial-temporal evolution are random variables definable through central moments.

Thus, the system of equations becomes:

1. $$\begin{cases} \overline{P} = \rho R \overline{T} = P_0 + \tilde{\tilde{P}} & \text{gas} \\ \overline{\rho} \cong \rho_0 (1 - \beta(\overline{T} - T_0)) = \rho_0 + \tilde{\tilde{\rho}} & \text{liquids} \end{cases}$$ State equation (1.10)

2. $$\frac{\partial \overline{u_i}}{\partial x_i} = 0$$ Mass conservation (Continuity equation) (1.11)

3. $$\frac{\partial \overline{u_i}}{\partial t} + \overline{u_j} \frac{\partial \overline{u_i}}{\partial x_j} = -g \frac{\tilde{\tilde{\rho}}}{\rho_0} \delta_{i3} - \frac{1}{\rho_0} \frac{\partial \tilde{\tilde{P}}}{\partial x_i} + \nu \frac{\partial^2 \overline{u_i}}{\partial x_j^{\,2}} - \frac{\partial \overline{u_i' u_j'}}{\partial x_j}$$ Momentum budget (Navier Stokes) (1.12)

4. $$\frac{\partial \overline{T}}{\partial t} + \overline{u_i} \frac{\partial \overline{T}}{\partial x_i} = K \frac{\partial^2 \overline{T}}{\partial x_i^{\,2}} - \frac{\partial \overline{u_i' T'}}{\partial x_i} + \text{source} - \text{sink}$$ Heat budget (1.13)

5. $$\frac{\partial \overline{S}}{\partial t} + \overline{u_i} \frac{\partial \overline{S}}{\partial x_i} = \nu_s \frac{\partial^2 \overline{S}}{\partial x_i^{\,2}} - \frac{\partial \overline{u_i' S'}}{\partial x_i} + \text{source} - \text{sink}$$ Generic scalar budget (humidity, salinity, concentration…) (1.14)

The system is not closed because the unknowns are more than the number of equations. A closure form of the system is, therefore, necessary. Generally, the closure relations consist in the parameterization of turbulent fluxes, which appear in the equations as cross-correlation terms (second moments) ($\overline{u_i' T'}, \overline{u_i' S'}, \overline{u_i' u_j'}$). These fluxes are, in fact, unknowns, because there are no equations defining them. Otherwise, the introduction of new forecast equations for these unknown quantities brings new unknowns, represented by third moment terms. Persisting in the search of a closed system of forecast equations is then impossible, because the introduction of new

equations increments only the number and the order of unknowns toward an infinite process. The parameterization of unknowns as a function of known quantities and parameters is then the only way to have a closure. The closure, thus, is named by the highest order of moments that are retained. If for example we retain the equation of the first moment (mean value) and the second moment (cross-correlation terms) are parameterized we have a first order closure, if we retain second moments, introducing a forecast equations for them, and the third order moments are parameterized we have a second order closure, and so on.
There are substantially two classes of closure forms:

- local closure, according to which an unknown quantity at any point in space is parameterized by values and /or gradients of known quantities at the same point. Local closure thus assumes that turbulence is analogous to molecular diffusion. That closure approach is very simple, but it is not always applicable, especially to convective conditions.
- Non-local closure, according to which the unknown quantity at one points is parameterized by values of known quantities at many points in space. This assumes that turbulence is a superposition of eddies at difference scales, each transporting fluid like an advection process; the presence of large eddies structures in real convective situation implies that one space point is influenced by contributions coming from most parts of the domain.

1.1.2. Turbulent Kinetic Energy equation

When a first order local closure is employed, the cross correlation term $\overline{u_i' u_j'}$, in analogy with diffusion term, becomes:

$$\overline{u_i' u_j'} = \nu_t \frac{\partial \overline{u_j}}{\partial x_i} \tag{1.15}$$

Where ν_t is the turbulent viscosity, a function of the turbulence intensity.

The Turbulent Kinetic Energy (TKE) is directly related to the momentum, heat and scalar transport due to turbulence and thus can be considered a measure of turbulence intensity. Another equation for TKE must be introduced in addition to those in 1.1.1 in order to solve the problem.
According to the kinetic energy definition TKE is the summed velocity variances divided by two and multiplied by the mass, i.e.:

$$TKE/m = \bar{e} = 0.5\left(\overline{u_i'^2}\right) \tag{1.16}$$

Starting with the governing equations written for the mean velocities, subtracting them to those written for the total velocities in order to get equations for the fluctuations, summing velocity variances and dividing by two, we obtain the TKE budget equation:

$$\underbrace{\frac{\partial \bar{e}}{\partial t}}_{I} + \underbrace{\bar{u}_j \frac{\partial \bar{e}}{\partial x_j}}_{II} = \underbrace{+\delta_{i3} \frac{g}{\bar{T}} \left(\overline{u_i' T'}\right)}_{III} \underbrace{- \overline{u_i' u_j'} \frac{\partial \bar{u}_i}{\partial x_j}}_{IV} \underbrace{- \frac{\partial \overline{u_j' e}}{\partial x_j}}_{V} \underbrace{- \frac{1}{\bar{\rho}} \frac{\partial \overline{u_i' P'}}{\partial x_i}}_{VI} \underbrace{- \varepsilon}_{VII} \qquad (1.17)$$

Each term gives us information about the forces that contribute to the production or dissipation of turbulence:

- Term I represents the local storage of TKE. Because unstable flows become or remain turbulent, while stable flows become or remain laminar, it denotes instability if positive and stability if negative.
- Term II describes the advection of TKE by the mean wind.
- Term III is the production or consumption of TKE due to buoyancy (if the heat flux is positive, $\overline{u_i' T'}$ is a production term; if the same flux is negative, it is a dissipative term).
- Term IV is a shear or mechanical production/loss term (usually the momentum flux $\overline{u_i' u_j'}$ is of opposite sign than the mean wind shear, so the term is a production term, because it is multiplied by a negative sign);
- Term V is the turbulent transport of TKE.
- Term VI is a pressure correlation term, it describes how TKE is redistributed by pressure perturbations.
- Term VII represents the dissipation term due to the conversion of TKE into heat.

The ratio between term III and term IV gives the dimensionless quantity, known as flux Richardson number.

$$Ri = \frac{\delta_{i3} \frac{g}{\bar{T}} \left(\overline{u_i' T'}\right)}{\overline{u_i' u_j'} \frac{\partial \bar{u}_i}{\partial x_j}} \qquad (1.18)$$

According to definition of terms III and IV, flow is:

- dynamically unstable when Ri <1
- dynamically stable when Ri>1
- statically unstable when Ri <0
- statically stable when Ri >0
- neutral when Ri=0

1.2. Local and Non -Local Transport

In a multiphase chemically inert system, dispersion is principally due to:

i. Molecular diffusion
ii. occurrence of a velocity motion field
iii. heterogeneity of the fluid dynamical field due to turbulence

In a turbulent flow, like convection, molecular diffusion is negligible in comparison to advection. A passive scalar field evolves according to the general advection equation 1.14. Considering the tracer concentration per unit mass C(**r**,t) instead of a generic scalar S, neglecting molecular diffusivity and setting the sink and source terms equal zero, eq. 1.14 becomes:

$$\frac{\partial \overline{C(\mathbf{r},t)}}{\partial t} + \overline{u}_i \frac{\partial \overline{C(\mathbf{r},t)}}{\partial x_i} = -\frac{\partial \overline{u_i' C'(\mathbf{r},t)}}{\partial x_i} \tag{1.19}$$

The origin of the correlation term $\overline{u_i' C'(\mathbf{r},t)}$ is thus advective, but likewise diffusion process it causes dispersion. Considering the analogy with Fick's law, turbulent flux can be assumed (Boussinesque hypothesis) proportional to the concentration gradient, through the so-called tensor of turbulent dispersivity (**K**). The transport equation for a turbulent flow thus evolves to the following advective-diffusive appearance (Advection Dispersion Equation, ADE, 1.16), but the latter term is only due to a mathematical first order local closure.

$$\frac{\partial \overline{C(\mathbf{r},t)}}{\partial t} + \overline{u}_i \frac{\partial \overline{C(\mathbf{r},t)}}{\partial x_i} = -\frac{\partial \overline{u_i' C'(\mathbf{r},t)}}{\partial x_i} = \frac{\partial}{\partial x_i}\left(K_{ij} \frac{\partial \overline{C(\mathbf{r},t)}}{\partial x_i} \right) \tag{1.20}$$

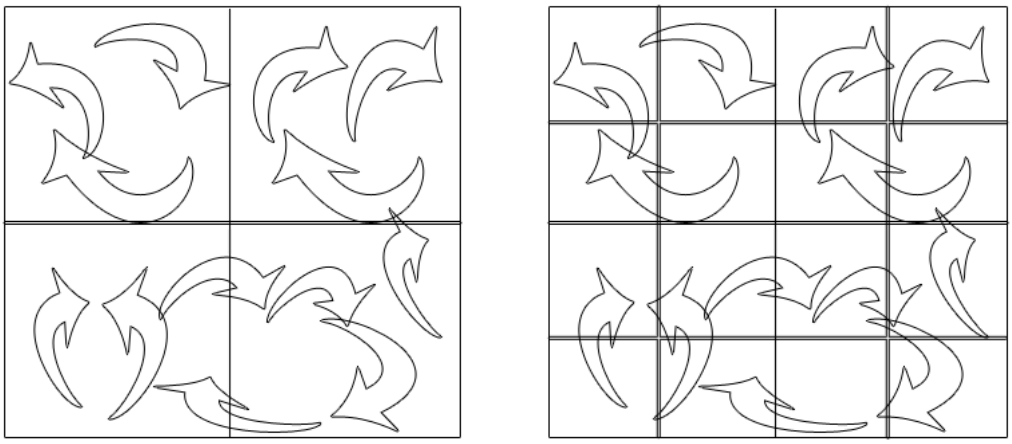

Fig. 1.3 The same turbulent flow that might appear diffusive-like (for large grid boxes) shows its advective nature when the grid resolution is made finer (Stull, 1993).

The derivation of the turbulent dispersivity in the ADE (**K**-closure) is based on the assumption of locality, according to which a tracer particle is carried to a very short distance by one eddy before being entrained in another eddy, totally uncorrelated with the first one. **K**-theory assumes small eddies cause turbulent fluxes that flow down the local mean gradient, analogous to molecular diffusion; **K** is then parameterized as a function of local mean flow variables. If the local assumption fails, as in long range correlation case (lagrangian integral scale different than zero), a non local description of turbulent transport is necessary (Fig. 1.3).

The non-local theory assumes that mixing between heights with finite separation can occur directly by fluid parcel movement, associated with coherent structures of a variety of sizes. Turbulence state is thus determined by non-local parcel movement, not by the local gradient. While smallest eddies cause diffusion, large organized eddies make the greatest contributions to turbulent advective-like transport. They are produced directly by, and gain their energy from, external forcing and mean wind shear; they hold the most turbulent kinetic energy and are usually anisotropic with sizes comparable to boundary-layer scales and external forcing.
There is ample evidence in nature of these coherent structures:

- Thermals rising from the surface have the most of their energy in the vertical, because of buoyancy, and their diameters are nearly equal the CBL depth;
- Looping smoke plumes and shear generated eddies have greater energy in the horizontal direction, because of the vertical shear due to the mean horizontal wind, and they are the size of shear domain;

- Wake eddies, like swirl of leaves or snowflakes around buildings and vehicles are the size of the obstacle.

Several non-local theories have been developed based on:

- Analytical integro-differential forms (Direct Interaction Approximation, Kraichnan 1959; Spectral Diffusivity theory, Berkowicz and Prahm 1979; Orthonormal expansions, Saffman 1969; Nonlocal or Integral turbulence Closure, Eringen 1972). In these cases closures are achieved by making a-priori assumptions about the nature or turbulence spectra. Such approaches work well for theoretical studies of idealized situations, but are of limited usefulness for non-stationary, inhomogeneous geophysical flows.
- Matrix forms (Convective circulations, Estoque 1968; Turbulence adjustment, Klemp and Lilly, 1978; Markov and non-Markov Models, Hosteleur and Opitz, 1982), which are well–suited for real cases studies and numerical modelling.
- Both analytical and discrete forms (Transilient Turbulence Theory developed by Stull and Driedonks, 1987; Asymmetrical Convective Model, Pleim and Chang 1992).

1.2.1. Transilient Turbulence Theory

The transilient turbulence theory (Stull and Driedonks, 1987) employs a Lagrangian description of transport, based on tracking of a species passively advected by the main flow, where variables are function of particle's starting location ($\mathbf{r}_0$) and time (t).

In order to estimate the scalar concentration, we can assume that it is constant on average along a trajectory, neglecting molecular diffusion. The conditional probability distribution $p(\mathbf{r}, t \mid \mathbf{r}_0, t_0)$, concerning a particle moving from $\mathbf{r}_0$ to $\mathbf{r}$ during the time interval Δt ($t-t_0$) is assumed to be equal to the statistical frequency for a number of realizations large enough. This probability obeys the Fokker Plank equation.

The average concentration $\overline{C(\mathbf{r}, t)}$ per unit mass at position $\mathbf{r}$ and time t of a concentration field of initial conditions $C(\mathbf{r}_0, t_0)$ can be estimated by summing the contributions of all particles located everywhere in the domain; so under the hypothesis of the scalar mass conservation we obtain:

$$\overline{C(\mathbf{r}, t)} = \int_V p(\mathbf{r}, t \mid \mathbf{r}_0, t_0) C(\mathbf{r}_0 t_0) dV \tag{1.21}$$

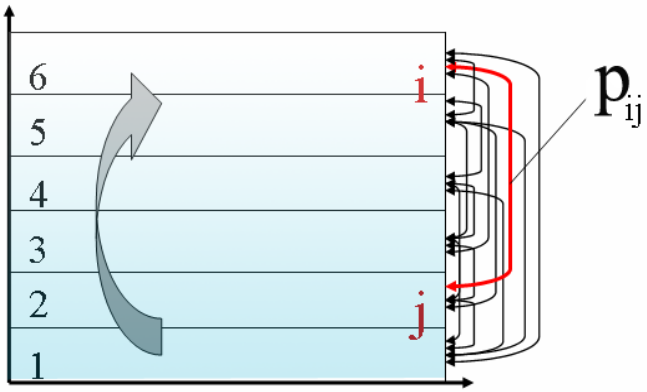

Fig. 1.4 Conceptual meaning of each transilient matrix element (p_{ij}). Using a discretization of the domain in a series of N homogeneous horizontal layers (each identified by an index i), the generic element p_{ij} refers to the fraction of fluid, which randomly moved from the j^{th} (source layer) layer to the i^{th} (destination layer) layer.

Starting from the idea that each particle can randomly move from each layer to another driven by turbulence (Fig 1.4), a discretization of the domain in a series of N homogeneous horizontal layers (each identified by an index i) may be employed. The continuous conditional probability distribution $p(\mathbf{r}, t \mid \mathbf{r}_0, t_0)$ may be replaced with its discrete form $p_{ij}(t, \Delta t)$.
Each $p_{ij}(t, \Delta t)$ term is conceived as the fraction of scalar particles, which move from layer j to layer i, transported by turbulent mixing, during the time interval Δt.
The discrete form of equation (1.17) is given by:

$$\overline{C_i(t+\Delta t)} = \sum_{j=1}^{N} p_{ij}(t, \Delta t)\overline{C_j(t)} \tag{1.22}$$

The elements $p_{ij}(t, \Delta t)$, positive and less than 1, form a square matrix, called Transilient Matrix (TM), where the row index i refers to the destination layer and the column index j refers to the source layer. Let **C** be an N-element column vector, and **P** the NxN TM. The previous equation describes a simple matrix multiplication:

$$\mathbf{C}(t+\Delta t) = \mathbf{P}(t, \Delta t)\,\mathbf{C}(t) \tag{1.23}$$

It is assumed that transported fluid parcels carry their original features of heat, moisture, tracers, and momentum components. The same TM might and should be applied to all of the state variables at any time, so the **C** column vector can be related, in a more general way, to whatever scalar parameter describing the state of each layer.

A full TM holds information on mixing process ranging from the smaller scales resolved by the grid spacing to the larger ones allowed by the domain. It includes the small eddy effects of **K**-theory plus the medium and large advective-like coherent structure effects that **K**-theory misses. It is essentially a Green's function matrix that yields the distribution of tracer as a superposition of individual distributions from many point sources.

According to its definition each element of the TM must be less or equal than 1.

In order for the TM to reflect the evolution of the tracer particle concentration per mass unit, each sub-volumes or bins used to construct it must comprises an equal mass of fluid. Thus, in a density stratified domain, the vertical extent of each horizontal layer must be inversely proportional to the density. Alternatively equally- spaced layers could be used, but now the resulting matrix must be used for describe the evolution of concentration per volume unit.

In general, if a constant mass bins discretization is employed, the sum of each row and column of the TM must be equal to one, because 100% of the fluid at each destination must have come from somewhere and all the fluid parcels initially located in each layer must go to somewhere. On the contrary, if the layer discretization does not imply mass conservation, each row sum to one but each column does not. In particular, it is verified that:

$$\sum_{j=1}^{N} p_{ij} = 1 \qquad \sum_{i=1}^{N} \frac{m_i}{m_j} p_{ij} = 1 \tag{1.24}$$

where $m_{i(j)}$ refers to the mass of layer i(j).

Elements along the main diagonal refer to fluid that has not moved from or to that layer (if then they are close to one no mixing occurs in that layer).

Moreover, the magnitude and the location of each element relative to the main diagonal give us information about how much fluid is involved in the mixing process and how faster and in which direction mixing develops. Thus elements close to the main diagonal are influenced by slow mixing upward or downward, while elements far from diagonals refer to fluid influenced by faster mixing (Fig 1.5).

Transilient turbulence theory is completely general and it can be used as a non local closure for the system of equations described in section 1.1.1.

Turbulent kinematic fluxes are, in fact easy to determine, because the transilient matrix tells us directly about the transport between grid boxes. The kinematic flux for the generic variable α across level k $\overline{u_3'\alpha'}(k)$, assuming that $\overline{u_3'\alpha'}(k=0)=0$, is given by:

$$\overline{u_3'\alpha'}(k) = \left(\frac{\Delta z}{\Delta t}\right)\sum_{i=1}^{k}\sum_{j=1}^{N} p_{ij}(\overline{\alpha_i} - \overline{\alpha_j}) = \overline{u_3'\alpha'}(k-1) + \left(\frac{\Delta z}{\Delta t}\right)\sum_{j=1}^{N} p_{kj}(\overline{\alpha_k} - \overline{\alpha_j}) \tag{1.25}$$

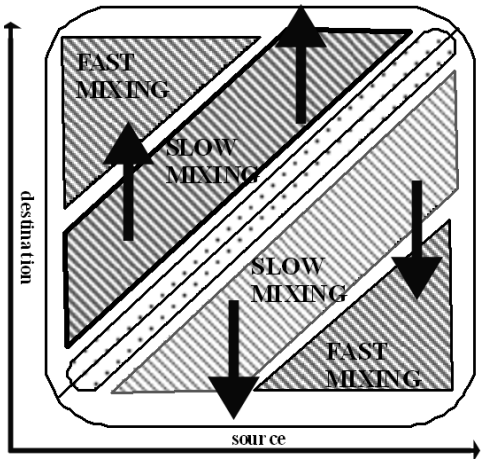

Fig. 1.5 Physical meaning of the TM. Elements close to the main diagonal are influenced by slow mixing upward or downward, while elements far from diagonals refer to fluid influenced by faster mixing.

Where Δz and Δt are respectively the spatial and temporal resolution for the matrix. The level k is defined as the border between grid boxes k and k+1. Thus, although $\overline{\alpha_i}$ is known at the centre of a grid box, $\overline{u_3'\alpha'}(k)$ is known at the edge of the grid box. This is physically consistent, because the flux represents the transport between grid boxes. Experimental modeling can produce a measurement of the TM elements directly through a statistical analysis of passive tracer trajectories, which are determined for example with Lagrangian image analysis techniques. On the contrary numerical modeling imposes a parameterization of the TM. Stull and Driedonks (1987) proposed, for example, a parameterization based on the mixing potential, deduced in analogy to the Turbulent Kinetic Energy (TKE) equation (Stull and Driedonks 1987).

1.2.2. Closure parameterization for transilient matrix

Here the parameterization of transilient matrix elements proposed by Stull and Driedonks (1987) is briefly illustrated. This closure scheme is based on a responsive approach, according to which the transilient coefficients change in response to changes in the mean flow. Substantially each time step is split into two parts, one includes all the non-turbulent dynamics, thermodynamics, boundary conditions and internal forcing, the other takes into account the response to the instabilities in the mean flow causing mixing. The amount of mixing is thus given by the transilient coefficients, which are parameterized to undo the mean flow instabilities.
Each transilient coefficient is computed through the dimensionless mixing potential between grid points i and j, M_{ij}.

$$\begin{cases} p_{ij}(t,\Delta t) = \dfrac{M_{ij}}{\|M\|} & \|M\| = \max_i \left[\sum_{j=1}^{N} M_{ij} \right] \\ p_{ii}(t,\Delta t) = 1 - \sum_{\substack{j=1 \\ j\neq i}}^{N} p_{ij} & \end{cases} \tag{1.26}$$

The potential for mixing depends on the flow instability, so a starting point for the determination of the mixing potential could be the TKE equation.
Consider equation 1.23. Neglecting subsidence, turbulent transport and pressure correlation terms, allowing for any arbitrary coordinate direction, integrating over time, normalizing the resulting equation with TKE and assuming $\Delta_{ij}\overline{\alpha} = \overline{\alpha_i} - \overline{\alpha_j}$ we have (Stull and Driedonks, 1987):

$$M_{ij} = \left[\frac{\Delta t\, L}{(\Delta_{ij} z)^2} \right] \left[(\Delta_{ij} \overline{u_1})^2 + (\Delta_{ij} \overline{u_2})^2 - g\Delta_{ij}\overline{T} \frac{(\Delta_{ij} z)}{(T\, Ri_c)} \right] - \frac{D_A \Delta t}{L} \qquad \text{for } i \neq j \tag{1.27}$$

There are three parameters in eq. 1.26 :

- the critical Richardson number, Ri_c (recommended values in real atmosphere is 0.21);
- the integral time scale L (recommended values for real atmosphere is 1000 s);
- the dissipation factor D_A (recommended values for real atmosphere is 1).

2

Modelling Criteria for the CBL and Similarity Analysis

In a heated from below fluid setting, structures characteristic of the CBL are growing domes or turrets presenting an extremely sharp interface at their top, flat regions of large horizontal extent after a dome has spread out or receded, and cusp-shaped regions of entrainment.
It is well known that those convective cells generate over a horizontal and smooth surface, if observed from a top view, tend to assume a hexagonal shape according to the Rayleigh-Benard-convection (Chandrasekhar, 1981) (Fig.2.1).
Thermal updrafts and their compensating environmental downdraft span the depth of the CBL, while the characteristic horizontal scale of thermal circulation ranges around 1.5 times the CBL height (Caughey and Palmer, 1979; Young, 1988). The spatial distribution of updraughts and downdraughts together with their characteristic horizontal and vertical dimension as a function of CBL height are important controlling factors for dispersion within the CBL, mass transfer, entrainment and gravity waves generation (Hunt and Gaynor, 1987; Young, 1988), as sketched in Fig. 2.2.
While turbulent convection is fully developing driven by buoyancy[4], four regions, evolving in time, vertically characterize the domain (Fedorovich et al., 2004), as sketched in Fig. 2.3:

- the Surface Layer near the heat source presents a negative buoyancy gradient proving that an unstable condition acts as a driving force for the

[4] Define buoyancy as $b = -g\frac{\rho - \rho_0}{\rho_0}$ where ρ_0 is the reference density. The potential temperature θ can be used instead of ρ to define buoyancy.

onset of convection; here buoyancy decreases fairly rapidly with height and heat transfer occurs mainly through conduction (SL);

- the Mixing Layer (ML), the bulk region of CBL where the mean vertical buoyancy gradients are nearly zero and the fluid is well-mixed due to turbulence;
- the entrainment zone (EZ), a density interface between the turbulent (CBL) and non-turbulent region, where buoyancy increases significantly with height;
- the Stable Layer (SbL), which is not noticeably affected by the growing CBL and the fluid maintains its initial stratification.

The first two layers characterize the CBL, while the EZ acts as an interface between the former and the non turbulent SbL. The CBL height (z_i) is thus located somewhere in the EZ and it is recognized as the characteristic scale for domes vertical dimension. Horizontal spacing of plumes is also function of z_i, but less interest has been addressed to its investigation and evolution in time. The mean and/or fluctuating part of variables, like potential temperature or vertical velocity variance, can be chosen as buoyancy or turbulence markers and their vertical profiles give us information about the presence and the vertical limits of the above listed layers (Fig. 2.3). According to a bulk approach, the ML growth mainly contributes to the value of z_i and different models have been developed to compute z_i as a function of time. The governing eqs in 1.1.1 with proper parameterizations, temperature and velocity data, or other derived variables, profiles have been exploited. In the following, a review of the most common methods is presented without claiming to be exhaustive. Scaling and similarity issues are finally discussed. In this chapter, the potential temperature is preferred rather than the absolute temperature T to ensure definitions and results generally applicable to air or water.

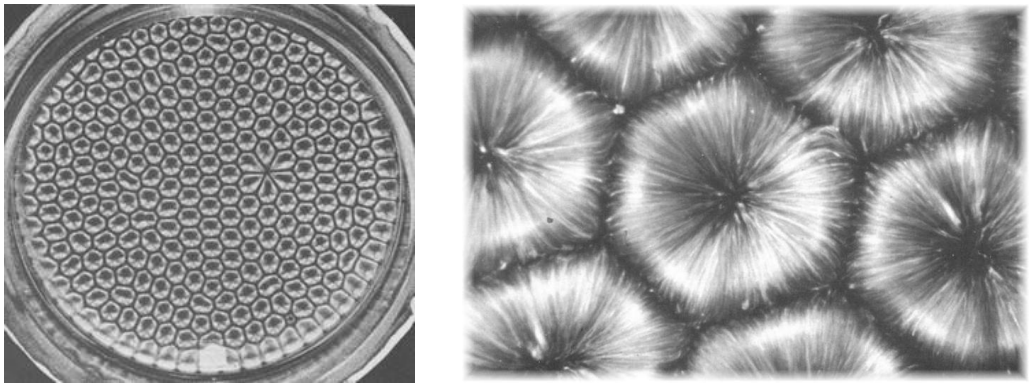

A

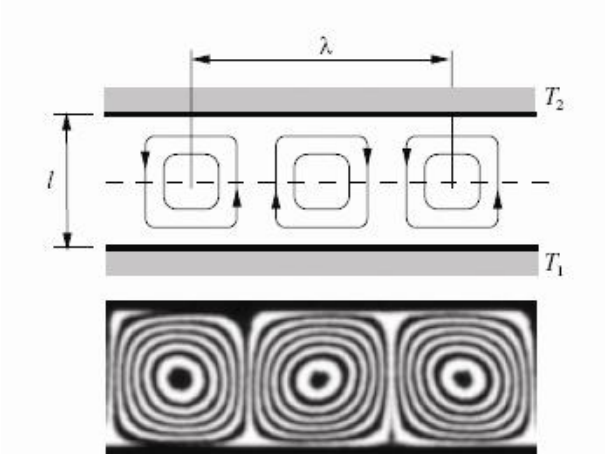

B

Fig. 2.1 A) Typical hexagonal pattern of convective cells in a Rayleigh-Benard experiment (top view) B) Cross section of typical thermal convective cells (Böhle et al., 2000).

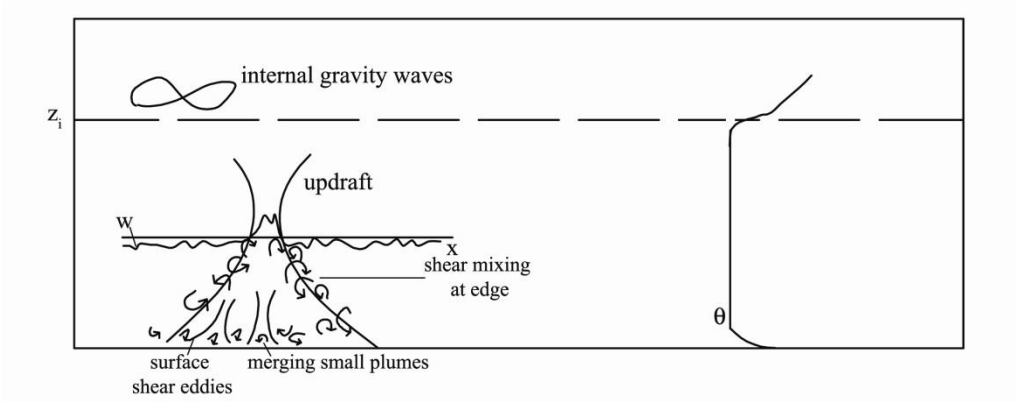

Fig. 2.2 Sketch of the typical structures for a snapshot of the penetrative convection evolution. The spatial distribution of updraughts and downdraughts together with their characteristic horizontal and vertical dimension as a function of CBL height are important controlling factors for dispersion within the CBL, mass transfer, entrainment and gravity waves generation (Hunt and Gaynor, 1987; Young, 1988).

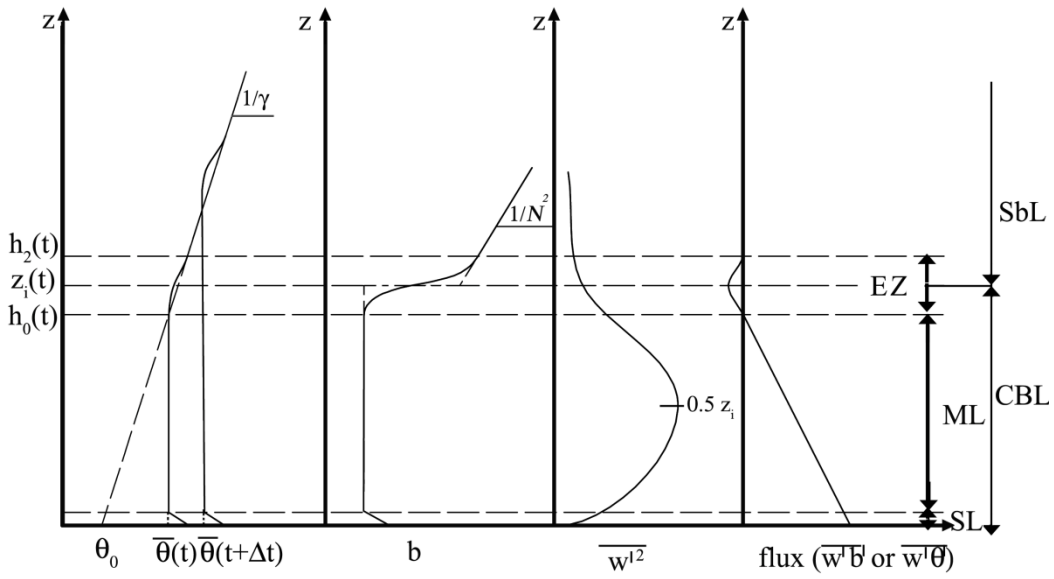

Fig. 2.3 Qualitative CBL subdivisions by observing vertical profiles of variable statistical moments. From right to left we have the typical profile of: mean potential temperature, mean buoyancy, vertical velocity variance, flux of a scalar, which can equally be heat or buoyancy (drawing not to scale).

2.1. Convective Boundary Layer Growth

2.1.1. Zero Order Jump Model

According to the zero-order jump model in Fig. 2.4, the EZ is modelled by a zero order discontinuity surface with a jump at level z_i. Moreover, neglecting the production of turbulence due to mechanical stresses, that model leads to a square root trend for the z_i as a function of time, $z_i \sim t^{1/2}$, recalling a pure thermo-dynamical model (Fedorovich, 2004). For both models in Fig.2.4, the ML height h_0 coincides with the CBL height z_i.
Considering a zero closure of the heat balance equation (eq. 1.3) and its integration over the convective bulk region we have:

$$z_i \frac{\partial \bar{\theta}}{\partial t} = \left(\overline{w'\theta'}\right)_s - \left(\overline{w'\theta'}\right)_{z_i} = q_s - q_{z_i} \tag{2.1}$$

Introducing the entrainment velocity w_e, according to the jump model sketched in Fig. 2.4 and using the parameterization for $\left(\overline{w'\theta'}\right)_{z_i}$ proposed by Driedonks (1982), we can write:

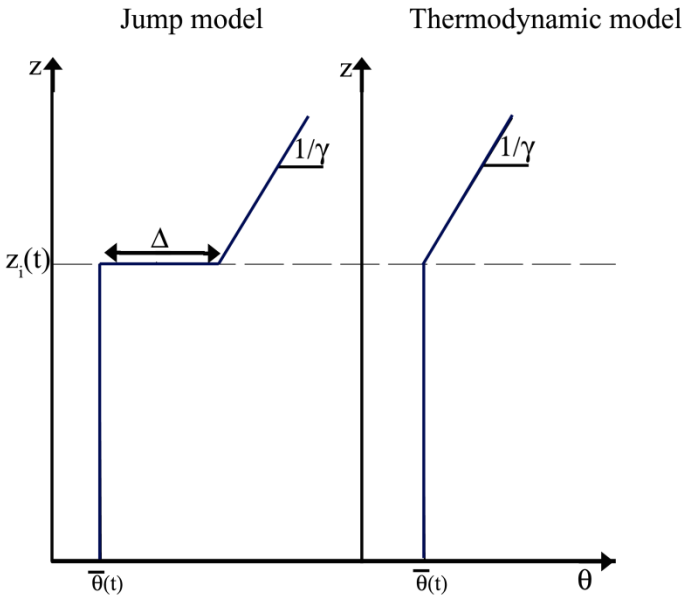

Fig. 2.4 Potential temperature profiles according to the jump and thermodynamic models. In the latter, the entrainment is neglected while in the former it is modeled with a temperature jump Δ (drawing not to scale).

$$w_e \cong \frac{dz_i}{dt} \cong \frac{\left(\overline{w'\theta'}\right)_{z_i}}{\Delta} \tag{2.2}$$

Where Δ is the temperature jump caused by the heat flux at the interface. The jump increases with the entrainment and decrease as the mean temperature of the mixing layer increase (Tennekes, 1973):

$$\frac{d\Delta}{dt} = \gamma w_e - \frac{d\overline{\theta}}{dt} \tag{2.3}$$

Moreover, the TKE budget equation simplified for the ideal model described above, neglecting the mechanical production of TKE and adding the parameterization of Batchvarova and Gryning (1991), becomes:

$$\left(\overline{w'\theta'}\right)_{z_i} \cong -A\left(\overline{w'\theta'}\right)_s \tag{2.4}$$

where $A \cong 0.2$

Batchvarova and Gryning (1991) present also a parameterization for Δ based on eq.2.4 combined with eqs 2.1, 2.2 and 2.3:

$$\Delta \cong \frac{A}{1+A}\gamma z_i \tag{2.5}$$

Substituting eqs. 2.4 and 2.5 in eq.2.2 we find z_i as a function of time:

$$\frac{dz_i}{dt} \cong \frac{(1+A)\left(\overline{w'\theta'}\right)_s}{\gamma z_i} \tag{2.6}$$

Finally, solving and integrating over the time interval t_2-t_1 we obtain:

$$z_i(t_2) \cong \sqrt{z_i^{\,2}(t_1) + \frac{2(1+A)\left(\overline{w'\theta'}\right)_s (t_2 - t_1)}{\gamma}} \tag{2.7}$$

Notice that the zero order jump model coupled with the no shear-stress assumption lead to a result analogous to the simpler thermodynamic model (Fig.2.3) which does not consider any entrainment modeling ($\Delta = 0$ and $\frac{dz_i}{dt} \cong \frac{1}{\gamma}\frac{d\bar{\theta}}{dt}$).

2.1.2. Buoyancy-based Methods

Different buoyancy-based methods are found in literature. The idea is that z_i should be the height at which the buoyancy forcing reaches its minimum. Depending on the quantity chosen as buoyancy marker, we have different methods grouped into gradient and flux methods (a review and comparison can be found in Sullivan et al., 1998). Among the others the two most common methods use respectively the potential temperature gradient and the heat flux profiles (Fig 2.3).

In the potential temperature gradient method, the CBL height z_i is defined as the vertical location of the largest increase in potential temperature, which is the vertical position of the maximum θ gradient (or whatever scalar chosen as a buoyancy marker).

$$z_i(x_1, x_2, t) = z : \frac{\partial\theta(x_1, x_2, z, t)}{\partial z} = \max imum \tag{2.8}$$

Using 2.8 the local spatial variation of z_i is preserved and the interface is followed as it evolves in time.

In the standard flux method, z_i is defined as the vertical location of the minimum heat flux averaged over the horizontal (or whatever flux used as buoyancy flux marker) that is:

$$z_i(t) = z : \overline{w'\theta'}(z) = \min imum \tag{2.9}$$

This definition of z_i was introduced by Deardorff et al., 1980 and it is often use in Large Eddy Simulations (LES). The main advantage is that z_i can be easily and unambiguously computed, but the spatial variation in the CBL height are ignored since the layer- averaged heat flux is employed.

2.1.3. Turbulence-based Methods

Second-order statistics provide a sense of overall turbulence properties of the flow. The idea here is CBL contains the greatest amount of turbulence, which vanishes in the SbL. Typical vertical profiles of velocity variances are plotted in Fig. 2.5A. Vertical velocity

variance exhibits a maximum around z=0.5 z_i, while the inflection point is located approximately at z=z_i (Deardorff and Willis, 1985; Sullivan et al. 1998).

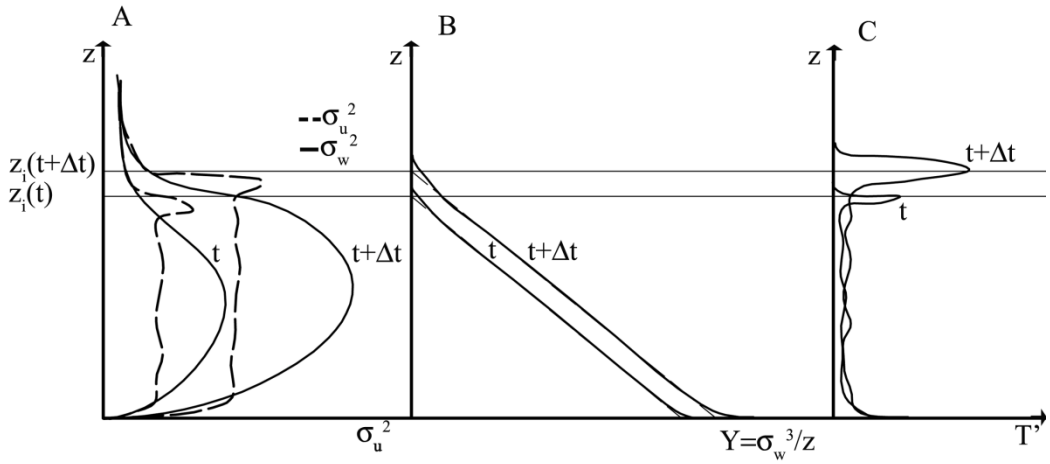

Fig.2.5 From right to left we have typical profiles of: A) velocity components variance (the vertical component is the solid line, while the horizontal one is the dash line); B) the approximation for the heat flux $Y=\sigma_w^3/z$; C) the potential temperature fluctuation (drawing not to scale).

A parameterization for the vertical variance is given, among others, by Caughey and Readings 1974 and McBean and McPearson, 1976). Neglecting the mechanical production of turbulence and considering horizontal homogeneity, we have:

$$\sigma_w{}^2(z,t) \approx 1.4\left(z\frac{g}{\theta(z,t)}\overline{w'\theta'}(z,t)\right)^{2/3} \tag{2.10}$$

Accordingly, a plot of $\frac{\sigma_w{}^3}{z}$ versus z gives an approximation for the local heat flux:

$$Y(z,t)=\frac{\sigma_w{}^3}{z}(z,t) \approx 1.7\frac{g}{\theta(z,t)}\overline{w'\theta'}(z,t) \tag{2.11}$$

In the ML the heat flux decreases linearly with height and reaches a minimum at z=z_i as shown in Fig. 2.2, thus the extrapolation to zero of the linear regression of the Y profiles provides the CBL growth with time, while the extrapolation for z=0 give an approximation for the surface kinematic heat flux q_s (Fig 2.5B; Weill et al., 1980).
Horizontal velocity variances have a similar behaviour with a uniform profile over the ML and a maximum located at about z=0.9z_i (Sullivan et al., 1998). Small variations in the location and value of the profiles maximum can occur due to the strength of the inversion (i.e. the initial stratification). CBL topped by stronger inversions, for instance, produces larger horizontal velocity variances because a greater percentage of the

upward motion in the thermals is transferred to the horizontal velocity components (Sullivan et al., 1998). Typical vertical profiles of the potential temperature variance are displayed in Fig. 2.5C. The potential temperature variance reaches a sharp maximum in the entrainment zone (at about $z=z_i$), because of the mean gradient of the potential temperature, showing that is the location of the most intense temperature fluctuations in the entrainment zone. The magnitude of this peak increases with increasing stratification (Sullivan et al., 1998).

2.2. Horizontal Scale of Structures

In order to find the horizontal scale for thermal circulation and thus the spacing of thermals, common methods employ a conditional sampling of turbulence data series to distinguish thermals from their environment.

A detailed review of methods is proposed by Young (1988) and it shows how sensitive the quantitative results are to the criteria used to distinguish structures from the environment. The most shared criterion defines thermals as the positive vertical velocity parcels, rather than positively buoyant parcels. The two definitions are in fact contradictory: in the upper CBL the updrafts are negatively buoyant on the average and also contain the entrained fluid which has opposite buoyancy than the rest of the updraft at that level. Thus positively buoyant plumes will include downward motion of SbL origin and exclude upward moving parcels of environmental origin. Conditional sampling based on vertical velocity unambiguously defines a convective updraft. Young, 1988 shows clearly how both observations and modelling results confirm that the fractional area covered by thermals is less than 0.5 throughout most of the CBL. Its value approaches 0.5 only at the surface and within the capping inversion (Fig 2.6). Estimates of minimum coverage in the mid CBL range from 0.36 to 0.43 for those studies which use a zero expected velocity threshold. Considering that the upper limit of both upward and downward regions scales with z_i, the main consequence of the above mentioned result is that for the most of CBL height the downward plumes are wider than upward thermals and only at the bottom and at the top of CBL they present almost the same width. For a given Δt, the average width of thermals are thus function of z/z_i but the sum of updraft and downdraft width remains fairly constant on average with z/z_i.

Moreover, from literature it is known that a convective thermal has a minimum aspect ratio of one, where both height and maximum width scale with z_i (Stull 1988). The horizontal length scale of the CBL can then be recognized as the distance between the cores of two thermals in excess equal to 2 z_i, according to the above considerations (Fig. 2.7). Different observational studies found that the horizontal characteristic scale for the bulk of CBL span from 1 to 2 z_i (Kaimal et al. 1976; Caughey and Palmer, 1979, Young, 1988, Stull 1988). Young (1988) computes an expected value for thermals width equal to 0.45 z_i, while a 0.55 z_i expected value is found for the environmental downdraft; the resulting width for updraft/downdraft pairs is then 1.0 z_i. Other studies (Kaimal et

al. 1976; Caughey and Palmer, 1979) show a characteristic horizontal length scale for the bulk CBL of 1.5 z_i, found by observing the peak wavelength of vertical velocity and temperature spectra after filtering.

All the above findings lead to the horizontal length scale as being a derived variable of z_i; consistently one can choose z_i as a single length scale for both horizontal and vertical dimensions.

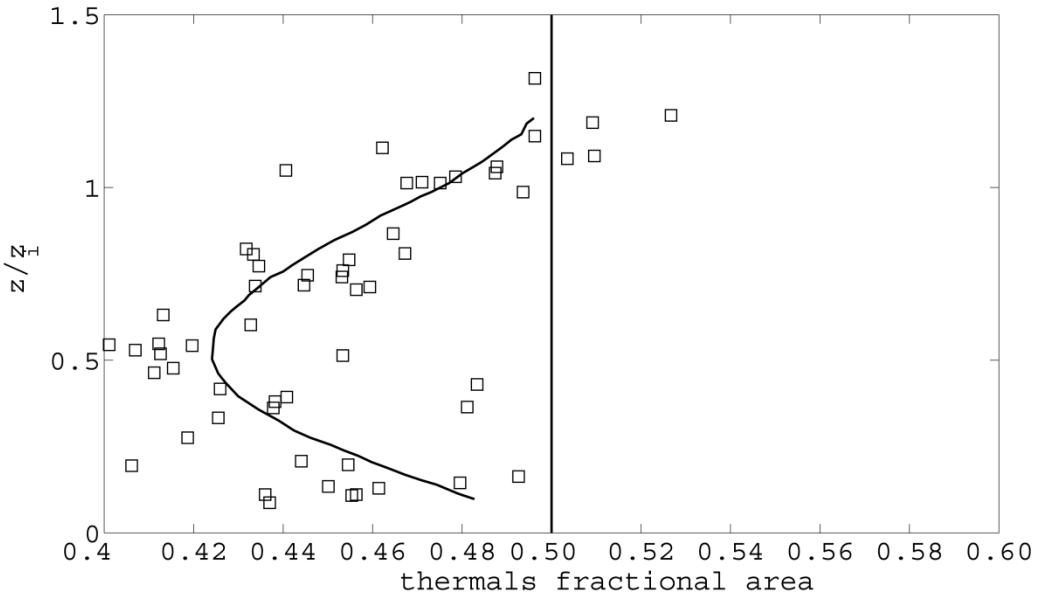

Fig.2.6 The vertical profile of the fractional area covered by thermals (Young, 1988). The fractional area covered by thermals is less than 0.5 throughout most of the CBL. Its value approaches 0.5 only at the surface and within the capping inversion.

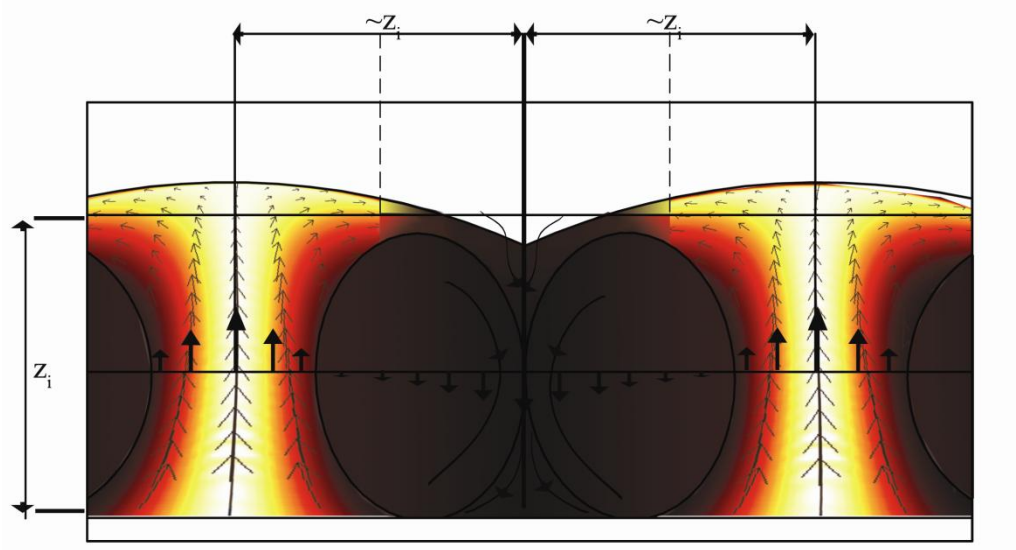

Fig.2.7 Idealization of the horizontal spacing between thermals. The lighter faded regions are updraft with positive value of vertical velocity, while darker shaded regions are environmental downdrafts. The horizontal distribution of vertical velocity in the mid CBL is qualitatively depicted, where arrow sizes are intentionally magnified for drawing purpose.

2.3. Similarity and scaling

When dealing with buoyancy generated turbulence, like turbulent Rayleigh-Benard convection, or its variants of free convection over horizontal surfaces, the following non-dimensional parameters fully describe the phenomenon according to similarity criteria:

- the Rayleigh number, as defined in (1.4), which is the ratio between the buoyancy forces driving convection to the restraining dissipative effects.
- The Prandtl number as defined in (1.4), which is the fluid capability to propagate momentum against heat; Typical values are Pr=0.7 in air and Pr=7 in water.
- The aspect ratio, AR=L/H, is a geometric parameter, which become AR>>1 for shallow convection.
- In the case of unsteady Rayleigh–Benard convection, the ratio of top to bottom fluxes is an additional parameter.

The Nusselt number Nu is defined in (2.12).

$$Nu = \frac{q_s\, H}{\kappa \Delta\theta} \tag{2.12}$$

$q_s = (\overline{w'\theta'})_{z=0} = \frac{Q_s}{\rho c_P}$: the surface kinematic heat flux

$Q_s = -K \left.\frac{\partial \theta}{\partial z}\right|_{z=0}$: the heat flux

c_p : the specific heat at constant pressure.

$K=\kappa \rho C_p$: thermal conductivity

$\Delta\theta$: is the potential temperature difference over the height H

Nu is a non-dimensional flux and depends on the above mentioned non-dimensional parameters. If a species is used to create the density difference, then species diffusivity ν_C is used instead of κ, and Schmidt number ($Sc=\nu/\nu_C$) replaces Pr (for details, see the reviews of Spiegel 1971; Adrian, Ferreira & Boberg 1986; Siggia 1994; Kadanoff 2001).

The convection becomes turbulent beyond $Ra \sim 10^5$ for $Pr \sim 7$ (Krishnamurthi 1970), from which point onwards the layer exhibits a clear division into bulk and near wall regions. Dissipative effects are important near the wall while turbulent processes dominate the bulk. The relevant bulk variables are q_s, $g\beta$ and H. Dimensional analysis implies that the fluctuation scales for length, velocity, time and temperature in the bulk are (Deardorff 1970):

- height of the CBL layer: $z_* \sim H = z_i$ (2.13)
- convective velocity: $w_* \sim \sqrt[3]{g\beta q_s z_i} = \sqrt{g\beta \vartheta_* z_i}$ (2.14)
- large eddy turnover time: $t_* \sim \frac{z_i}{w_*} \sim \frac{1}{N}$ (2.15)
- convective temperature: $\theta_* \sim \frac{q_s}{w_*}$ (2.16)

Note that w_*, the Deardorff velocity scale can also be obtained by equating the volume integrated values of kinetic energy dissipation to the buoyant production of kinetic energy. Combining the 2.16 with the 2.14 the w_* can be expressed in term of θ_* as $\sqrt{g\beta\theta_* z_i}$ and it is simple verified that t_* scales with $1/N$.

Alternatively, taking $\Delta\theta$, the temperature difference between the wall and the bulk as the independent variable instead of q_s, the above mentioned parameter scales are:

- height of the CBL: $z_\theta \sim H = z_i$ (2.17)
- bulk velocity scale : $w_\theta \sim \sqrt{g\beta\Delta\theta z_i}$ (2.18)

- bulk time scale : $$t_\theta \sim \frac{z_i}{w_*} = t_g = \frac{1}{N} \qquad (2.19)$$
- bulk temperature scale : $$\theta_\theta \sim \Delta\theta \qquad (2.20)$$

Diffusive effects are important close to the walls and there is no independent length scale in this region. The relevant independent variables are κ, ν, $g\beta$ and q_s. Based on dimensional reasoning from these variables, Townsend (1959) introduced length, velocity, time and temperature scales as

- near wall height scale: $$z_o \sim \frac{\kappa}{w_o} \qquad (2.21)$$
- near wall velocity scale: $$w_o \sim \sqrt[4]{g\beta q_s \kappa} \qquad (2.22)$$
- near wall time scale: $$t_o \sim \frac{z_o}{w_o} \qquad (2.23)$$
- near wall temperature scale: $$\theta_o \sim \frac{q_s}{w_o} \qquad (2.24)$$

Alternatively, taking $\Delta\theta$, the temperature difference between the wall and the bulk as the independent variable instead of q_s, the above mentioned parameters scales as (Theerthan & Arakeri, 1998)

- near wall height scale : $$z_{nw} \sim \frac{\sqrt{\kappa\nu}}{U_{nw}} \qquad (2.25)$$
- near wall velocity scale: $$U_{nw} \sim \sqrt[3]{g\beta\Delta t}\sqrt[6]{\nu\kappa} \qquad (2.26)$$
- near wall time scale: $$t_{nw} \sim \frac{z_{nw}}{w_{nw}} \qquad (2.27)$$
- near wall temperature scale: $$\theta_{nw} \sim \Delta\theta \qquad (2.28)$$

It is possible to express the relations between these scaling variables in terms of the non-dimensional parameters Ra, Nu and Pr. The details of these relations are given in Theerthan & Arakeri (1998) and Adrian et al. (1986). With an increase in Rayleigh number, it is believed that the bulk starts affecting the near wall flow. This is because the ratio of the bulk to the near-wall velocity increases monotonically with Ra as (Puthenveettil and Arakeri, 2005):

$$\frac{w_*}{w_o} \sim (\mathrm{Ra\ Nu\ Pr})^{1/12} \qquad (2.29)$$

Given the characteristic parameters for certain condition of flow, scaling results in the normalization of each variable with its respective homogeneous scaling parameter.

The unsteady state of penetrative convection (for example the CBL height and mean temperature increase with time), implies that the scaling parameters above defined are also function of time. Assuming quasi-steadiness, according to which the system changes through a series of steady states, scaling allows us to compare data not acquired simultaneously. Moreover scaling gives us the possibility to make results at bench scale comparable to real scale and numerical results.

2.3.1. Non-dimensional equations for the bulk convective boundary layer

Consider the system of governing equations in section 1.1.1 valid under the following hypothesis:

- Newtonian and initially stratified fluid
- Boussinesque hypothesis
- negligible Coriolis force
- vertical variations much greater than horizontal ones

A dimensional analysis of the governing equations can be useful to find the non dimensional numbers which control the phenomenon and verify that similarity based on Rayleigh and Prandtl numbers should be matched between the laboratory model and the prototype.
Using the set of reference scales found by Deardorff (1970) for the bulk CBL as defined in 2.13, 2.14 , 2.15 , 2.16, the non dimensional variables (identified by ^) are:

- $\hat{x}_i = x_i / z_*$ (2.30)
- $\hat{u}_i = u_i / w_*$ (2.31)
- $\hat{t} = \frac{t}{t_*}$ (2.32)
- $\hat{\theta} = \frac{\tilde{\theta}}{\theta_*}$ (2.33)
- $\hat{P} = \frac{\tilde{P}}{\rho_0 {w_*}^2}$ (2.34)

Applying the reference scales to variables, the non dimensional governing equations become:

$$\frac{\partial \hat{u}_i}{\partial x_i} = 0$$ Continuity equation (2.35)

$$\frac{w_*}{t_*}\frac{\partial \hat{u}_i}{\partial \hat{t}} + \frac{{w_*}^2}{z_i}\hat{u}_j\frac{\partial \hat{u}_i}{\partial \hat{x}_j} = -g\beta\theta_*\delta_{i3} - \frac{{w_*}^2}{z_i}\frac{\partial \hat{P}}{\partial \hat{x}_i} + \nu\frac{{w_*}}{{z_i}^2}$$ Navier Stokes (2.36)

$$\frac{\theta^*}{t_*}\frac{\partial\hat{\theta}}{\partial\hat{t}}+\frac{\theta_* w_*}{z_*}\hat{u}_i\frac{\partial\hat{\theta}}{\partial\hat{x}_i}=\kappa\frac{\theta_*}{z_i^{\,2}}\frac{\partial^2\hat{\theta}}{\partial\hat{x}_i^{\,2}}$$ Heat budget (2.37)

Multiplying the 2.36 by $\frac{t_*}{w_*}$ and the 2.37 by $\frac{t_*\nu}{\theta_*\kappa}$ we obtain:

$$\frac{\partial\hat{u}_i}{\partial x_i}=0$$ Continuity equation (2.38)

$$\frac{\partial\hat{u}_i}{\partial\hat{t}}+\hat{u}_j\frac{\partial\hat{u}_i}{\partial\hat{x}_j}=-g\beta\theta_*\frac{z_i}{w_*^{\,2}}\delta_{i3}-\frac{\partial\hat{P}}{\partial\hat{x}_i}+\frac{\nu}{w_* z_i}\frac{\partial^2\hat{u}_i}{\partial\hat{x}_j^{\,2}}$$ Navier Stokes (2.39)

$$\frac{v}{\kappa}\frac{\partial\hat{\theta}}{\partial\hat{t}}+\frac{v}{\kappa}\hat{u}_i\frac{\partial\hat{\theta}}{\partial\hat{x}_i}=\frac{\nu}{w_* z_i}\frac{\partial^2\hat{\theta}}{\partial\hat{x}_i^{\,2}}$$ Heat budget (2.40)

It is simple verify that the term $g\beta\theta_*\frac{z_i}{w_*^{\,2}}=1$ by using the definition of the convective velocity in eq. 2.14.
In accordance with the scaling parameters used, the Grashof number is:

$$Gr=\frac{g\beta\theta_* z_i^{\,3}}{\nu^2}=\frac{w_*^{\,2}z_i^{\,2}}{\nu^2}$$ (2.41)

Thus the non-dimensional equations become:

$$\frac{\partial\hat{u}_i}{\partial x_i}=0$$ Continuity equation (2.42)

$$\frac{\partial \hat{u}_i}{\partial \hat{t}} + \hat{u}_j \frac{\partial \hat{u}_i}{\partial \hat{x}_j} = -\delta_{i3} - \frac{\partial \hat{P}}{\partial \hat{x}_i} + Gr^{-1/2} \frac{\partial^2 \hat{u}_i}{\partial \hat{x}_j^{\,2}} \qquad \text{Navier Stokes} \qquad (2.43)$$

$$Pr \frac{\partial \hat{\theta}}{\partial \hat{t}} + Pr \hat{u}_i \frac{\partial \hat{\theta}}{\partial \hat{x}_i} = Gr^{-1/2} \frac{\partial^2 \hat{\theta}}{\partial \hat{x}_i^{\,2}} \qquad \text{Heat budget} \qquad (2.44)$$

Two non-dimensional similarity parameters appear in the above equations, Grashof and Prandtl number, or alternatively the Rayleigh and Prandtl numbers.
If a different length scale L would be employed for the horizontal dimension, an additional non-dimensional number would appear in term of the aspect ratio L/z_i.
Notice that considering the CBL height z_i as the characteristic length scale, implies including the entrainment and thus the so called "cross-over" effect typical of penetrative convection. For penetrative convection problems where a fixed length D is used as controlling parameter, an additional similarity number might appear in terms of the densimetric Froude number $\left(Fr = \frac{w}{ND} \right)$, which takes into account the entrainment effect at the interface between the CBL and the stable region. The LU et Al., 1997 similarity model for the Urban Heat Island (UHI) is a typical example. The controlling basic variable in UHI experiments is the diameter of the island D, whereas z_i is determined by D. In order to ensure the entrainment to be modelled the Froude number had to be added as a similarity parameter.
Moreover, it is interesting to observe that, using z_i and w_* as controlling parameters for length and velocity, Fr is equal to one.

3

Broader Impact of the Research

There are several well-known physical examples of penetrative convection.

A simple laboratory experiment can be realized using an insulated container of water with a bottom ice surface fixed at temperature 0°C and a top air surface at temperature 25°C (Townsend, 1964). The maximum density of water at 4°C makes the bottom layer gravitationally unstable and convective motion generated there will penetrate into the stable layer above.

Penetrative convection is also common in the environment. On a sunny morning, the nocturnal inversion of the Planetary Boundary Layer (PBL) is replaced by a growing convective layer adjacent to the warming ground. Surface cooling of sea water by evaporation can result in a gravitationally unstable surface layer which is transported downwards into the lower stably stratified layers. Penetrative convection also occurs in stars, where the turbulent convective zone grows against the stratified radiative region on the characteristic timescale of stellar evolution (Canuto and Christensen-Dalsgaard, 1998; Miesch et al., 2000).

Further, natural convection can be observed inside confined spaces of various shapes, like roof cavities, solar energy collectors, nuclear reactors and others. The phenomenon can thus be exploited for engineering design purposes.

The dynamics of penetrative convection both in natural or engineering systems influences the transport and mixing features of a given fluid, in fact the flux through the interface between the convective mixed layer and the stable layer plays a fundamental role in characterizing and forecasting the distribution of chemical species with implication for a great variety of studies, which span from the environmental geophysical topics and astrophysics to energetic engineering applications. Examples are:

1. air quality monitoring and forecasting in the lower troposphere : the dispersion of pollutants, released inside the mixed layer, is confined inside it and is influenced by micrometeorology of the PBL;
2. absorption of UV radiation studies: forecasting the redistribution of ozone is fundamental, because it is a natural filter for UV in the upper atmosphere, but a harmful contaminant in the lower troposphere;
3. climate change studies: the transport of greenhouse gases on a large scale can have great implication on the climate;
4. water quality monitoring in large water bodies like lakes and oceans;
5. water turnover and redistribution of nutrients in still water bodies: oxygen and nutrients redistribution are essential for water turnover and ecosystem preservation but if they overload the natural system can cause harmful algal blooms and eutrofization problems;
6. stellar evolution theories in astrophysics;
7. building or reactor design;
8. indoor air quality;

3.1. Planetary Boundary Layer Dynamics

3.1.1. Definitions

The motions of atmosphere, on all scales, are mainly of convective origin. Air motions are, in fact, been imposed primarily by thermal inequalities, which constantly occur due to sun-driven heating and cooling daily cycle. The particular forms of motions greatly span from chaotic thermal 3D turbulence at micro-scale to highly organized systems such as hurricanes. Nevertheless it should be noted that all scales have the common property of a non-linear atmospheric content. This is mainly due to the fact that the motions which develop transport both heat and vorticity (Saltzman, 1962).

Meteorology is intimately connected with air quality determining the concentration levels of locally emitted primary pollutants, the formation of secondary pollutants, their transport to other areas, and their ultimate removal from the atmosphere. Even if anthropogenic emissions are the source of air quality degradation, meteorology determines the magnitude of the problems that will be caused by these emissions as well as when and where these problems will occur. For example, even if both local and regional anthropogenic emissions of the major pollutants (SO_x, NO_x, and total VOC_s) are relatively constant from day to day, the measured $PM_{2.5}$ concentrations have a great variability on a daily scale, directly determined by meteorology. Each of the scales of atmospheric motion plays a role in air pollution. Micro-scale meteorological effects determine the dispersion of a plume from a local source (an industrial stack or a highway) over timescales of the order of minutes or few hours (spatial scale of order of kilometre).

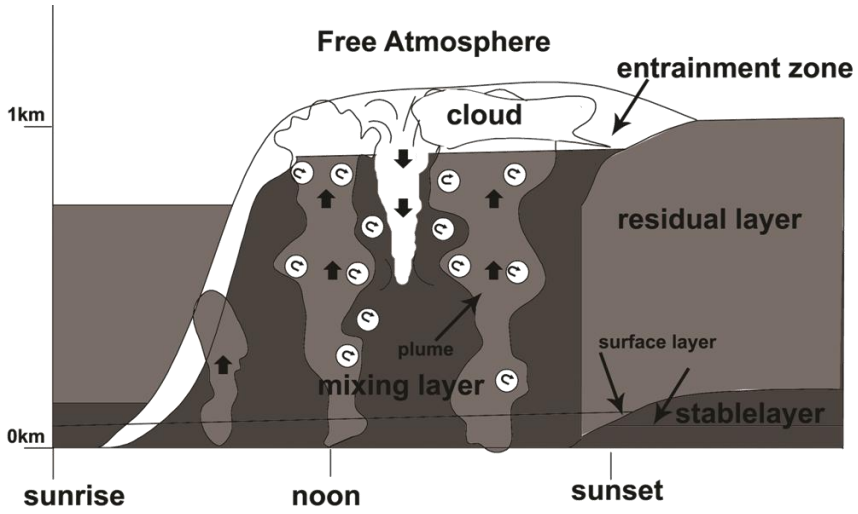

Fig. 3.1 Planetary Boundary Layer daily cycle accordingly to Stull, 1988. During the day the growth of a well mixed turbulent region (mixing layer or CBL) occurs while the PBL is heated from below by the ground. The mixed region starts to decrease after the sunset, when a neutral buoyant layer (residual layer) gradually replaces the convective zone allowing a stable stratification near the cooled ground (stable layer).

On the other hand meso-scale phenomena take place over hours or days and influence the transport and dispersal of pollutants to areas that are hundreds of kilometres from their sources.

We are focused on the phenomena occurring at micro-scale considering that most of the emissions, gases and vapour by either anthropogenic activities or nature itself, enter the atmosphere in the lower level the troposphere, in the so called Planetary Boundary Layer.

Accordingly to a famous definition by Stull (1988) the PBL is "that part of the troposphere that is directly influenced by the presence of the earth surface, and responds to surface forcing with a timescale of about an hour or less (Stull, 1988) Another shared definition is "the PBL is the part of the troposphere where physical quantities such as flow velocity, temperature, moisture etc., display rapid fluctuations, so turbulence and vertical mixing are strong".

The PBL daily cycle is sketched in Fig. 3.1. It consists in the growth of a well mixed turbulent region during the day (mixing layer or CBL), when the PBL is heated from below by the ground. The mixed region starts to decrease after the sunset, when a neutral buoyant layer (residual layer) gradually replaces the convective zone allowing a stable stratification near the cooled ground (stable layer). During the day when clouds are present in the mixing layer, the latter is sub-divided into a cloud layer and sub-cloud layer, where it is a common rule identifying the CBL height with the cloud's base. The entrainment zone acts as an interface between the free atmosphere above and the

mixing layer below. When the stability of the free atmosphere is strong enough to be classified as a temperature inversion (the absolute temperature increase with height), generally at night-time, the EZ is called capping inversion.

A dramatic increase and decrease of TKE occurs in a diurnal cycle (Fig. 3.2). The increase of TKE from a small early morning values to a large early afternoon values represents a net storage of TKE in the air. During later afternoon and evening a gradually decrease of TKE occurs, when dissipation and other losses exceed the production of turbulence. The storage term is thus negative during this transition phase.

Penetrative convection is the main cause of mixing in the PBL and thus the redistribution of pollutants (or whatever scalar) in the first kilometres of atmosphere is determined to a large extent by the temperature profile and the wind speed inside the PBL. Mechanical stress and buoyancy act as primarily forcing for convection and they interplay in a very complicated manner. Depending on micrometeorological condition one can dominate to the other deeply influencing the dynamics of the PBL. On sunny and clear sky days buoyancy generally dominates over mechanical stress.

Stability condition of the PBL is a crucial issue to classify the lower atmosphere accordingly to its attitude to generate turbulence and thus mixing processes.

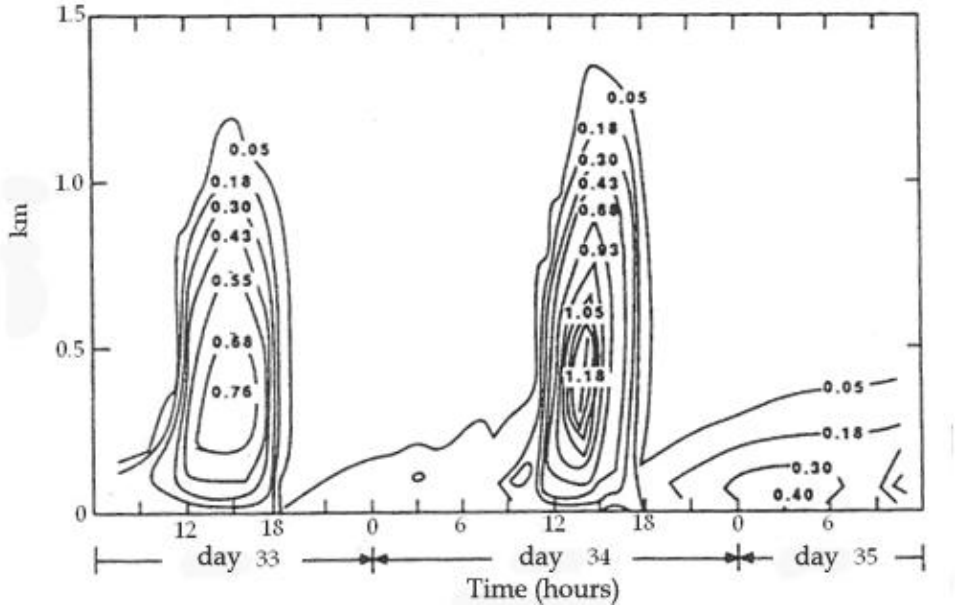

Fig.3.2 Planetary Boundary Layer TKE evolution (Stull, 1988). The increase of TKE from a small early morning values to a large early afternoon values represents a net storage of TKE in the air. During later afternoon and evening a gradually decrease of TKE occurs, when dissipation and other losses exceed the production of turbulence. The storage term is thus negative during this transition phase.

3.1.2. Atmospheric stability

Accordingly to well known stability matters, air can be classified into unstable, stable or neutral if, after an impulsive perturbation, the air move forward with perturbation, backward or do not move at all. Different stability criteria do exist to evaluate the stability regime of PBL, grouped into local and non local criteria.

Among the local criteria the most common consists in the comparison of the local lapse rate (temperature vertical gradient) with the ideal adiabatic one.
Simple thermo-dynamical considerations for dry atmosphere, in fact, lead to an adiabatic gradient of absolute temperature for a neutral atmosphere (equal to $-\frac{\partial T}{\partial z} = \Gamma \cong g/c_p = 9.8\ K/m$); then a super-adiabatic lapse rate ($-\frac{\partial T}{\partial z} > \Gamma$) is typical of unstable conditions and sub-adiabatic ($-\frac{\partial T}{\partial z} < \Gamma$) one of stable condition.

Considering the potential temperature instead of absolute temperature a simple stability criteria become:

$$\begin{aligned} &\text{neutral} \rightarrow \frac{\partial \theta}{\partial z} = 0 \\ &\text{stable} \rightarrow \frac{\partial \theta}{\partial z} > 0 \\ &\text{unstable} \rightarrow \frac{\partial \theta}{\partial z} < 0 \end{aligned} \qquad (3.1)$$

The presence of moisture in neutral atmosphere can significantly change the temperature gradient from its ideal adiabatic one written above for dry air (Γ). For air containing water vapour, in fact, the adiabatic lapse rate is a function of the water vapour content: the higher the water vapour content, the larger the heat capacity of the air parcels (c_p) and the smaller is the adiabatic lapse rate. Changing virtually the temperature of moist air (virtual temperature) until it reach an adiabatic lapse rate equal to Γ, the local stability criterion written above in 3.1 is still valid, but using the so called virtual potential temperature θ_v instead of θ.

If it is true that neutral atmosphere presents an adiabatic lapse rate the contrary is not always true. In other words the knowledge of the virtual potential temperature is usually sufficient to identify local stability condition and parts of the PBL but with an exception: the mixing layer. Mixing caused by turbulent convection determines adiabatic condition inside the mixing layer, i.e. $\frac{\partial \theta_v}{\partial z} = 0$, (Fig. 3.3). Using the local criterion in 3.1 one can be induced to consider the mixing layer neutral in term of stability. On the contrary, it stands to reason that inside the mixing layer instability conditions drive turbulence. The presence of large convective structures imposes a non

local approach to be applied and one have to observe which condition occurs below the adiabatic profile in order to classify the adiabatic region as unstable or neutral.

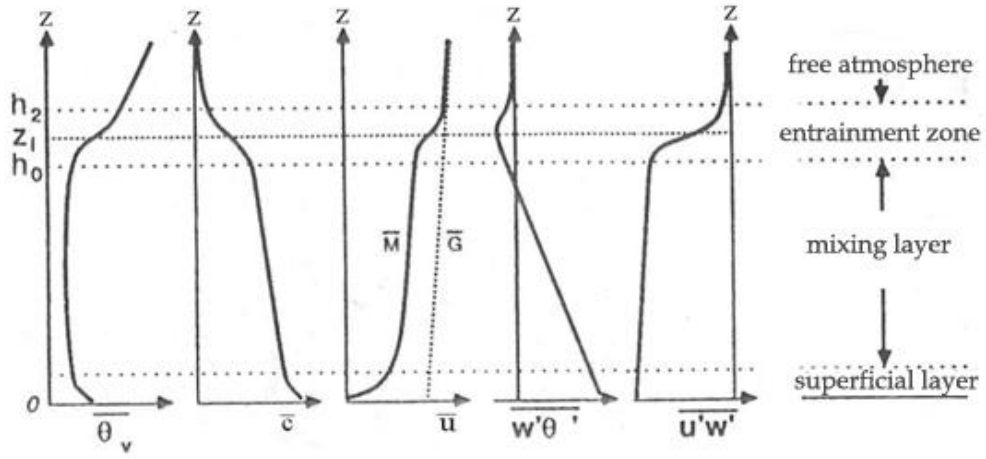

Fig. 3.3 Typical vertical profiles for some parameters of the diurnal PBL. An adiabatic profile for the virtual potential temperature is unstable if the SL is unstable according local criteria.

An adiabatic profile for the virtual potential temperature is unstable if the SL is unstable according local criteria discussed above (typical during the day, Fig.3.3), while the adiabatic region is neutral if the SL is stable according to local criteria discussed above (typical during the night).

3.1.3. Typical values of controlling parameters

Typical values of the controlling parameters for a sunny cloud-free diurnal PBL are shown in table 3.1. The order of magnitude of variables is computed from condition of Oklahoma atmosphere at 6pm on 7th July 2003 (from Oklahoma Climatological Survey public database).

3.2. Upper Lake and Ocean Dynamics

The upper part of a large water body connects the surface forcing from winds, heat, and fresh water, with the quiescent deeper region where this heat and fresh water are sequestered and released on longer time and global scales. The vertical structure of the water body is primarily defined by changes in the temperature (and salinity in the ocean), which together control the water column's density structure. Along the vertical direction, a number of distinct layers can be distinguished which are formed by different processes over different timescales (Fig. 3.1):

parameter	value	unit
t_κ	~ 10^{11}	s
t_ν	~ 10^{11}	s
t_g	~ 100	s
z_i	~ 500-2500	m
Δt	~4	K
ν	~1,5 10^{-05}	$m^2 s^{-1}$
ρ	~1,14	Kg m^{-3}
κ	~2,1 10^{-05}	$m^2 s^{-1}$
β	~3,4 10^{-03}	K^{-1}
Pr	~0.7	
Ra	~ 10^{12} - 10^{14}	
w*	~ 1-2 m	s^{-1}
t*	~ 1000	s
θ*	~0.1	K

Table 3.1 Characteristic parameter for real atmosphere under clear sky and weak winds condition (taken from the public database of Oklahoma Climatological Survey, conditions of atmosphere at 6pm on 7th July 2003)

1) the upper mixed layer (Epilimnion) with a thickness of a few to several hundred meters. The action of the wind blowing over the water surface generates waves that penetrate deeply into this layer. As the waves travel and eventually break, they continually overturn this layer, hence its name. This layer tends to be relatively warm, since it is the region into which sunlight (energy) penetrates and is ultimately absorbed. Most ocean life lives in this layer due to the availability of sunlight to drive photosynthesis. Gases are exchanged with the atmosphere at the top of this layer, and water is lost by evaporation and recovered in the form of precipitation. In the tropical oceans particularly, this layer also has relatively low salt content, since it receives all the (fresh) rainwater falling on the ocean as well as river runoff. In oceans, the surface currents flow in this layer; they tend to be relatively shallow and well-defined, and to flow at relatively high speed.
2) The pycnocline**,** situated between the mixed layer and the deep layer, is where water density increases rapidly with depth because of changes in temperature

and/or salinity. Recall that cold water is denser than warm water and salty water is denser than fresh water. Where a decline in temperature with depth is responsible for the increase in density with depth, the pycnocline is also a thermocline (lakes). On the other hand, if an increase in salinity is responsible for the increase in density with depth, the pycnocline is also a halocline (oceans). Typically, the pycnocline extends to a depth of 500 to 1000 m. In middle latitudes seasonal pycnoclines may develop within the mixed layer and entrainment phenomenon takes place between the two regions.

3) The deep layer below the pycnocline (hypolimnion) accounts for most of the water body mass. It is dark (since sunlight does not penetrate this deep) and cold, with a temperature very close to ~4° C, the temperature at which liquid water is most dense. In oceans these waters contain a relatively high salt content. Mixing is generally very slow. Life is sparse, and relies on organic matter settling downward from the well-mixed layer. Deep ocean currents tend to be broad and deep, and not well-defined, and to flow slowly through these waters.

The presence of a well mixed upper layer on a daily and seasonal time scale is of fundamental importance for the water turnover and protection of large water bodies. Cooling and evaporation induce convective mixing and overturning, whereas heating and rainfall cause the mixed layer to re-stratify in depth and display alternate levels of greater and lower vertical property gradients. Thus, if strong enough, the wind and buoyancy fluxes can generate sufficient turbulence so that the upper portion of the surface layer has a thick, homogeneous (low vertical gradient or stratification), well-mixed layer in temperature, salinity, and density. Variations in the strength and relative contributions of the atmospheric forcing can cause substantial variability in the water properties and thickness of the upper mixed layer. Large temporal variation can occur on daily and seasonal timescales due to changes in the solar radiation. For example, during the daily cycle the sun heats the ocean causing the upper surface to become increasingly warm and weakly stratified. The typical vertically uniform mixed layer may not be present in the upper ocean surface layer. As the sun sets, the surface waters are cooled and sink, generating turbulent convection that causes entrainment of water from below, and mixing that produces the vertically well-mixed layer.

Furthermore, the mixed layer structure can exhibit large horizontal variations. For example, the large differences in solar radiation along meridians result in mixed layers that generally increase in depth from the equator to the poles. Even in the east-west direction, boundary currents and differential surface forcing can result in mixed layers of different structures, although differences in the annual variations of temperature along a given latitude will generally be small. Moreover the stability within the pycnocline may offer resistance for the mixed layer development. If the vertical density gradient in the pycnocline is very strong, the turbulence within the upper mixed layer induced by the air-water exchanges of wind and heat, cannot overcome the great stability of the pycnocline to penetrate into the deeper water body. The base of the

pycnocline marks the depth limit of the upper surface layer. Under this depth, the water has not seen the surface for a very long time, and above it, the stability of the pycnocline acts as a barrier against turbulent mixing processes.

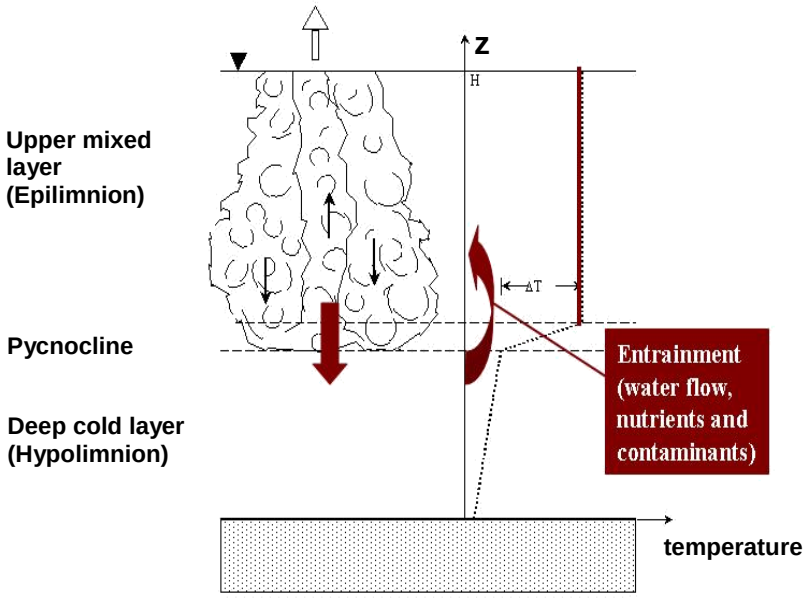

Fig. 3.4 Sketch for the upper lakes and oceans dynamics. If strong enough, the wind and buoyancy fluxes can generate sufficient turbulence so that the upper portion of the surface layer has a thick, homogeneous (low vertical gradient or stratification), well-mixed layer in temperature, salinity, and density. The deep and dark layer below (hypolimnion) accounts for most of the water body mass. Entrainment occurs at the interface between the two regions

In some polar regions, particularly in the far North and South Atlantic, no permanent thermocline exists. The isothermal water column suggests that the cold, dense waters are virtually continuously sinking to great depths. No stable permanent pycnocline or thermocline exists as a barrier to the vertical passage of the surface water properties that extend to the bottom. In some cases, such as along the shelf in Antarctica's Weddell Sea in the South Atlantic, salinity can also play a role in dense water formation. When ice forms from the sea water in this region, it consists primarily of fresh water, and leaves behind more saline and thus denser surface water that must also sink. The vertical flow of the dense waters in the polar regions is the source of the world's deep and bottom waters that then slowly mix and spread horizontally via the large-scale thermohaline ocean circulation to fill the deep ocean basins. In fact, the thermohaline circulation also plays an important role in maintaining the permanent thermocline at a relatively constant depth in the low and middle latitudes. Despite the

fact that the pycnocline is extremely stable, it might be assumed that on some timescale it could be eroded away through mixing of water above and below it.

The water turnover that follows the development of the upper mixed layer is also the main cause of the redistribution of oxygen and nutrients within the water body. The ecosystems are fed by the rising of substances from the deeper water, where most of the nutrients are concentrated. On the other hand water pollution can cause an overload of nutrients in terms of nitrogen and phosphorous, which directly determines algal blooms. The algal species are often harmful or toxic for the fish population causing the break of the marine food-chain. Moreover algal blooms can cause oxygen concentration became lower the critic level, impairing the whole marine ecosystem equilibrium and the human activities depending on it.

3.3. Additional Applications

In addition to the study of geophysical flows a wide range of physical and engineering applications occurs for turbulent natural convection.

One of the main issues in the theory of convection is what happens at the convective-radiative boundary in stars. Stars of mass less than approximately one solar mass present a radiative core and a convective envelope; more massive stars have a convective core and a radiative envelope (Canuto and Christensen-Dalsgaard, 1998), as sketched in fig. 3.5. Turbulent motion in the convective region may penetrate the stably stratified radiative region. Between the two layers there is a gradual transition from convective to stable condition, known as convective penetration zone. Below it, energy is transported outwards entirely by radiative diffusion. At the penetrative convection depth, the gas becomes suddenly less opaque, becomes unstable, and convective transport becomes dominant. The depth at which convective plumes penetrate into a stable layer can affect many aspects of stellar theory and evolution. Of great interest is the structure of the tachocline, which is thin layer at the base of the solar convection zone. This shallow shear layer between the solid-body rotation of the interior radiative zone and the differential rotation of the convection zone in the Sun is poorly understood and its structure is not well determined observationally or theoretically. Different theories and techniques are developed to determine its vertical extension as an important ingredient for the so-called solar dynamo. Therefore, understanding convective penetration below the convection zone, particularly in the case of the Sun, is of fundamental importance. Mixing of species below the convection zone is important for models of stellar evolution. Different theories are applied to quantify mixing inside the convective region and transport through the penetration zone, most of which has been previously applied to geophysical flows, as turbulent transilient theory firstly proposed by Stull and Driedonks in 1987 for atmospheric investigation (Miesch et al., 2000).

Heat and mass transfer phenomena connected to the development of turbulent natural convection finds outstanding applications also in enclosures with various

shapes and wall conditions. In recent years a greater and sustainable energy demand impose efficiency improvements to be mandatory in several engineering fields, such as building thermal design and energetic efficiency, nuclear reactor design, solar energy collector, and others.

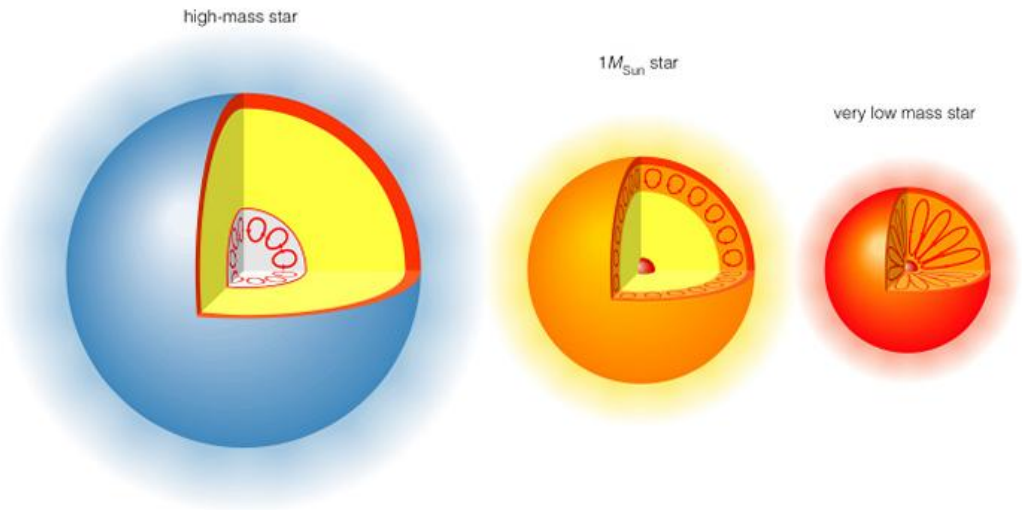

Fig. 3.5 Sketch of convection occurring in high-mass and low-mass stars. Stars of mass less than approximately one solar mass present a radiative core and a convective envelope; more massive stars have a convective core and a radiative envelope (Canuto and Christensen-Dalsgaard, 1998).

For instance building units exposed to great temperature gradients, like roof cavities, attics, building facade elements and building bricks need particular attention during the design phase in order to improve the insulation of the whole building and increase its energetic performance. The flow and heat transfer inside the enclosure is controlled by its geometrical feature (shape, aspect ratio), building materials, orientation of the external surfaces, which lead to different temperatures gradients over the walls (Ben-Nakhi and Mahmoud, 2006). An example of convective cell occurring in a building attic during a summer day is sketched in Fig. 3.6. Ben-Nakhi and Mahmoud (2006) found that at Ra = 10^9, the total heat flux into the indoor through the roof construction increases by 21%when the roof-cavity aspect ratio increases from 1 to 6. In a similar trend, for an aspect ratio equal to 6, the total heat flux through the roof construction increases by 25% when Ra increases from 10^3 to 10^{10}. Means of improving the enclosure construction with the goal of reducing that heat flux is the subject of several ongoing investigations.

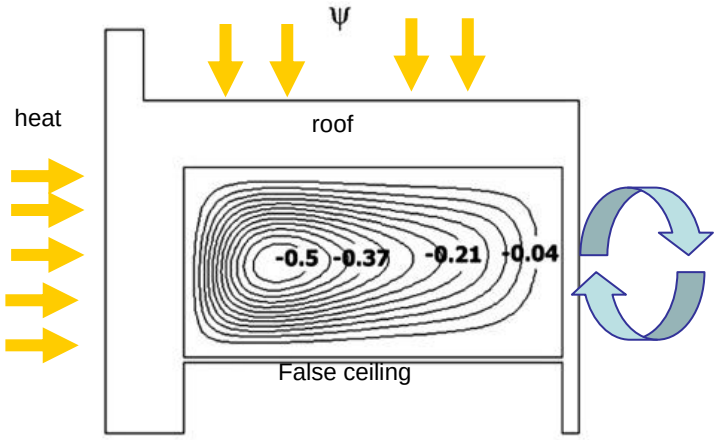

Fig. 3.6 Sketch of convection inside a building attic under summer day boundary condition (Ben-Nakhi and Mahmoud, 2006).

4

The Experimental Model

4.1. Experimental Set-up

The laboratory model consists of a convection chamber containing an initially stable, density stratified fluid, which is heated from below to trigger destabilization and penetrative convection. The experimental set-up is basically the same as Cenedese and Querzoli (1994), Querzoli (1996), Cenedese and Querzoli (1997) and Moroni and Cenedese (2006), but when possible equipment and procedures have been upgraded in term of accuracy and precision (thermocouple calibration, illumination and optical assembling).

The test section is a tank with a square base (0.41×0.41 m^2) and 0.40 m high. Its lateral sides are insulated by 0.03 m thick removable polystyrene sheets. When images are acquired, the insulation on the sides facing the cameras is removed to allow optical access. Distilled water is used as working fluid, to allow both a large heating rate and sufficient time to take measurements of the evolving thermal structures. Pollen particles of about 40 μm mean diameter and 1.06 g cm^{-3} density (Moroni and Cenedese, 2005) are used as neutrally buoyant and passive tracer to reconstruct particle trajectories. A diffuser, which also acts to insulate the upper surface since it is attached to a polystyrene sheet, floats on the surface of the water as it fills the tank (Fig. 4.1). A tank filled with hot water drains by gravity into a continually stirred colder tank and that tank in turn drains to the diffuser. While the diffuser floats upwards, it fills the test section creating a linear stratification of the fluid, cold to hot from bottom to top (two-tank filling method, Fig. 4.1). In the meantime the bottom is maintained at a constant temperature (T_{s0}) using a heat exchanger connected to a cryostatically controlled cold bath. The filling time ranges from 30 to 60 minutes depending on the gradient. The fluid initial conditions are velocity equal to zero and linear increase of temperature with height through a slope of $1/\gamma$. Both velocity and temperature are measured before convection is started to ensure steady state is reached. After the fluid stratification

within the tank is completed, a thermostatically controlled hot water bath is connected to the metal base plate at the bottom and the experiment begins.

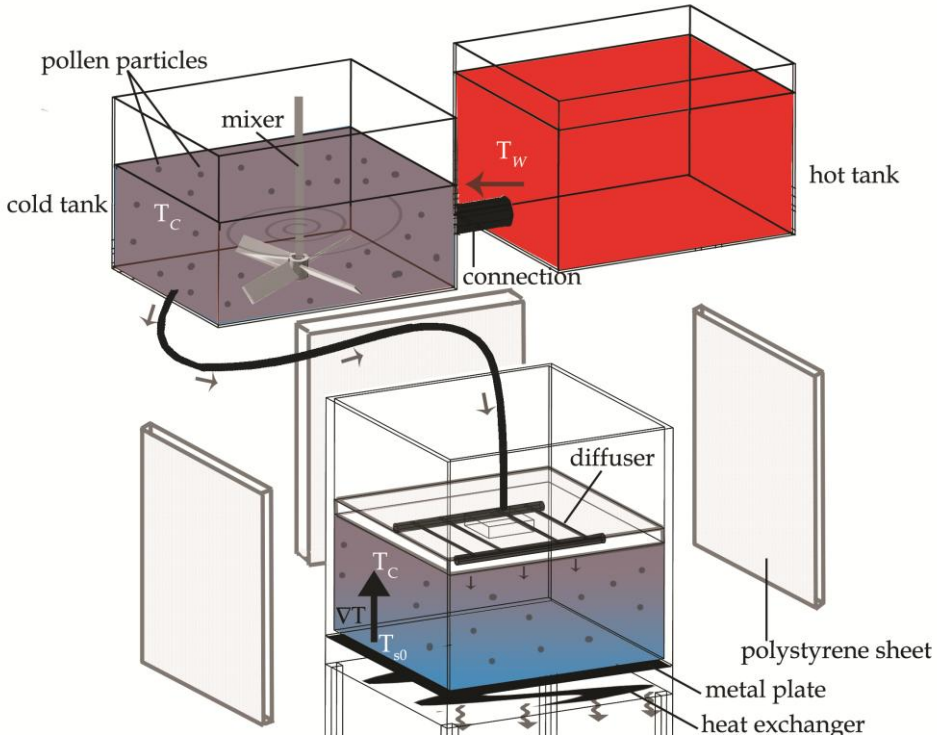

Fig. 4.1 Sketch of the filling procedure using the two connected tanks method. A tank filled with hot water (TW) drains by gravity into a continually stirred colder tank (TC) and that tank in turn drains to the diffuser. While the diffuser floats upwards, it fills the test section creating a linear stratification of the fluid, cold to hot from bottom to top. During filling the test section the bottom is maintained at a constant temperature (Ts0) using a heat exchanger connected to a cryostatically controlled cold bath.

Convection is sustained by maintaining a temperature always greater than the average temperature within the mixing layer (Fig. 4.2). In fact, thermal convection can occurs upon replacing the cool water circulating under the lower boundary with warm water of temperature greater than the upper boundary temperature. The temperature at the bottom, T_s, gradually increases approaching the final value T_{sf}.

Temperature is detected through T-type thermocouples (Fig. 4.3) of uncertainty less than 0.1 °C (Fig. 4.4). Thermocouples are placed within the test section along a vertical array of 26 probes to measure vertical profiles and on the lower boundary to test horizontal homogeneity in supplying heat.

T- thermocouples are made of copper and a copper (60 %)/nickel (40 %) alloy (constantan).

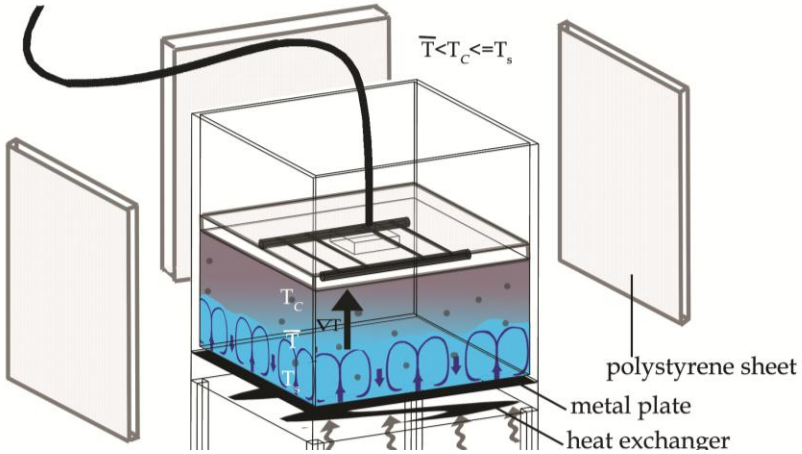

Fig. 4.2 Sketch of the fluid configuration during the experiment. A thermostatically controlled hot water bath is connected to the metal base plate at the bottom and the fluid is heated from below. Convection is sustained by maintaining a temperature at the bottom (T_s) always greater than the average temperature within the mixing layer ($\overline{T}$).

The cold junctions are obtained inside a Hoover vase by immersing each metal joint between copper and constantan inside an ice-water bath at 0.00±0.1° C. Each junction has been placed inside a glass tube filled with doubly distilled water to restrain corrosion which causes the increase of metal electric resistance.
The calibration is performed by doing measurements in a thermostatic bath at temperatures ranging between 5.00±0.01 °C and 40.00±0.01 °C. It appears that slight differences in output voltage between individual thermocouples exist. Therefore, every thermocouple is assigned its own calibration parameters (Table 4.1). For the calibration parameters, linear fits are used ($T \approx aV+b$, with V the measured voltage in mV) and optimized by minimizing the sum of squared differences.
Calibration results for thermocouples are summarized in table 4.1 and a calibration fitting curve for a generic thermocouple is provided in Fig. 4.5.
The same experimental set up is arranged into two different optical configurations named in the followings as 2D arrangement and 3D arrangement. The former employs a single camera focused on a thin light sheet, while the latter uses a stereoscopic system of cameras focused on an illuminated volume to measure the two components of velocity in a plane and the three components of velocity in a volume respectively.

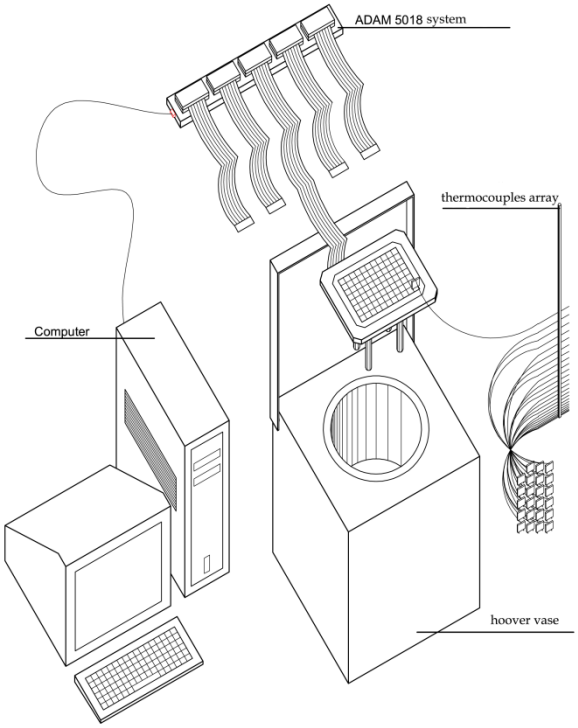

Fig. 4.3 Sketch of the ADAM 5018 temperature acquisition system

#channel	constant	#channel	constant	#channel	constant
1	25.39	12	25.24	23	25.57
2	25.34	13	25.26	24	25.72
3	25.44	14	25.28	25	25.74
4	25.66	15	25.46	26	25.90
5	25.43	16	25.40	28	25.82
6	25.37	17	25.43	29	25.86
7	25.35	18	25.59	30	25.99
8	25.31	19	25.63	31	25.94
9	25.20	20	25.69	32	25.93
10	25.40	21	25.59	34	25.85
11	25.36	22	25.75	35	25.86

Table. 4.1 Thermocouple calibration constants. Each thermocouple is labelled with the number of its channel. Thermocouples arranged in the vertical array are connected to the first 26 channels. Channel 28 and 29 refer to monitoring thermocouples on the lower boundary, while channel 30 to monitoring thermocouple inside the cold tank. Thermocouples connected to channels 31-32-34 and 35 are spare probes.

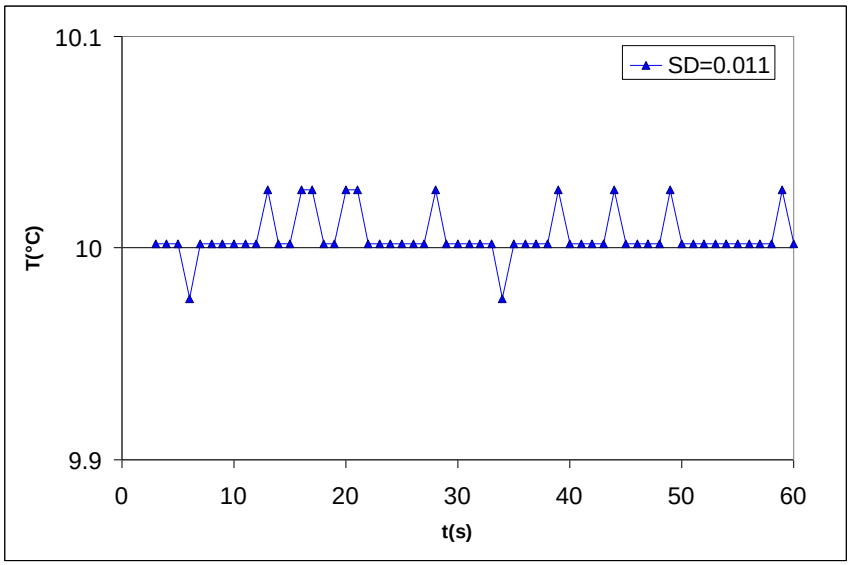

Fig. 4.4 Acquired signal over time for a generic thermocouple (#10 in table 4.1)

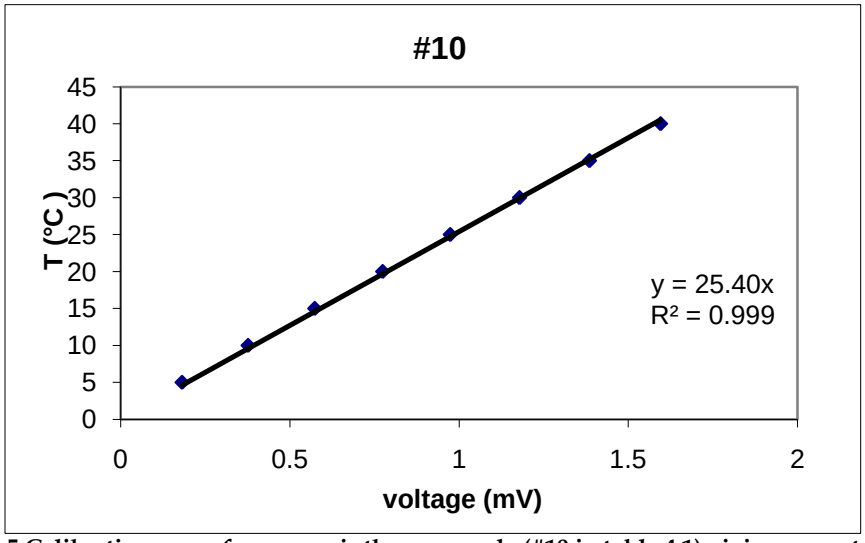

Fig. 4.5 Calibration curve for a generic thermocouple (#10 in table 4.1) giving a constant of 25.40 °C/mV

4.1.1. 2D arrangement

The arrangement employed to measure two component velocities in a plane is sketched in Fig. 4.6. It is basically the same as Cenedese and Querzoli (1994), Querzoli (1996), Cenedese and Querzoli (1997) and Moroni and Cenedese (2006), a part from the illumination system, which has been improved.

Images of well reflecting tracer particles were recorded by using a single monochrome 8-bit CCD camera with a time resolution of 25 fps, focused on the mixing layer region (acquisition window of 15 cm side approximately). The measuring plane is illuminated by a thin light sheet obtained by collimating a divergent light beam, produced by a 150 Watt halogen source, using a light-line fiber optic guide equipped with a cylindrical lens. The white light source can be replaced with a monochromatic 5 Watt LED source if fluorescence imaging is employed for visualization.

The acquisition procedure can be divided into two steps. Images are first stored on the mass memory of a computer (576x764 pixels resolution). Then they are analyzed to detect trajectories. Trajectory and the sparse velocity field are detected through the 2D Feature Tracking (Miozzi, 2004, Miozzi et al., 2008).

Feature Tracking (FT) algorithms focus their attention on pixel luminosity intensity gradients distributed within each image, recalling the "image brightness constancy constraint" and assuming the hypothesis of tracer particles behaving as Lambertian surfaces. The intensity gradients are likely distributed around the particle border and those are tracked frame by frame. The issues of properly separating a particle from the image background and computing its centroid are overcome (Moroni and Cenedese, 2005). FT is suitable for analyzing any particle density images and it does not require a priori velocity estimates to identify particle trajectories. The technique employed for this investigation implements a pure translation model (Miozzi, 2004; Moroni and Cenedese, 2005; Miozzi et al., 2008). When a 2D image analysis technique is employed, camera calibration simply consists in computing the pixel/cm ratio, acquiring one image of a known spacing target grid.

4.1.2. 3D arrangement

The arrangement employed to measure three component velocities in a volume has been newly designed (Dore et al. 2009a) and is sketched in Fig. 4.7.

An approximately $0.15 \times 0.15 \times 0.40$ m^3 light volume (shaded region inside the test section in Fig 4.7) is obtained using a high power arc lamp (1000 W). A 45° mirror is mounted on a cubic light guide to reflect the light and concentrate it in the middle of the test section. The Images of the pollen particles are now recorded using a stereoscopic system made by three synchronized 764×576 pixels CCD cameras with a time resolution of 25 frames per second. Synchronization of the cameras is obtained by using the sync signal from one of the cameras as the triggering signal for the others. Each camera is connected to a different colour input of a RGB frame grabber and the full resolution images are stored as single channel bmp files.

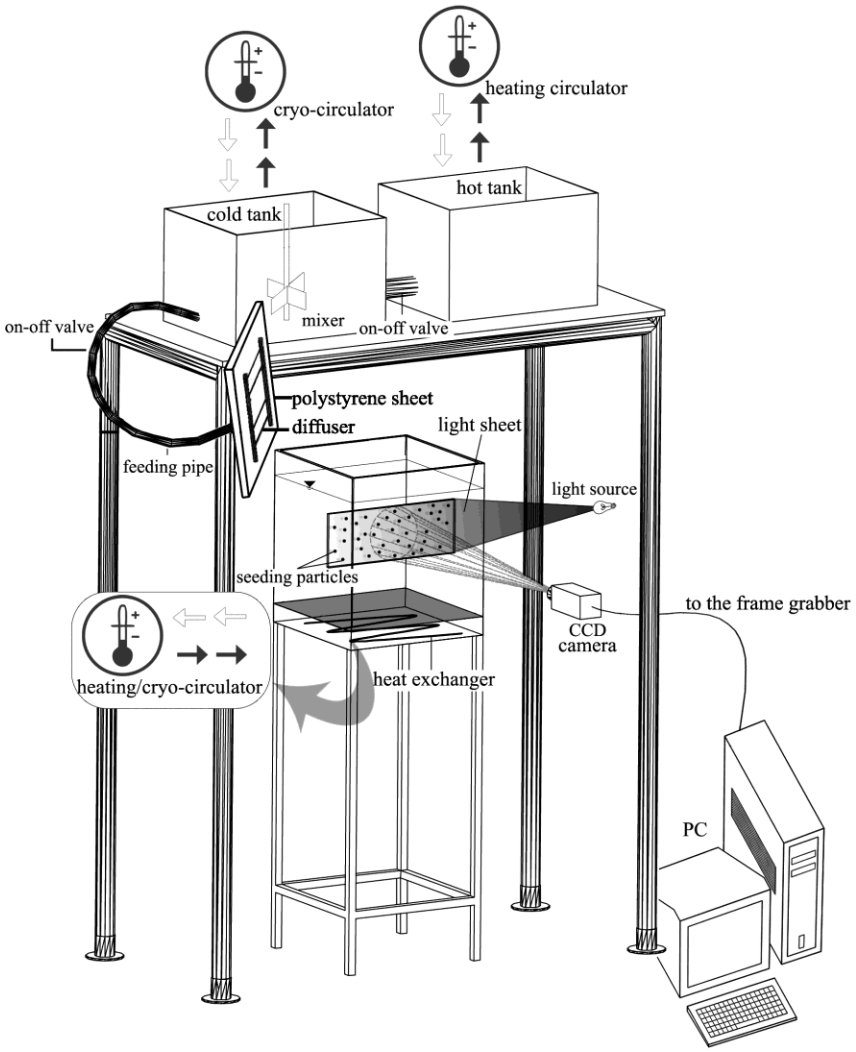

Fig. 4.6 Sketch of the 2D arrangement. The experimental set-up used for the 2D measurements is the same as Cenedese and Querzoli (1994), Querzoli (1996), Cenedese and Querzoli (1997) and Moroni and Cenedese (2006) a part from the illumination system, which has been improved.

The geometrical features of the experimental apparatus determine the camera arrangement; the three CCD cameras are mounted as equidistant as possible from the test section with each optical axis approximately perpendicular to the side of the tank the camera faces. Subsequently, with a square based tank, the optical axes of successive cameras should be at 90° angles and lie on the same plane.

The stereoscopic system has to be properly calibrated in order to reconstruct a 3D object from 2D multiple views, applying 3D-Particle Tracking Velocimetry (3D-PTV).

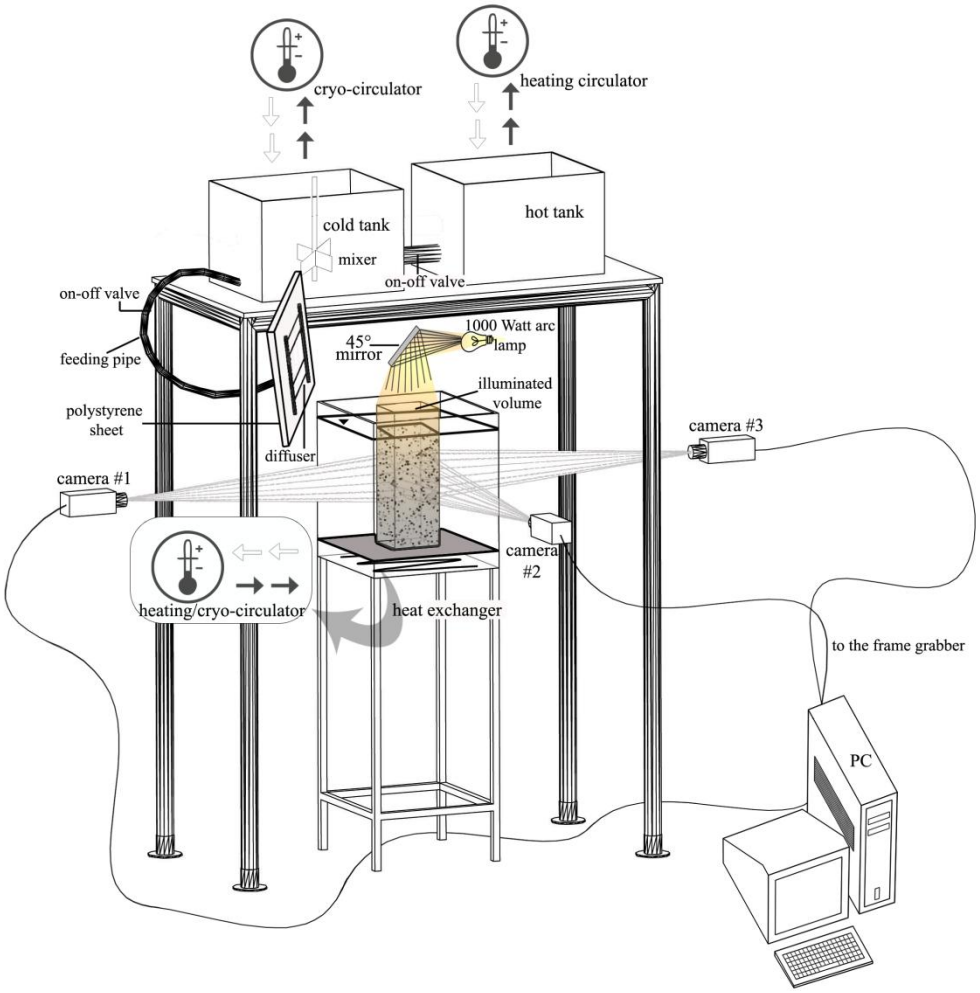

Fig. 4.7 Sketch of the 3D arrangement. The optical arrangement has been newly designed to apply 3D-PTV (Dore et al. 2009a).

4.2. Photogrammetric Particle Tracking Velocimetry

The technique of 3D particle tracking was introduced by Chang and Taterson (1983) and further developed by (among others) Maas *et al*. (1993). Suzuki *et al*. (2000) applied three-dimensional Particle Tracking Velocimetry to simultaneous measurements of fluid and dispersed phases in a turbulent water channel flow and clarify the mutual

interaction between near-wall coherent structures and solid particles. Instantaneous 3D vectors of tracer and solid particles were obtained from four successive sets of particle images. Kieft *et al.* (2002) applied a 3D Particle Tracking Velocimetry algorithm to the wake flow behind a heated cylinder. The performance of the 3D particle localization and tracking technique was studied and tested with respect to its accuracy. Both for the calibration and the accuracy tests, synthetic data were created by traversing a 2D grid through the measuring volume. The method assumes a particle in a camera image will have a position in the world coordinate system somewhere along the particle projection line. The points in space where the lines from the different cameras cross are the possible positions of the particles. Due to optical disturbances, random camera noise and errors in the calibration data, an exact crossing of the lines is unlikely and a line crossing is detected when the minimum distance between the lines is smaller than a certain critical value. Doh *et al*. (2004) describe 3D-PTV experiments investigating the structure of a sphere wake. To obtain the three-dimensional velocity vectors, camera parameters were obtained in advance. Next, the position of each particle was detected and finally the three-dimensional velocity vectors were calculated.

The starting points for the photogrammetric reconstruction of a 3D object in real space from 2D image projections are: the pinhole model for cameras and the mathematical relations of photogrammetry based on the collinearity assumption. According to the pinhole principle, a camera is modelled by its projective centre C and the image plane π. A 3-D point P is projected into an image point P′ given by the intersection of π with the line containing C and P (Fig. 4.8). The line containing C and orthogonal to π is called the optical axis and its intersection with π is the principal point (PP). The distance between C and π is the focal distance (c).

Introduce the following reference frames (Fig. 4.8):

- the world reference frame OXYZ is an arbitrary 3D reference frame where the position of 3D points in the scene are expressed and can be directly measured;
- the image reference frame $\xi\eta\zeta$ is the coordinate system where the position of pixels in the image are expressed (ζ= 0 for all image point and ζ= c for the projective centre);
- the camera standard reference frame Cxyz is a 3D reference frame solidal to the camera, centred in C, with the z axis coincident with the optical axis, x parallel to ξ and y parallel to η.

According to those reference frames, the fundamental relations of photogrammetry allow one to determine the image coordinates ξ and η of a generic image point P′ from the X, Y, Z coordinates of the corresponding object point P in the world reference frame, knowing the camera space orientation and its intrinsic parameters. Starting from the collinearity condition, which states that the object point, camera projective centre, and image point must lie on a straight line (Maas, 1992), the relations are analytically described by Eqs. 4.1 and 4.2:

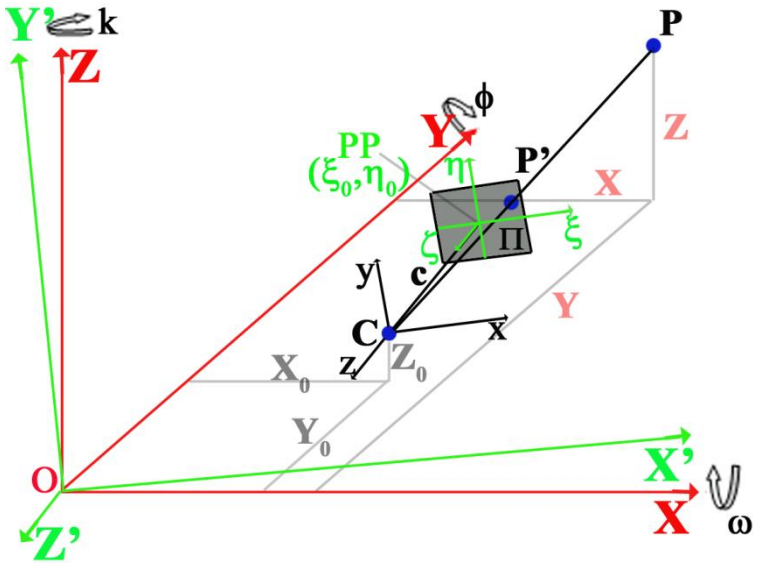

Fig. 4.8 Camera pinhole model and reference frames employed by the classical photogrammetric approach (Maas et al 1993).

$$\xi = \xi_0 - c\frac{r_{11}(X - X_0) + r_{21}(Y - Y_0) + r_{31}(Z - Z_0)}{r_{13}(X - X_0) + r_{23}(Y - Y_0) + r_{33}(Z - Z_0)} \quad (4.1)$$

$$\eta = \eta_0 - c\frac{r_{12}(X - X_0) + r_{22}(Y - Y_0) + r_{32}(Z - Z_0)}{r_{13}(X - X_0) + r_{23}(Y - Y_0) + r_{33}(Z - Z_0)} \quad (4.2)$$

(X, Y, Z): object point coordinates in the world reference frame
(X_0, Y_0, Z_0): camera projective centre coordinates in the world reference frame
$r_{ij:}$ elements of 3×3 rotation matrix **R** with angles ω, φ, κ
(ξ_0, η_0): image principal point
c: image focal distance
The spatial rotation matrix **R** indicates the spatial arrangement of the frame related to the coordinate system OXYZ. The elements r_{ij} can be expressed as a function of the rotations ω, ϕ and κ (4.3):

$$R_{\omega\phi\kappa} = \begin{pmatrix} \cos\phi\cos\kappa & -\cos\phi\sin\kappa & \sin\phi \\ \cos\omega\sin\kappa + \sin\omega\sin\phi\cos\kappa & \cos\omega\cos\kappa - \sin\omega\sin\phi\sin\kappa & -\sin\omega\cos\phi \\ \sin\omega\sin\kappa - \cos\omega\sin\phi\cos\kappa & \sin\omega\cos\kappa + \cos\omega\sin\phi\sin\kappa & \cos\omega\cos\phi \end{pmatrix} \quad (4.3)$$

where ω is the rotation in a counter clockwise direction around the X axis, ϕ around the Y axis and κ around the Z axis in order to have X Y and Z overlapping x, y and z respectively. The order the rotations have to be applied is ω, ϕ and κ.
Parameters to be determined in order to use equations (4.1) and (4.2) are the camera intrinsic parameters (ξ_0, η_0, c) and extrinsic parameters (X_0, Y_0, Z_0, ω, ϕ, κ). The camera

manufacturer states that ξ_0 and η_0 are zero. System calibration is needed to deduce the unknown parameters. Additional parameters for systematic image deformation and the multimedia geometry are not mathematically included in the calibration procedure, but calibration was conducted both inside water and air to directly check the effects of refraction in a multimedia geometry and include those effects into the calibration parameters.

We have chosen a world coordinate reference system (OXYZ) with its origin coincident with the test section lower internal corner. Considering the point of view of camera 2, the reference system axes are parallel to the three edges of the test section with the X axis oriented from left to right, the Z axis from the bottom to the top and the Y axis inside the tank (Fig. 4.9).

4.2.1. Calibration

The aim of the calibration procedure for a stereoscopic system is to determine the intrinsic and extrinsic parameters of each camera in order to solve the photogrammetric problem (eqs. 4.1 and 4.2). In many cases, the overall performance of the 3D trajectories reconstruction from stereo views strongly depends on the accuracy of the camera calibration, a very sensitive procedure. Several methods for geometric camera calibration are presented in literature, divided into explicit methods, based on the physical parameters defined in the previous section, and implicit ones, where those physical parameters are replaced by a set of non-physical implicit parameters that are used to interpolate between some known target points (Heikkila and Silven, 1997).

We developed an explicit physically-based calibration procedure using eqs (4.1) and (4.2) in their inverse form and minimizing a non-linear error function through least squares estimation. Pre-calibration was performed to ensure each camera's optical axis is approximately orthogonal to the corresponding test section face, providing the starting values of the rotation angles for the calibration procedure (Table 4.2).
The following steps allow calibration of the acquisition system (Fig. 4.9):

1. place an equally spaced 0.01 m grid of alternatively distributed black and white squares inside the test section;
2. mount this target on a precision motor positioner, which can move along two perpendicular directions;
3. for each camera acquire images of the target for seven different positions, each parallel to the others and to the corresponding face of the test section, along the optical axis direction of the considered camera; the coordinates of each target point in the world reference frame ($X_iY_iZ_i$) are measured with an uncertainty of ±0.5 mm (step 1 in Fig. 4.9);
4. reconstruct the target point coordinates in the image reference frame ($\xi_i\eta_i$) using a corner detection algorithm (step 2 in Fig.4.9);

5. convert the image coordinates from pixels to centimetres using the camera sensible area dimensions (for our CCD 0.64906x0.48306 cm² corresponds to 782x582 pixels);
6. identify the camera intrinsic and extrinsic orientation parameters in the absolute reference system using the photogrammetric approach (step 3 in Fig. 4.9, Moroni *et al.*, 2009);
7. compute the estimated coordinates ($\bar{\xi}_i$, $\bar{\eta}_i$) using the photogrammetric equations, together with the calibration parameters found in the previous step, and perform the error analysis (step 4 in Fig. 4.9).

The three-camera set-up of Fig. 4.9 involves the following rotation matrices computed from the starting values of ω, ϕ and κ reported in Table 4.2 (for camera #1, camera #2 and camera #3 respectively):

$$R_1 = \begin{bmatrix} 0 & 0 & -1 \\ -1 & 0 & 0 \\ 0 & 1 & 0 \end{bmatrix} \qquad R_2 = \begin{bmatrix} 1 & 0 & 0 \\ 0 & 0 & -1 \\ 0 & 1 & 0 \end{bmatrix} \qquad R_3 = \begin{bmatrix} 0 & 0 & 1 \\ 1 & 0 & 0 \\ 0 & 1 & 0 \end{bmatrix} \tag{4.4}$$

We assume the pre-calibration is unreliable and the rotation matrix angles are unknowns. For each camera, Table 4.2 displays the number of points employed for the calibration procedure.

The final calibration parameters are obtained by applying an iterative procedure based on least squares. To make sure the minimum residual reached is not local, various initial values are used to ensure the results do not vary.

Figure 4.10a and b provides a qualitative representation of the quality of the calibration procedure by presenting the scatter plots of the difference between the expected and measured image coordinates, $\bar{\xi} - \xi$ and $\bar{\eta} - \eta$, vs. the expected image coordinates, $\bar{\xi}$ and $\bar{\eta}$, for one of the seven views acquired by the camera #2.

To quantitatively evaluate the reliability of the entire calibration procedure, the statistics (mean and standard deviation) of the distance between expected and measured positions of grid points have been computed and results are reported in Table 4.3. Note that the mean distance is nearly always less than one pixel.

	Water calibration				**Air calibration**			
	N points	**ω_{st}**	**ϕ_{st}**	**κ_{st}**	**N points**	**ω_{st}**	**ϕ_{st}**	**κ_{st}**
Camera #1	2225	90	270	0	2375	90	270	0
Camera #2	2246	90	0	0	2451	90	0	0
Camera #3	2230	90	90	0	2429	90	90	0

Table 4.2. Data related to the calibration procedure

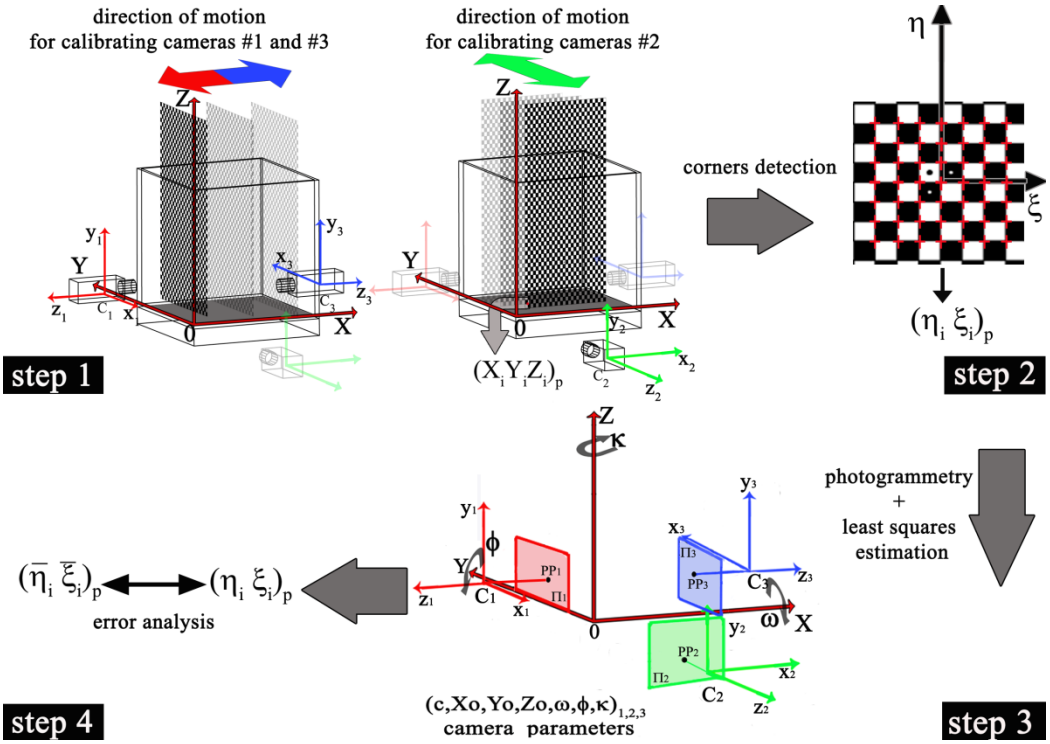

Fig. 4.9 Sketch of procedure for the stereoscopic system calibration

Water calibration									
Camera	**X0 (m)**	**Y0 (m)**	**Z0 (m)**	**c (m)**	**ω**	**ϕ**	**κ**	**mean distance (pixel)**	**st dev (pixel)**
#1	-1.0606	0.1873	0.0775	0.0354	89.99	269.68	-0.06	0.72	0.35
#2	0.1967	-1.0630	0.0721	0.0360	90.23	-0.14	0.08	0.64	0.38
#3	1.5065	0.1748	0.0659	0.0361	90.10	89.76	-0.008	1.57	0.29
Air calibration									
Camera	**X0 (m)**	**Y0 (m)**	**Z0 (m)**	**c (m)**	**ω**	**ϕ**	**κ**	**mean distance (pixel)**	**st dev (pixel)**
#1	-0.7889	0.1855	0.0777	0.0264	89.96	269.59	-0.08	0.47	0.29
#2	0.1969	-0.7873	0.0744	0.0266	90.16	-0.11	0.06	0.51	0.31
#3	1.2458	0.1754	0.0655	0.0273	90.13	89.69	-0.01	2.24	0.76

Table 4.3. Results of the calibration procedure for calibration inside water and air (we use a 25 mm lens for each camera).

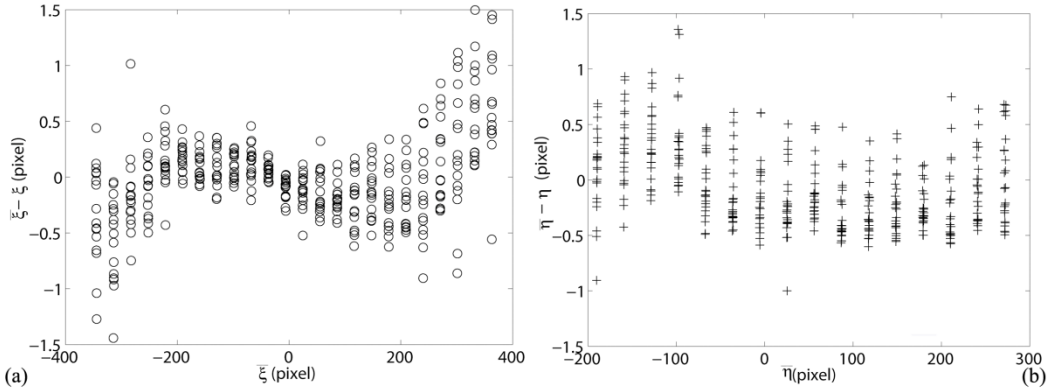

Fig. 4.10 (a) Difference between the expected image coordinate $\overline{\xi}$ and the measured image coordinate ξ vs. $\overline{\xi}$ for one of the seven views acquired by camera #2; (b) difference between the expected image coordinate $\overline{\eta}$ and the measured image coordinate η vs. $\overline{\eta}$ for one of the seven views acquired by camera #2.

Table 4.3 shows the results of calibration conducted both in water and in air; one can clearly see that water acts as a lens artificially increasing the effective focal lengths (for camera #1 the focal distance is 0.0354 m in water and 0.0264 m in air) and the distance between each camera's projective centre and the tank face orthogonal to the correspondent optical axis (the coordinates Y_0 and Z_0 of camera #1 remain substantially unchanged while X_0 is -1.0606 m in water and -0.7889 m in air, i.e. when air fills the test section instead of water the camera apparently translates along its optical axis reducing its distance from the test section).

4.2.2. Structure from Stereo

The purpose of the structure-from-stereo step is the reconstruction of the 3D geometry in a scene from two or more views taken with pinhole cameras. Two processes are involved: correspondence or matching and reconstruction. Correspondence implies estimating which points in the images are projections of the same scene point. Two cameras are enough to reconstruct a 3D image, but additional views increase confidence in the results. The coordinates of corresponding points are related by the epipolar geometry[5]. Assuming the orientation parameters of the cameras are known from the

[5] The epipolar geometry refers to the geometry of stereo vision and it is largely employed in computer vision applications. When two cameras view a 3D scene from two distinct position, there are a number of geometric relations between the 3D points and their projections onto the 2D images that lead to constraints between the image points (for more details refer to Maas et al 1993).

calibration procedure, given a point in one image, its conjugate must belong to a line in the other image, the epipolar line (Fig. 4.11).
Figure 4.11 describes the procedure to establish the stereoscopic correspondences. Starting from a point P^{I}_{1} in the first image, all epipolar lines $(EP_1)_{I\text{-}II}$ in the second image and $(EP_1)_{I\text{-}III}$, $(EP_1)_{II\text{-}III}$, $(EP_2)_{II\text{-}III}$, $(EP_3)_{II\text{-}III}$ in the third are derived where candidates $P_1^{II}, P_2^{II}, P_3^{II}$, and $P_1^{III}, P_2^{III}, P_3^{III}$ are found in the second and in the third image respectively. The particle on the intersection between the epipolar lines (P_1^{III}) will be the one we were looking for. Errors can be taken into account by introducing a tolerance ε and the search area for the corresponding particle image becomes a narrow two-dimensional band-shaped window in image space.
The 2D displacement vector between corresponding points within couples of images (called conjugate pairs) is called disparity. Reconstruction recovers the full 3D coordinates of points using the estimated disparity and intrinsic and extrinsic calibration parameters. The two most important processing steps in 3D-PTV (i.e. the establishment of spatial and temporal correspondences between particle images in simultaneous acquisitions of multiple cameras) can be handled in different ways:

- 3D particle positions determined for each time step and tracking performed in 3D space (Malik et al., 1993; Kasagi and Nishino, 1990);
- particles tracked in image space and spatial correspondences between 2D trajectories establishment (Moroni and Cushman, 2001);
- combination of image and object space based information to establish spatio-temporal correspondences between particle positions at consecutive time steps (Willneff and Gruen, 2002).

The first method is employed in the present work.

4.2.3. Trajectory Reconstruction

Tracking 3-D positions in real space instead to tracking the projections in image plane has a great advantage in term of less ambiguity. In the image plane, in fact, the positions may appear to coincide or cross and thus tracking ambiguities increase in the projected image.

To make tracking particles easier, a label (i.e. a progressive number) is given to each centroid. Let i corresponds to time $i\Delta t$ and C_i to any centroid at time i, the following operations are performed to track 3D positions in space (Fig. 4.11):

1) Starting from i= 0, the algorithm looks for all barycenters, C_{i+1}, located within a distance D_{max} (dictated by the maximum expected value of the velocity field). The algorithm may discard all the barycentres located above (below) C_i assuming that all the particles follow the direction of the flow.
2) Let r be a vector connecting C_i to one of C_{i+1} determined in step 1. The algorithm extends r to 2r and looks for barycentre C_{i+2} within a distance tol (dictated by the local acceleration) of 2r. As before only centroids located below (above) C_{i+1} are taken into account. If ambiguities arise, the nearest neighbour principle

("minimum acceleration" criterion) is employed. In other words, if more than one particle belongs to the sphere of radius toll, the particle closer to the centre of the sphere is kept. Since the centre of the sphere represents the expected position of a particle travelling with a uniform velocity, this position will represent a condition of minimum acceleration.

Steps 1 and 2 result in a sequence of 3-point trajectories.

3) To obtain possible successive points in each of these trajectories continue to repeat step 2. The algorithm first constructs triplets and then adds barycentre with increasing times to the trajectories.

The result of step 3 is a large set of possible trajectories starting at t=0. Some barycentre at time $n\Delta t$, may not have been included in these trajectories (e.g. a particle may have just entered the window of observation of the cameras). Repeat the above procedure for each i with these new initial barycentre.

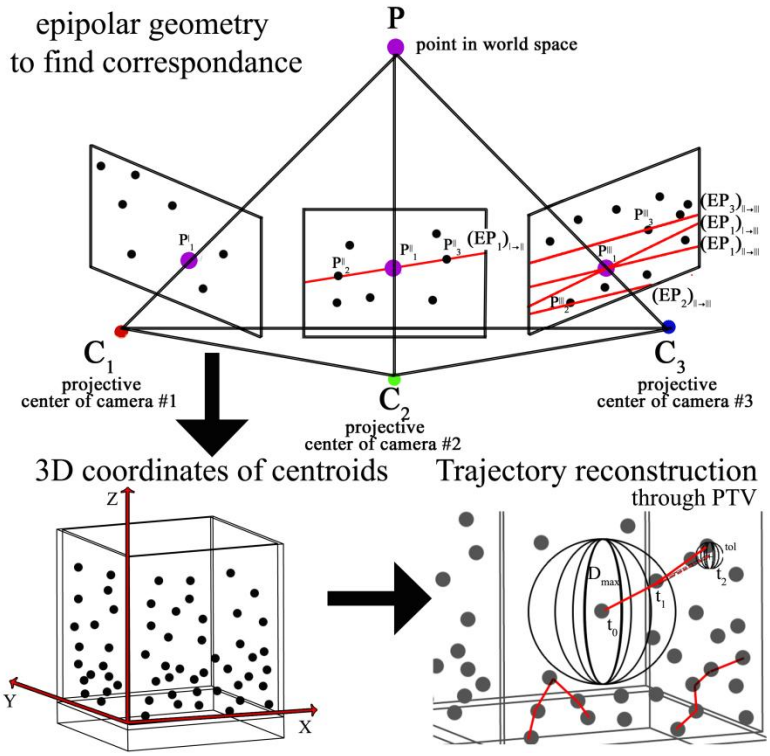

Fig. 4.11. Sketch of correspondence and reconstruction procedure, used to lengthen 3D trajectories (P_{i_i} refers to the i^{th} candidate of point P on the j^{th} view; $(EP_i)_{j-k}$ is the epipolar line of P_i on view k from view j, where i=1,2,3 and j=k=I,II,III; D_{max} is the radius of the sphere where the algorithm looks for all centroids at time t_1 dictated by the maximum expected value of the velocity field, while tol is the radius of the sphere where the algorithm looks for all centroids at time t_2 dictated by the local acceleration

4.3. Experimental data set

A set of experiments is shown in table 4.4. For each run the following features are reported:

- The image analysis technique applied
- The initial temperature gradient, γ
- The initial temperature at the bottom, T_{b0}
- The final heating temperature at the bottom, T_{bf}
- The order of magnitude of the expected final CBL height, z_{if}
- The extrapolated temperature at the top of the CBL of height z_i,T_{tf}
- The expected final Prandtl number, Pr_f
- The expected final Rayleigh number, Ra_f

In Fig. 4.12 the temperature profiles before heating starts are plotted for a sub-set of experiments in table 4.4. The initial condition of temperature for each experiment well fits a linear trend with a square correlation coefficient very close to 1 (R^2=0.99).

#	arrangement	γ	T_{bo}	T_{bf}	z_{if}	T_{tf}	Pr_f	Ra_f
		K/m	K	K	$*10^{-1}$ m	K		$*10^7$
1	2D	24.50	288.15	292.65	1.00	290.60	7.25	2.04
2	2D	51.50	287.05	298.15	1.00	292.20	6.690	6.32
3	2D	53.00	287.15	298.65	1.00	292.45	6.63	6.63
4	2D	40.50	288.39	305.15	1.00	292.44	6.12	14.50
5	2D	82.00	285.15	293.85	1.00	293.35	6.94	0.52
6	2D	47.40	286.66	292.72	1.00	291.40	7.18	1.32
7	2D	68.00	285.15	294.48	1.00	291.95	7.00	2.59
8	2D	41.10	293.76	300.00	1.00	297.87	6.10	2.43
9	2D	55.10	294.32	300.20	1.00	299.83	5.93	0.43
10	2D	29.50	294.00	299.05	1.00	296.95	6.24	2.35
11	2D	70.3	287.54	296.71	1.00	294.57	6.62	2.29
12	2D	92.59	284.58	308.15	1.00	293.84	5.77	17.00
13	2D	55.56	294.56	303.15	1.00	300.11	5.67	3.66
14	2D	70.13	293.33	303.15	1.00	300.34	5.65	3.39
15	3D	120.38	283.16	308.15	1.00	295.20	5.66	15.60
16	3D	55.29	291.92	308.15	1.00	297.45	5.49	13.20
17	3D	55.35	293.12	308.15	1.00	298.66	5.39	11.90
18	3D	101.16	286.65	308.15	1.00	296.77	5.54	14.00

Table 4.4. Set of 18 experimental runs. Main features are reported for each penetrative convection experiment.

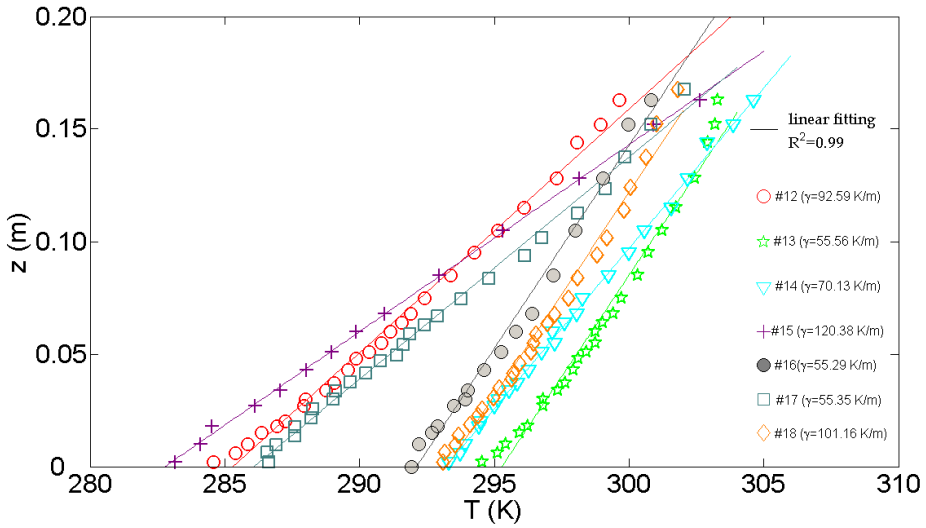

Fig. 4.12 Temperature stratification before heating starts for a sub-set of experiments in table 4.4.

4.4. Time Scaling

Given the scaling parameter for time t* as defined in eq. 2.15 we can look for the time scaling law of our experience, which allow us to simulate a similar phenomenon in nature. Introducing the measured time t and the scaled non- dimensional time $\hat{t}$ we can write:

$$\hat{t} = \left(\frac{t}{t^*}\right)_{model} = \left(\frac{t}{t^*}\right)_{nature} \tag{4.5}$$

The way to solve the problem will be:

- find t* and $\hat{t}$ in nature as a function of t;
- find t* and $\hat{t}$ in experience as a function of t ;
- look for $(\hat{t})_{model} = (\hat{t})_{nature}$ which give us a relation between t_{model} and t_{nature}.

We can use a data-set of experiences and real meteorological data to scale our model with free convection in atmosphere. For the atmosphere we use a data-set taken from University of Oklahoma on 7th of July 2003 in Norman (Oklahoma, USA). The meteorological conditions of Norman atmosphere in that day were cloudless and weakly windy so that we can assume free-convection occurred. The mixing layer growth in Norman is given in Fig. 4.13.

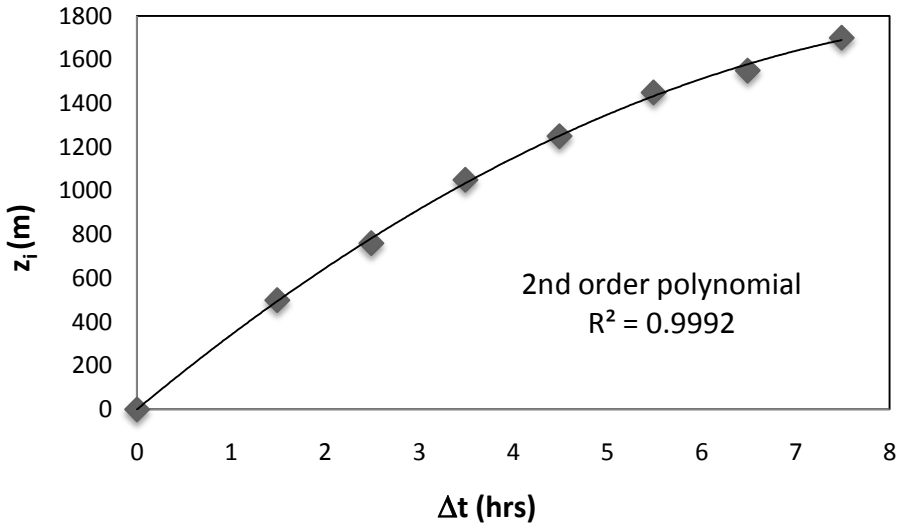

Fig. 4.13 Interpolation of real data for atmosphere in Norman taken by University of Oklahoma on 7th of July 2003. Δt is the time delay from sunrise.

Coupling the knowledge of the mixing layer growth with kinematic heat flux at the soil for the same meteorological data set, we are able to find $(\hat{t})_{nature}$ as a function of the time delay from sunrise (Δt). In Table 4.5 computed values for the surface kinematic heat flux q_s, w* t* and finally $\hat{t}$ are reported as a function of time delay from sunrise (Δt) for the real case studied.

Δt hrs	**z_i m**	**q_s m K/s**	**w* m/s**	**t* s**	**$\hat{t}$ -**
0	0.00	0.00	0.00	0.00	0.00
1.49	500.00	0.12	1.23	405.63	13.22
2.49	760.00	0.18	1.65	460.18	19.48
3.49	1050.00	0.24	2.02	520.06	24.16
4.49	1250.00	0.29	2.28	548.27	29.48
5.49	1450.00	0.34	2.51	578.59	34.16
6.49	1550.00	0.37	2.65	585.62	39.90
7.49	1700.00	0.40	2.79	608.86	44.29

Table 4.5 Values of q_s, w* t* and $\hat{t}$ computed for atmosphere in Norman on 7th of July 2003.

Given the experimental data-set in table 4.4, the scaled time $\hat{t}_{model}$ is plotted in Fig. 4.14 as a function of the measured time t_{model} for a subset of runs. The average plot (t_{model} vs $\hat{t}_{model}$) of all runs and its polynomial interpolation are then shown in Fig. 4.15.

Finally the time scaling law can be derived by combining the interpolation of experimental data in Fig 4.15 with real data in table 4.5 and constrain $(\hat{t})_{model}$ to be equal to $(\hat{t})_{nature}$. In Fig. 4.16 the time at the bench scale vs time at the real scale is plotted. Data are well fitted with a second order polynomial trend, which can be used to scale time from the bench to the real scale.

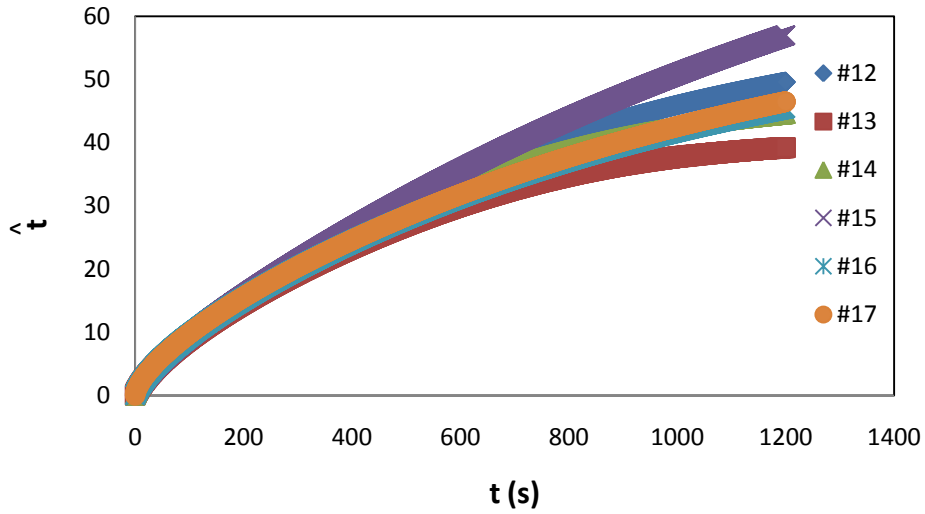

Fig. 4.14 Plot of $\hat{t}_{model}$ as a function of time for a sub-set of runs in table 4.4

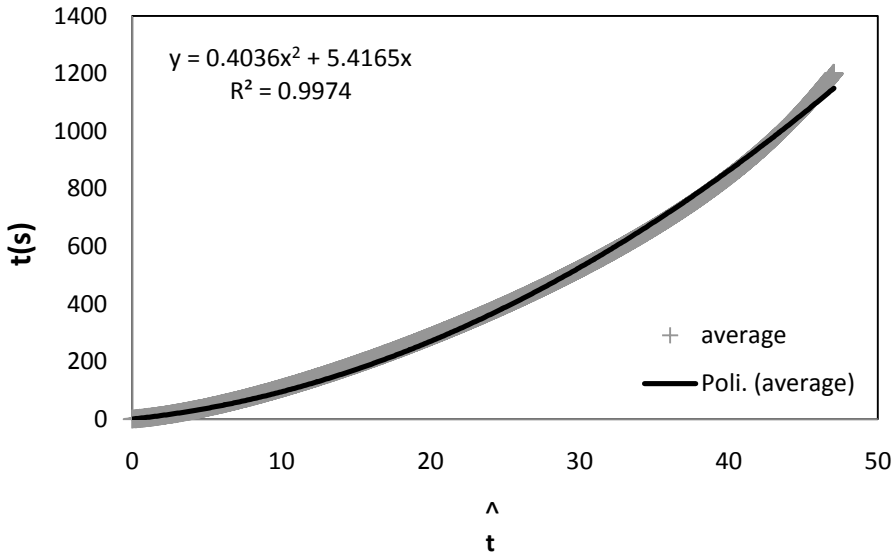

Fig. 4.15 Average plot of time as a function of $\hat{t}$ for the runs in table 4.4

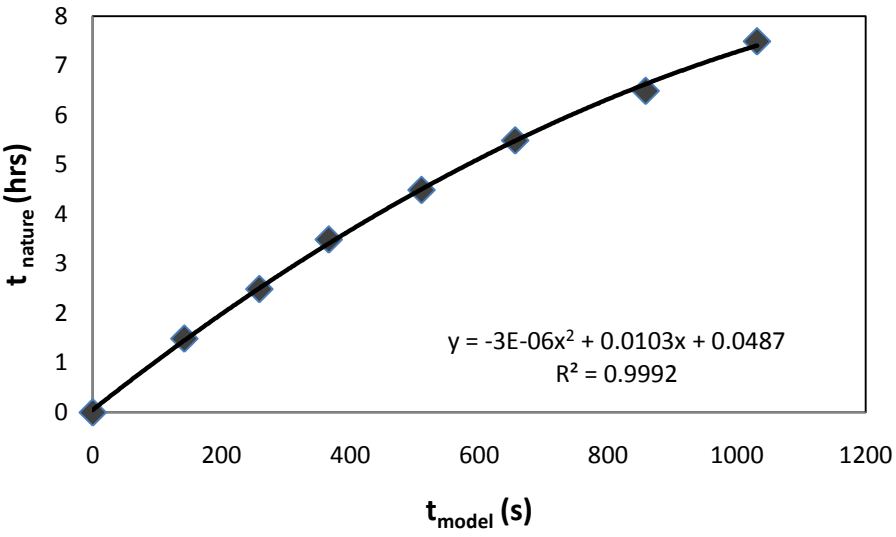

Fig. 4.16 Time at the bench scale vs time at real scale. Data well fit a second order polynomial trend.

5

2D Model: a Physical Insight

Among the experimental data set in table 4.4 characterized by initial condition in Fig 4.12, two experiments with significantly different temperature gradient (exp#12 and #13) will be presented in detail as representative of the 2D model. Exp #13 presents a temperature gradient (γ) lower than exp #12, while the final value of temperature reached at the test section bottom is slightly larger for exp #12. In this chapter the data processing will be mainly focused on give a deeper physical insight of the phenomenon.

5.1. Horizontal Homogeneity Test

As mentioned in section 4.1 the heat supply is assumed to be horizontally homogeneous for all the runs and thermocouples have been placed on the bottom surface in order to monitor if the boundary condition has been preserved. Since the horizontal homogeneity assumption will be widely used in the following analysis, a preliminary homogeneity test is thus mandatory.

The degree of homogeneity was tested in a statistical sense by analyzing sets of velocity data extracted from different locations within the mixing layer at the same height. In particular, the reverse arrangement test (Bendat and Piersol, 2000) was performed and repeated several times for different data sets (Fig. 5.1). The analysis demonstrates the horizontal homogeneity hypothesis holds with a 5% level of significance. In fact, the total number of reverse arrangements (A) falls into the interval 11-35 (i.e. the 5% level of significance interval for a number of samples equals to 10).

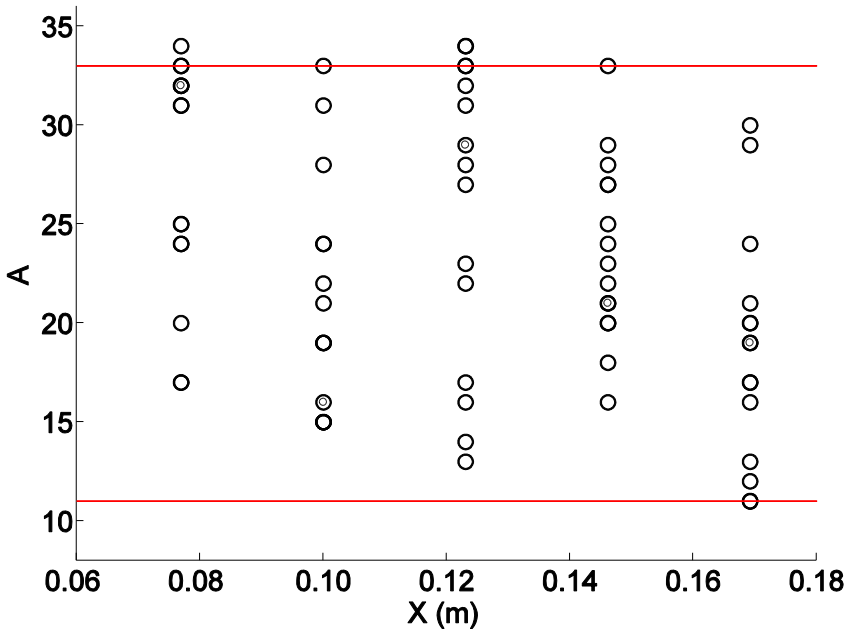

Fig. 5.1 Reverse arrangement test results for several sets of velocity data extracted from different locations within the mixing layer at the same height (Experiment #12). A is the total number of reverse arrangements (Bendat and Piersol, 2000) related to a specific set of 10 velocity data (the coordinate x is chosen as the independent variable).

5.2. CBL Growth

5.2.1. Fluorescence Imaging

In Fig. 5.2 a visualization of CBL growth using fluorescence imaging is displayed. The fluid has been dyed with sodic fluorescein, which has excitation peak at 490 nm (blue) and emission at 520 nm (green). The domain has been illuminated with a LED source of emission peak that matches the maximum excitation wavelength of fluorescein, while images are acquired using a 3CCD camera. Buoyant plumes (green region) arise as a consequence of thermal instability at the bottom and develop against the stable region above (dark region).

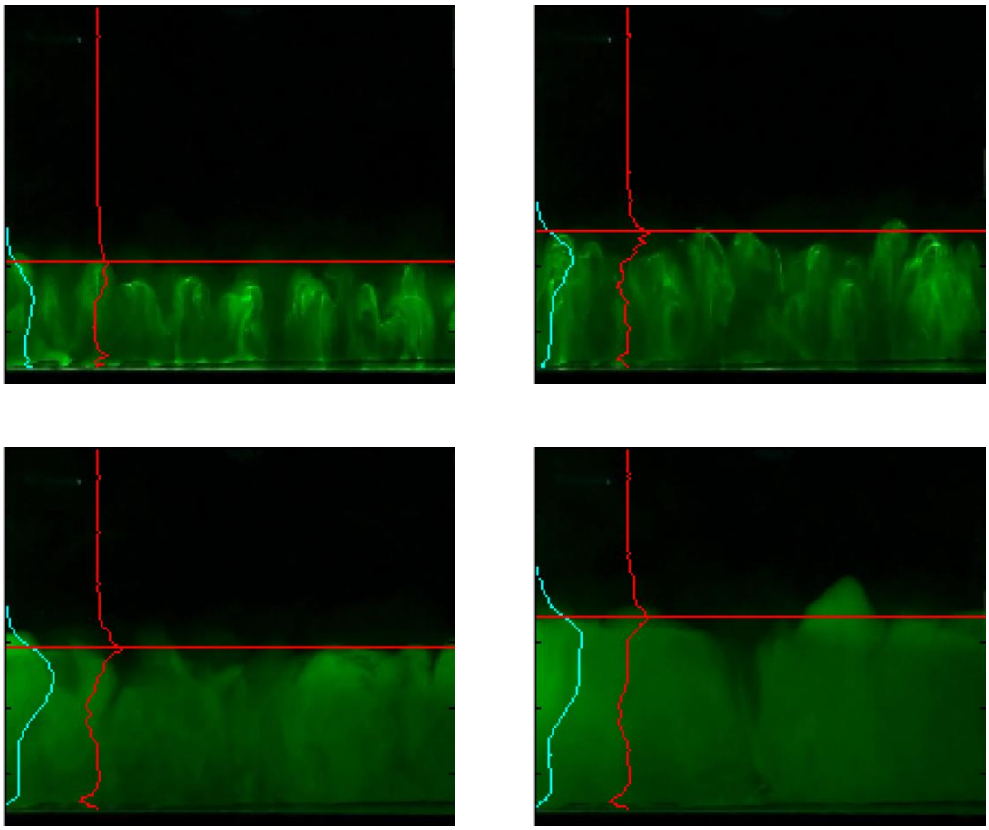

Fig. 5.2 Visualization of the CBL growth using fluorescence imaging. Buoyant plumes (green region) arise as a consequence of thermal instability at the bottom and develop against the stable region above (dark region). The cyan profile is the signal of fluorescence (i.e. the pixel intensity of the green channel) averaged over the horizontal. The upper limit of the CBL (horizontal red line) is located where the gradient of the fluorescence signal (red profile) is maximum.

As the fluorescence strength of the dye is a function of its concentration within the working fluid, the signal of fluorescence (i.e. the pixel intensity of the image green channel) can be used as a measure of mixing. More the signal became lower and homogeneous more the dye has been diluted and the fluid mixed as a consequence of mass transport. In Fig. 5.2 the signal of fluorescence (cyan profile) and its gradient (red profile), both averaged over the horizontal, are overlapped as well. The upper limit of the CBL (horizontal red line) is located where the gradient of the fluorescence signal (red profile) is maximum.

5.2.2. Temperature Data Analysis

Figure 5.3 presents vertical temperature profiles for experiment #13 (for experiment #12 profiles are qualitatively very similar). Each profile is associated with the acquisition time given in the legend even though it was obtained through averaging data acquired for 20 seconds at each thermocouple location. When heat is supplied from below, the linear temperature profile associated to the stratification inside the domain (t=0 s) starts to break up and changes with time as far as the phenomenon evolves.

Three portions characterize each profile. The portion of the profile close to the boundary presents a negative gradient related to the existence of the surface thermal boundary layer. Its height cannot be quantified because of the low spatial resolution of thermocouples in the lower boundary region. Then, the profile has a uniform temperature, $\bar{T}(t)$, where the mixed layer is located. Finally, above the mixed region, the temperature profile practically collapses onto the straight line of the initial stratification. The temperature profile in the stable layer is not noticeably affected by the growing CBL. This holds even at late stages when velocity data indicate internal wave activity in the stable layer. Profiles relative to the latest time intervals deviate from the original stratification profile and become less stable (the slope increases and the thermal gradient decreases). Vertical temperature profiles acquired during the experiment allow the growth of the CBL to be measured at different time instant ($z_i(t)$). The height can be calculated through the following relation, where $\bar{T}(t)$ is the mean temperature within the mixed layer:

$$z_i(t) \cong h_0(t) = \frac{1}{\gamma}(\bar{T}(t) - T_{s0}) \qquad (5.1)$$

$\bar{T}(t)$ is calculated by averaging the thermocouple outputs where the temperature profile is uniform. The upper limit of the convective zone and the mixing layer height do not exactly coincide, and the temperature profile should exhibit an interface layer, the entrainment zone, where the temperature homogeneity overcomes the initial stratification line (phenomenon well known as cross-over), as sketched in Fig. 2.3. Given the heating temperature, the vertical extension of the entrainment zone is expected to be greater for lower temperature gradients of the initial stratification. This is due to the weaker resistance opposed by fluids presenting large temperature gradients.
In all the experiments the temperature gradient is not low enough to observe a significant cross-over and the entrainment can be neglected in computing z_i. Equation (5.1) is then used to detect the CBL height.

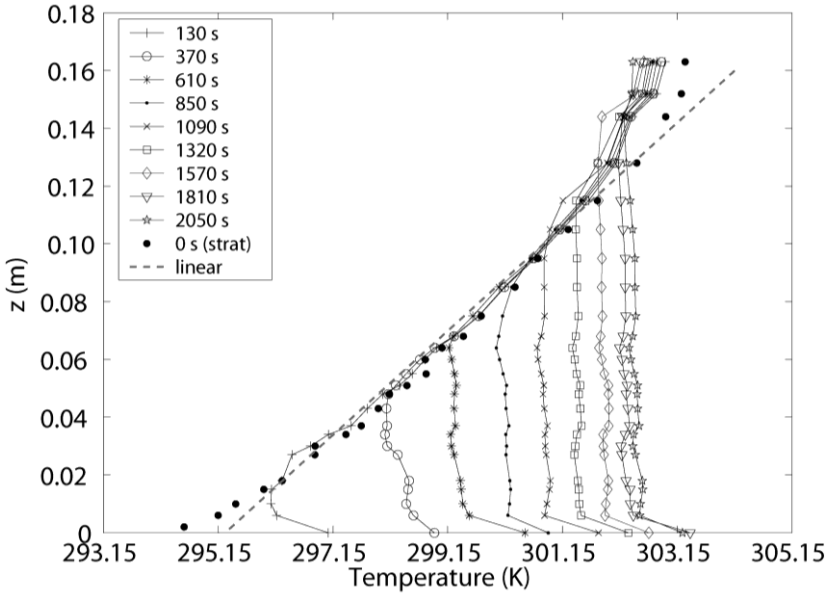

Fig. 5.3 Temperature vertical profiles for experiment #13 (the stratification profile is the one at t= 0 s). Three portions characterize each profile: the unstable surface layer at the bottom, the uniform mixed layer in the middle and the stable layer above where the temperature profile follows the initial stratification

Moreover, when the entrainment zone thickness can be neglected, the method described above coincides with the well known maximum gradient method, for which the mixed layer depth is defined as the level of the largest increase in potential temperature vertical gradient (Sullivan et al., 1998).

5.2.3. Velocity Data Analysis

The CBL height is comparable with the domes vertical dimension. Starting from this idea we can evaluate the mixing layer height with a given frequency (anyway less than 25 Hz, the largest frame rate for image acquisition) by dividing the domain into layers and computing the vertical velocity standard deviation profiles (Fig. 5.4A). The horizontal homogeneity assumption, in fact, allows averaging velocity data in each layer. We expect values of the velocity standard deviation larger inside the mixing region than in the stable layer where it should vanish. According to this expectation profiles have a typical behaviour with a maximum that became larger for longer time and an inflection point moving upward. All profiles change less as height increases further.

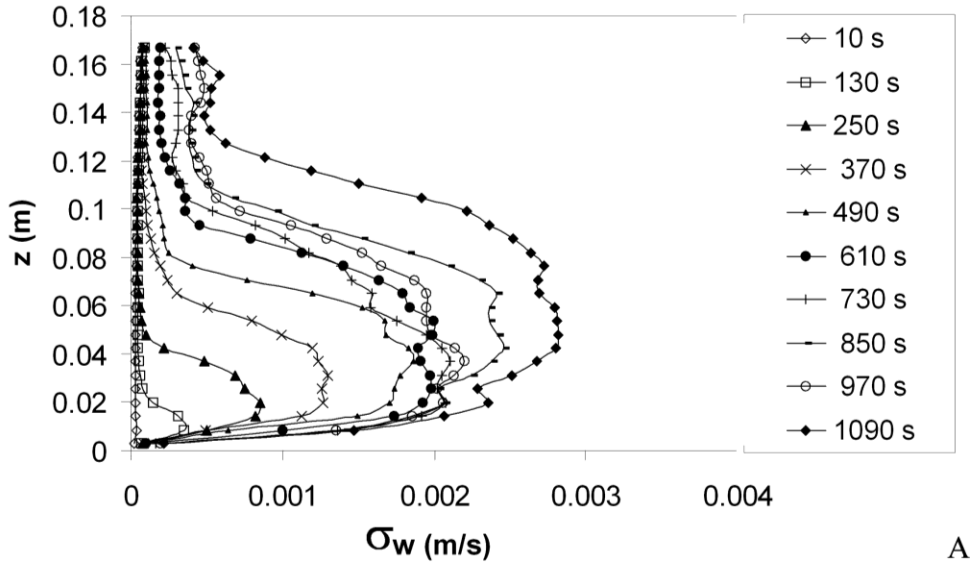

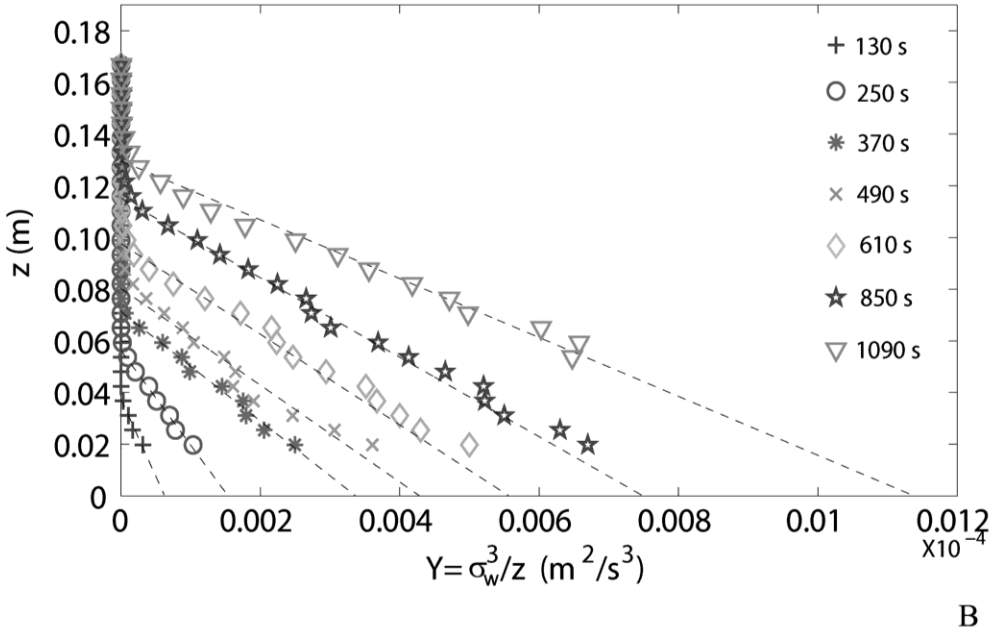

Fig. 5.4 (A) Time evolution of vertical velocity standard deviation profiles for experiment #13. (B) Time evolution of σ_w^3/z profiles for experiment #13.

For each profile in Fig. 5.4A, the height where the standard deviation became, after the peak, 30% of the maximum value and the profile slope is still gentle, is identified. z_i is then:

$$z_i(t) = \frac{1}{k} z_{30\%}(t) \qquad (5.2)$$

where $z_{30\%}(t)$ is the height associated to the standard deviation equal to 30% of the maximum value and k=0.7 is a constant empirically determined by using a larger set of experiments and findings of Cenedese and Querzoli,1994. Moreover inside a well mixed layer where mechanical production can be neglected, the $Y=\sigma_w^3/z$ profile vs z gives an approximation for the local heat flux, which linearly decreases with height vanishing by definition at $z=z_i$ (Weill et al., 1980), as shown in Fig. 5.4B. Thus, the extrapolation to zero of the linear regression of the Y profiles provides the CBL growth with time. Different cross-validating methods have then been employed and compared to compute the time evolution of the mixing layer height.

Figure 5.5 presents the superimposition of the CBL growth detected for exp #12 and #13, both employing equation (5.1) (empty dots and squares respectively) and equation (5.2) (filled dots and squares respectively). These results are then compared to the "zero heat flux level" method employing Y profiles in Fig. 5.4B (Weill et al., 1980) and to the zero-order mixing layer model, namely $z_i \sim t^{1/2}$ (Fedorovich et al., 2994).
The different methods applied show a fairly good agreement. The temperature gradient plays a dominant role in the dynamics of the mixing layer growth. Large temperature gradients correspond to a greater resistance of the stable layer to be eroded by the plume. In fact, for exp #12 the CBL height is much lower than for exp #13 even if heat provided to start and maintain convection is slightly larger.

Figure 5.6 compares three profiles, chosen among those presented in Fig. 5.4A, with the snapshots of feature trajectories up to the same times. Each profile on the right-hand side is relative to the given time, while the white straight line in the images on the left-hand side indicates the height of the CBL computed from temperature measurements. After 10 minutes approximately, the internal waves of increasing amplitude with time can be recognized in the stable layer. The region occupied by domes (i.e. the region interested by higher values of the standard deviation) overlaps very well with the region of temperature homogeneity. This evidence, coupled with the comparison of temperature-based and velocity-based methods to detect the CBL height proves that both sets of data allow the vertical extension of the convective region to be accurately computed.

In Fig. 5.7 the standard deviation profiles are normalized accordingly the Deardorff mixed-layer similarity (Deardorff, 1970), where w* is the convective velocity defined by equation (2.14). After normalization all profiles collapse on the same curve demonstrating that the phenomenon is self-similar, hence results given by different experiments and different time intervals can be compared.

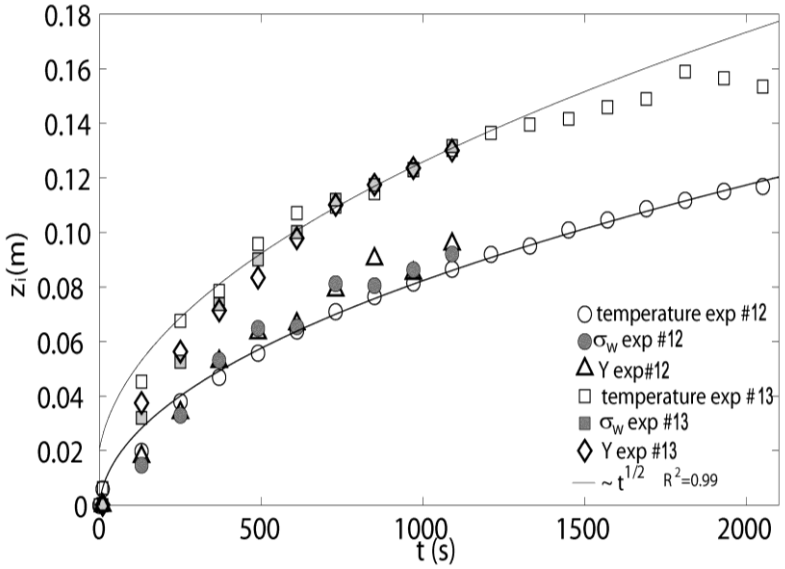

Fig. 5.5 Comparison of CBL growth for experiments #12 and #13. Temperature based method (empty markers) and velocity based method (full markers) are compared to the "zero heat flux level" method employing Y profiles in Fig. 5.4B (bold markers, Weill et al., 1980) and to the zero-order mixing layer model, namely $z_i \sim t^{1/2}$ (solid lines, Fedorovich et al., 2994).

Standard deviation profiles are also compared to atmospheric models (Fig. 5.7A, Lenshow, 74; Lenshow et al., 80), tank experiments (Fig. 5.7A, Cenedese and Querzoli, 94; Deardorff and Willis, 85; Willis and Deardorff 74) and field campaign measurements (Fig. 5.7B, Young, 88). The comparison shows a good agreement with measurements both at bench and real scale, demonstrating the validity of the experimental apparatus and its applicability for the study of the real atmospheric boundary layer and its monitoring for environmental purposes.

5.3. Horizontal Spacing of Structures

The horizontal extent of domes can be investigated through the spatial correlation of the velocity field within the CBL, which is defined as follows:

$$R_{u_i u_j'}(\mathbf{x}_1, \mathbf{x}_2, t) = \overline{u_i'(\mathbf{x}_1, t)\, u_j'(\mathbf{x}_2, t)} = \int_{-\infty}^{\infty}\int_{-\infty}^{\infty} u_i'(\mathbf{x}_1, t)\, u_j'(\mathbf{x}_2, t)\, p(u_i', u_j', t)\, du_i' du_j' \qquad (5.3)$$

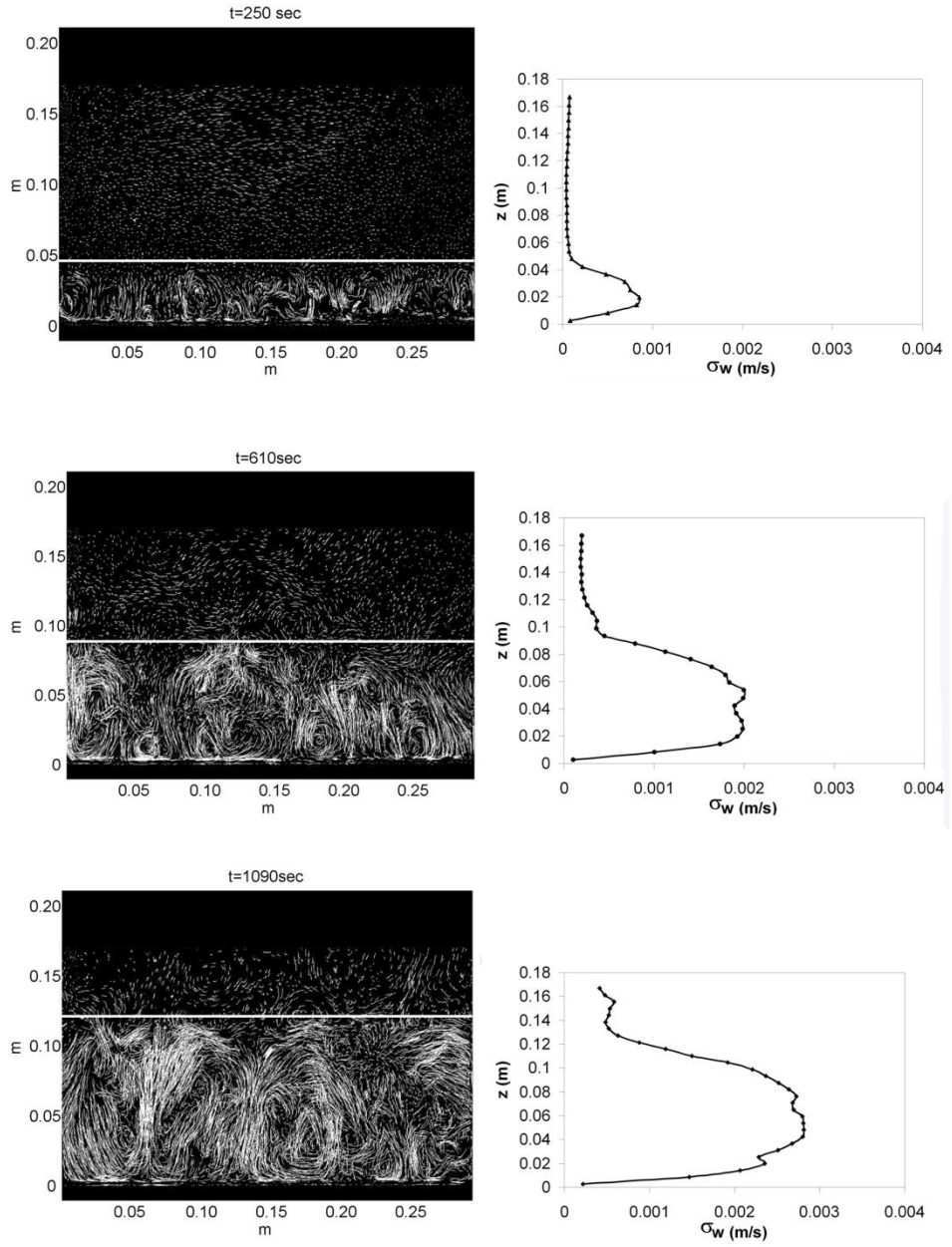

Fig. 5.6 Time evolution of vertical velocity standard deviation profiles compared to the mixing layer height evolution derived quantitatively from temperature measurement (solid lines overlapped onto images) and qualitatively from trajectories observation (experiment #13)

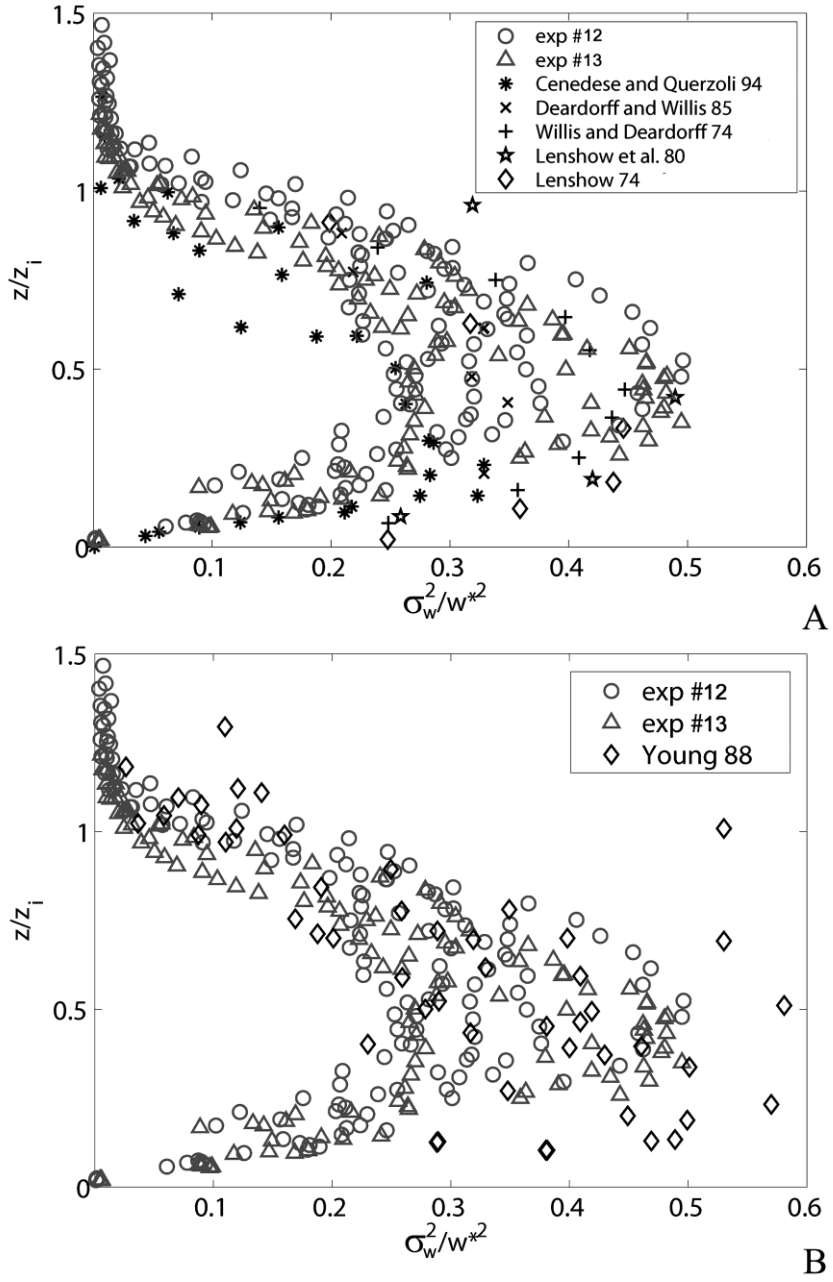

Fig. 5.7 Normalized standard deviation of vertical velocity compared with atmospheric models, tank experiments (A) and field campaign data (B) found in literature.

where the fluctuating part of each velocity component, u_i' and u_j' (if i=j we obtain the autocorrelation function), are measured at points $\mathbf{x}_1$ and $\mathbf{x}_2$ and at time t, $p(u_i', u_j', t)$ is the joint probability density function. Setting $\mathbf{x}_1 = \mathbf{x}$ and $\mathbf{x}_2 = \mathbf{x} + \mathbf{r}$ it is

$$R_{u_i' u_j'}(\mathbf{x}_1, \mathbf{x}_2, t) = R_{ij}(\mathbf{x}, \mathbf{r}, t) \tag{5.4}$$

If the assumption of horizontal homogeneity is satisfied, the spatial correlation is only function of $|\mathbf{r}|$, the height z and time t, i.e. $R_{ij}(z, |\mathbf{r}|, t)$.

Figure 5.8 presents the spatial correlation of the vertical component of the velocity field for three instants of time. Velocity vectors belonging to a layer centred on the convective region centreline are taken into account. The oscillating behaviour of each line allows the transverse dimension of the plumes within the mixing layer, for a given time the correlation refers to, to be evaluated. The characteristic dimension of those structures increases with time. For small times, the number of velocity samples belonging to the layer within the mixing region taken into account to compute the correlation is inadequate to gather a statistically acceptable result. For large times, the structure dimension becomes comparable to the test section side and the wall effects are not negligible. The wall effects appears as anomalies and drifts both in temperature and velocity data profiles for large times (Fig 5.3 and 5.4A). This then suggests the velocity data analysis is meaningful since about 1000 second from the beginning of the experiments.

The correlation goes toward zero faster for smaller time, congruently with the expected smaller dimension of the structure; moreover, the dome horizontal characteristic dimension increases with time. The distance between two peaks in each plot is compared with the distance between two domes. Notice the results are in a good agreement for each time instant presented.

5.4. Transilient Matrices

In Fig. 5.9 transilient matrices (section 1.2.1) for six different non-dimensional time lags are exhibited. Recalling the Deardorff mixed layer similarity (1970) and the non-steadiness of the phenomenon, normalization is a necessary step in order to compare data not acquired simultaneously. Each matrix, after normalization, can be considered time independent and independent from the condition of experiment as well.

Although the spatial extent of each bin increases with Δt^* due to the increase of the mixing layer height, the matrices are plotted with respect to the origin and destination depths in order to simplify their physical interpretation. The destination index increases from the bottom to the top. Height will then increase upwards.

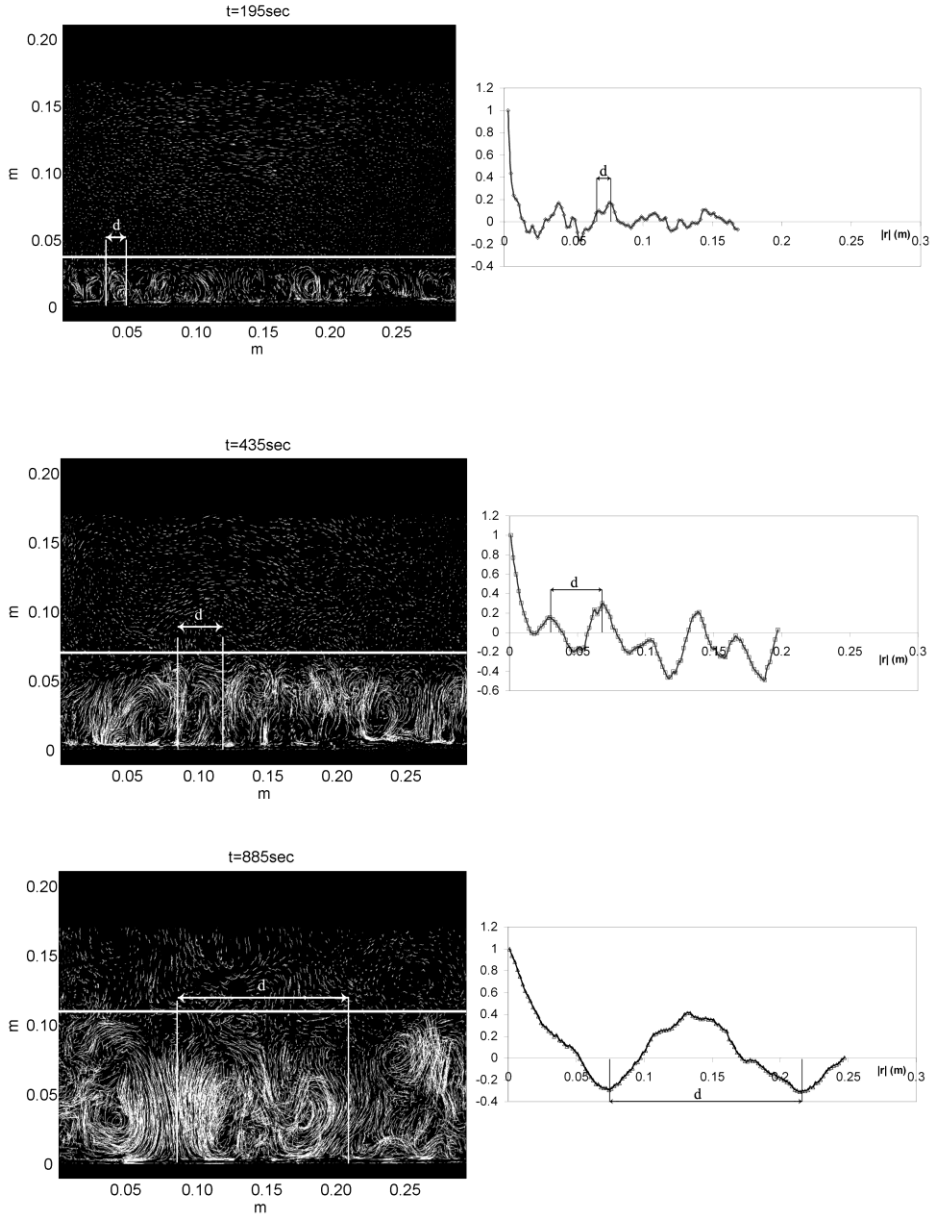

Fig. 5.8 Spatial autocorrelation of the vertical component of the velocity field for three times (experiment #13). Velocity vectors belonging to a layer centred on the convective region centreline are taken into account. The distance (d) between two peaks in each plot is compared with the distance between two domes, visualized through the trajectories at the same time.

One can clearly see that at the beginning ($\Delta t^* = 0.01$) all the elements along the main diagonal are close to one, meaning that the fluid is at rest and no mixing occurs. As convection evolves inside the CBL the matrices become more and more dispersed showing a faster mixing for greater non-dimensional time lags. For large time lags ($\Delta t^* > 0.4$) tracer spreads out almost uniformly within the mixing layer and the transilient matrix assumes uniform values in that area. Moreover the asymmetry on the contours plot demonstrates that the transport is preferentially downward.

Figure 5.10 presents cross sections through the transilient matrices in Fig. 5.9 at a fixed source depth (0.675). As elements of TM are fraction of fluid moved from the source to the destination layer, each curve can be conceived as a concentration probability density function. The concentration begins as a δ function at the source depth, marked with a continuous line, and progressively more disperse curves correspond to later times. The dotted line marks the boundary of convection zone. If a local closure of the ADE could be applied cross sections through the matrix would yield Gaussian which would progressively decrease in amplitude and increase in dispersion with time. To verify the likelihood of the concentration profiles to a Gaussian distribution, second order central moment (i.e. variance,) and third, fourth order normalized central moments (i.e. skewness and kurtosis) are computed [6] and plotted in Fig. 5.11 as a function of the non-dimensional time lag. The increasing trend of the second order moment implies an increasing volume of fluid interested by the presence of the scalar. The third order moment shows how the concentration distribution moves away from symmetry while the dispersion, related with the mixing layer growth, is going on. As the distributions are positively skewed, the centres of mass are translated downward in respect to the source, meaning that a preferential downward mass transport does exist. Finally the concentration profiles tend toward a symmetrical distribution for long time intervals. In general the distribution curves are never Gaussian, as the kurtosis value, which always differs from 3, demonstrates. The analysis proves the non local approach to be mandatory.

---

[6] The x^{th} order normalized central moment is defined as: $\mu_x^* = \frac{\mu_x}{\sigma^x}$ where μ_x is the x^{th} order central moment of the variable.

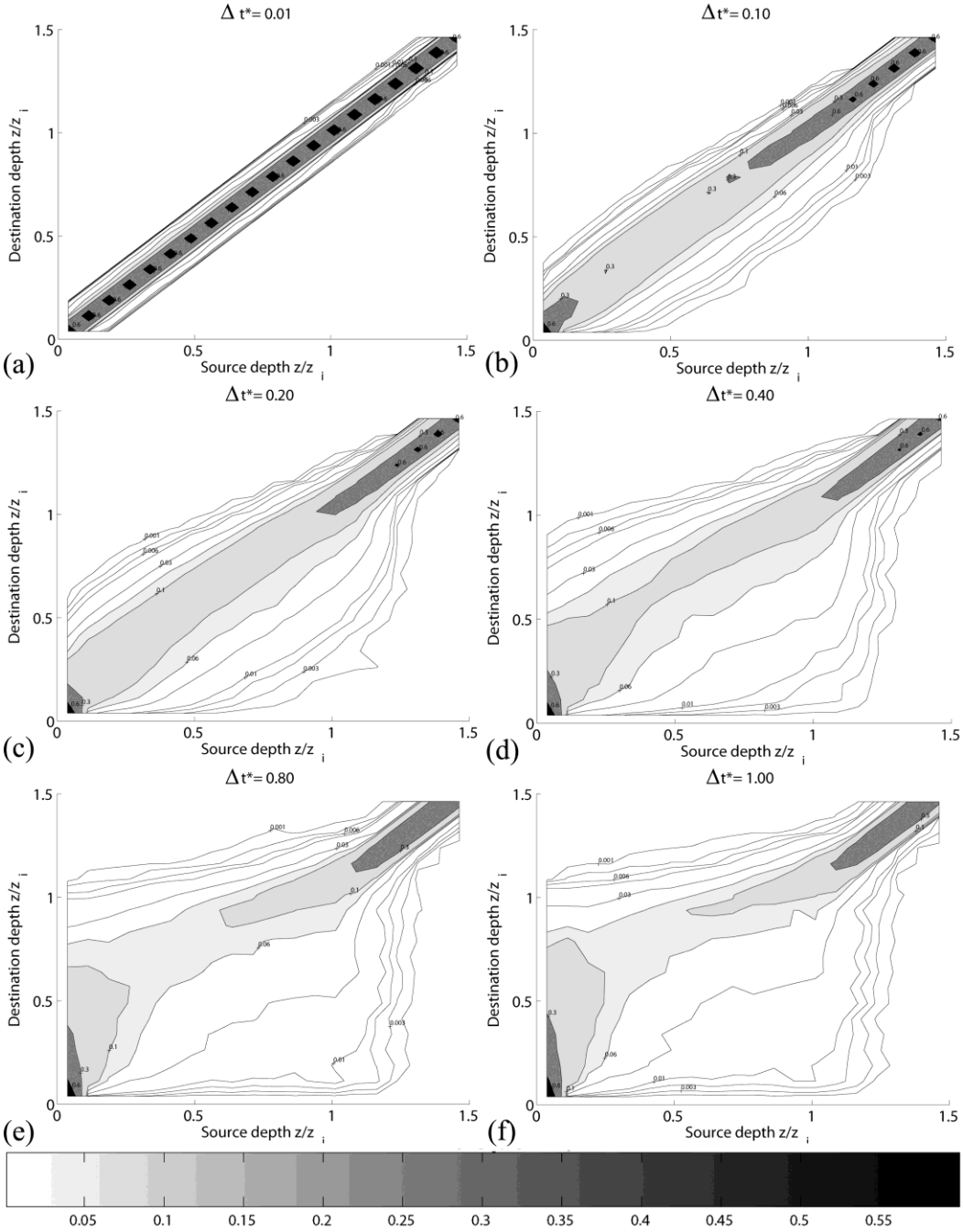

Fig. 5.9. Normalized Transilient matrices for various non-dimensional time lags.

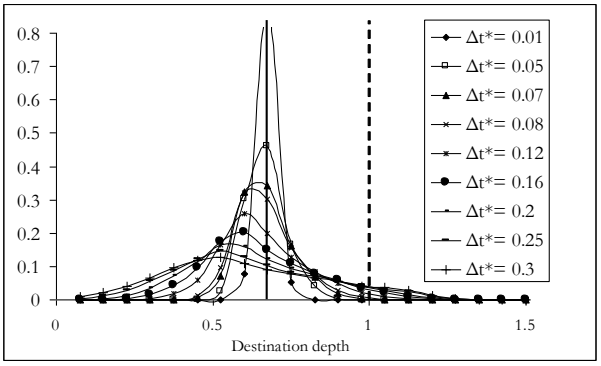

Fig. 5.10. Cross section of the transilient matrices at a fixed source (z/z_i=0.675) for various non-dimensional time lags. The concentration begins as a δ function at the source depth, marked with a continuous line, and progressively more disperse curves correspond to later times. The dotted line marks the boundary of convection zone.

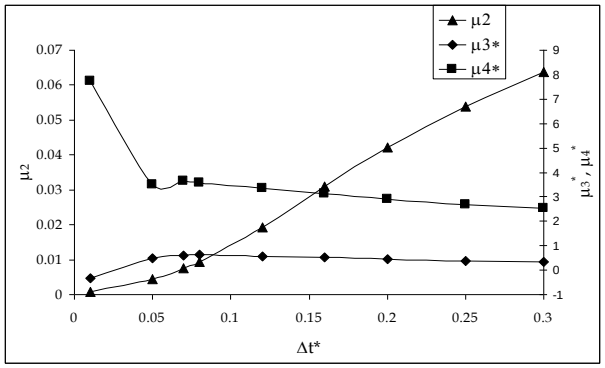

Fig. 5.11. Variance (triangle marker), skewness (diamond marker) and kurtosis (square marker) of curves in Fig. 5.10. The increasing trend of the variance implies an increasing volume of fluid interested by the presence of the scalar. All the curves are positively skewed and differ from Gaussians having the kurtosis not equal to three.

6

3D Model: Algorithm validation based on synthetic trajectories

Driven by the idea that only a fully three-dimensional technique can significantly improve our laboratory model in term of a more likely description of three-dimensional free convection structures, a photogrammetric 3D-PTV technique has been applied as described in section 4.2. Once the stereo-system calibration has been developed and optimized, different algorithms for the spatio-temporal matching and reconstruction have been developed and tested as well. This chapter is mainly focused on testing the performance of different algorithms through a synthetic generated data-set in order to optimize the technique for the following application to real experimental data, which the chapter 7 will be entirely dedicated to.

6.1. Features of the Synthetic Data Set

Matching algorithms have been tested on a synthetically generated data set simulating curling trajectories in a volume of dimensions similar to the ones employed for the experiments (Fig. 6.1).

The starting location of each trajectory is randomly distributed in a region close to the bottom of the observation volume, particles are assumed to remain in the lighted volume and the mean velocity is constant for each trajectory. Particles are allowed to move along the positive direction of the Z axis. The synthetic trajectory lengths (in SI units) are similar to those expected in the experiments.

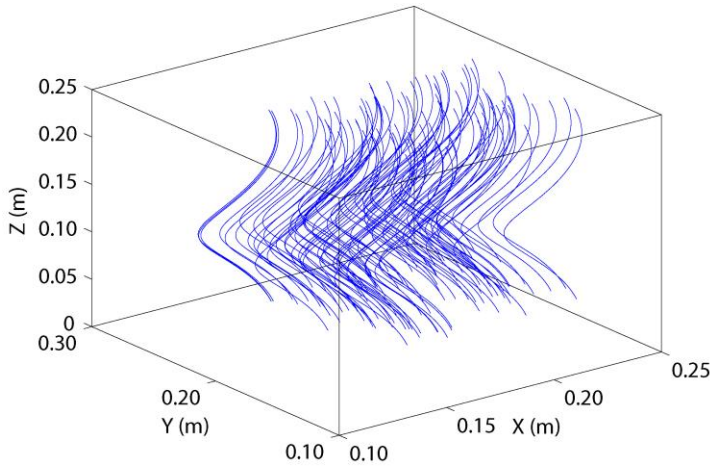

Fig. 6.1 Synthetically generated data set simulating curling trajectories in a volume of dimensions similar to the ones employed for the experiments

6.2. Sensitivity Tests

Different sensitivity tests have been performed and here presented. Recalling the epipolar geometry to find correspondences between multiple views of the same scene (section 4.2.2), two strategies of matching have been tested in term of their sensitivity to:

- density of seeding particles
- number and arrangement of cameras
- error in calibration parameters

6.2.1. Algorithm Strategy

Starting from the idea that at least two different views of the same scene have to be acquired for the 3D reconstruction, two strategies of matching have been tested:

1) the one-choice strategy chooses the only single doublet (if two view are employed) or triplet (if three views are employed) with the smallest sum of the distances from the corresponding epipolars and epipolar intersections which satisfy the tolerance constraint in each view;
2) the multi-choice strategy chooses all the doublets or triplets whose distances from the corresponding epipolars and epipolar intersections satisfy the tolerance criterion for each view.

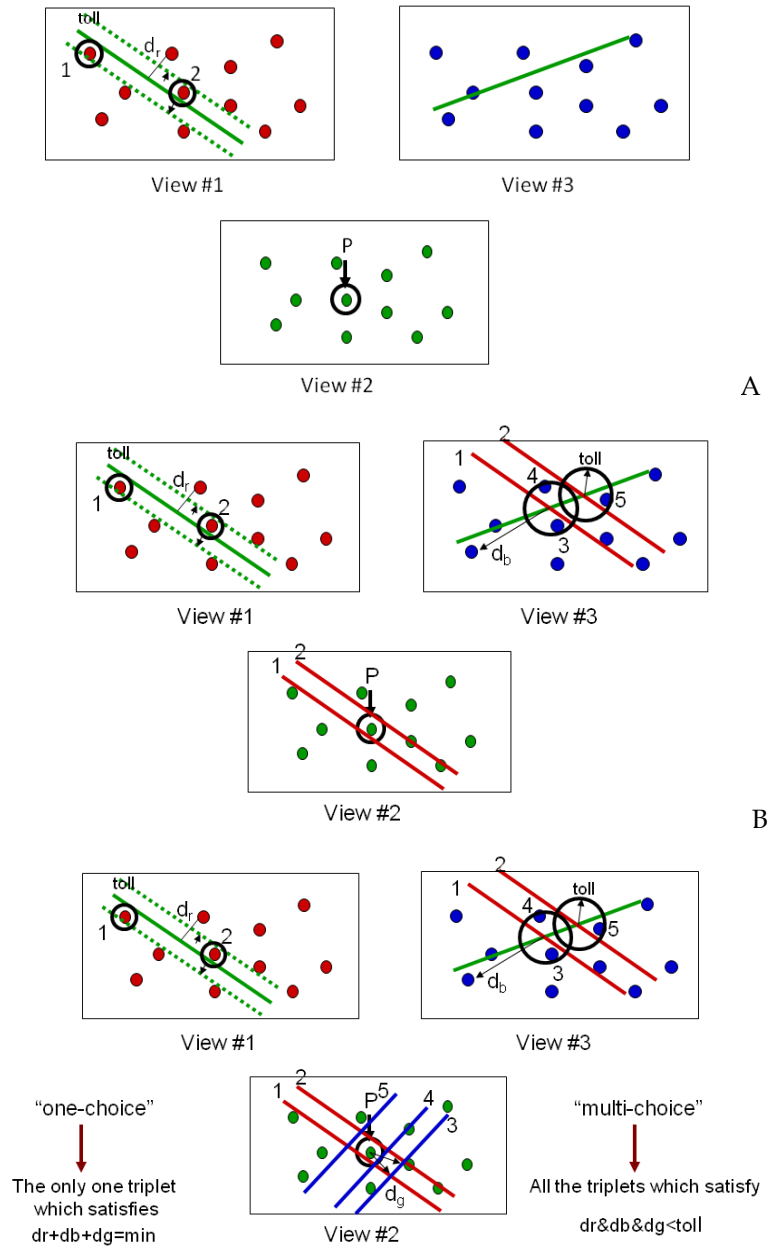

Fig. 6.2 Sketch of the matching algorithm strategies tested. The one-choice strategy chooses the only one triplet for which the quantity $d_r+d_b+d_g$ is minimum, while the multi-choice strategy chooses all the combinations which satisfy the tolerance criterion in all the views.

In Fig.6.2 the description of the two strategies is sketched, for three views of the same scene. Given a fixed tolerance (toll) in pixels, start from the one particle in the view #2 (P) and compute its epipolar lines on the other two views (green lines in Fig. 6.2 A). Suppose to find two possible candidates in the first view (1,2), which satisfy the tolerance criterion (d_r<toll, where d_r is the distance between a generic particle and the green line). Compute their epipolar lines (red lines in Fig. 6.2 B) on the second and third views and search for all candidates in the view #3 which satisfy the tolerance criterion (d_b<toll, where db is the distance between a generic particle and the green-red epipolar intersections). Suppose to find three possible candidates in the third view (3, 4, 5), we can go back to the second view (Fig. 6.2C), compute their epipolars (blue lines in Fig. 6.2C) and finally filter all the candidates which do not satisfy the tolerance criterion on the third view (d_g<toll, where dg is the distance from the point P and the red-blue epipolar intersections). At the end, if the one-choice strategy would be applied the only triplet for which the quantity $d_r+d_b+d_g$ is minimum will be chosen (i.e. P, 1, 4). On the contrary if the multi-choice strategy would be applied all the combinations which satisfy the tolerance criterion in all the views will be kept as possible triplet.

6.2.2. Density Tests

The effect of increasing the number of particles seeding the measurement volume (from 100 to 2000 particles) was tested on the matching procedure. We expect that performances will decrease with an increasing particle density. Particle tracking is very sensitive to seeding density as the latter could significantly increase the ambiguity in matching and tracking procedures. The ghost and overlapping particle problem is well known in classical PTV and it exponentially increases as the particle density increases, reconstructing short and unreliable trajectories.

6.2.3. Camera Arrangements

3D-PTV requires viewing the sample volume from two or more directions. The performance of the matching algorithms has been tested by using both 2 and 3 cameras. The ideal setup for obtaining highly accurate trajectories (Becker *et al.*, 1999) requires the cameras to be mounted with the distance between them equal to the distance to the centre of the measurement volume. However, the camera arrangement is usually a compromise between ideal geometrical conditions in the measuring volume and practical restrictions associated with the experiment. For this reason three different three-camera set-ups (labelled A, B and C) have been tested (Fig. 6.3).

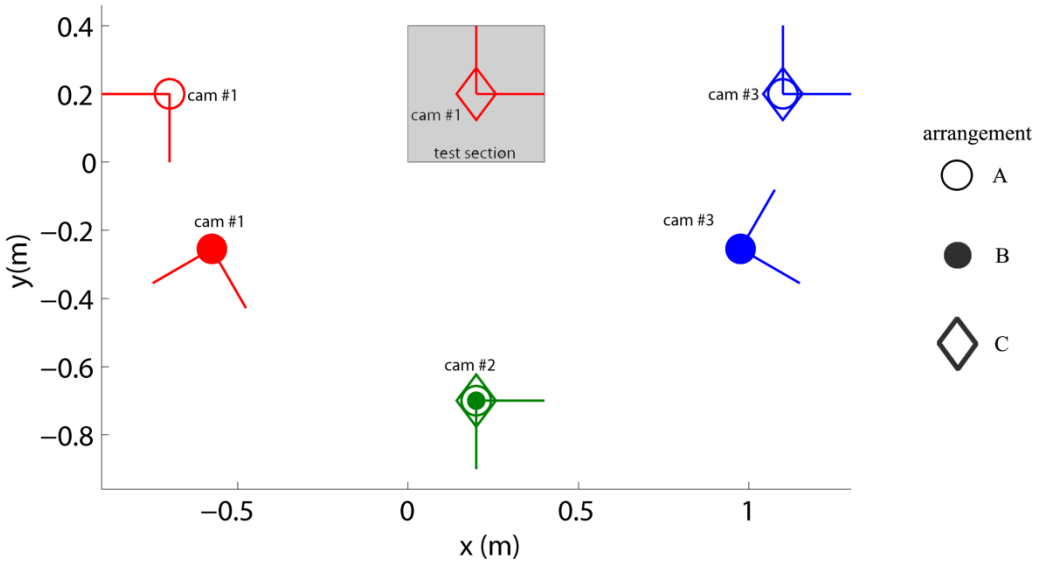

Fig. 6.3 Top view of the three stereo arrangements tested with synthetic trajectories. The three empty dots refer to arrangement A, the three full dots to arrangement B and the three diamonds to arrangement C. All camera positions are in the (x,y) plane at z=0.14 m, except for camera #1 of arrangement C which is at z=1.00 m. Note that cam #2 of the three arrangements coincides as well as cam #3 of arrangements A and C.

Arrangement A corresponds to a three camera set-up with optical axes lying on the same plane and forming an angle of 90° with the closer camera (the arrangement is employed in the present set of measurements); Arrangement B presents three cameras with optical axes lying on the same plane and forming an angle of 60° (this arrangement is used by Moroni *et al.*, 2009); Arrangement C presents three cameras with optical axes of each couple of cameras forming an angle of 90° (this arrangement is used by Di Giuseppe *et al.*, 2009). For each arrangement, the synthetic three-dimensional trajectories have been projected on the image plane of the two (#1 and #2) or three cameras (#1, #2 and #3) replicating the exterior and interior calibration parameters of the acquisition system employed.

Arrangement	"err1"	"err2"	"err3"	"err4"	"err5"
A	2	5	8	11	15
B	2	6	9	12	16
C	1	2	3	4	5

Table 6.1 Projection error in pixels as a function of the stereo arrangement and the error in the calibration parameters ("err1" indicates a 0.01% error added, "err2" a 0.03 %, "err3" a 0.05 %, "err4" a 0.07 %, "err5" a 0.09%)

6.2.4. Error in Calibration Parameters tests

The effect of a wrong evaluation of the calibration parameters was investigated as well. In this case, the projections were calculated by employing a fixed set of calibration parameters (the correct ones, "err0"), while the reconstruction was carried out by using a modified set of calibration parameters by introducing an arbitrary error in percentage ("err1" indicates a 0.01% error added, "err2" a 0.03 %, "err3" a 0.05 %, "err4" a 0.07 %, "err5" a 0.09%).
Despite the small error added, the projection error in pixels it determines is significant and highly dependent on the camera arrangement (table 6.1).
To determine the projection error we have employed a 3D grid of dimensions equal to the investigated volume and known tie-point coordinates in the world reference frame. Table 6.1 displays the largest value of the quantity $\sqrt{(\Delta\xi_i)^2+(\Delta\eta_i)^2}$, i.e. the squared difference between "correct" and "corrupted" grid projection coordinates (i refers to a generic grid point). The influence of the camera arrangement on the projection error is high. In particular, Arrangement C is less sensitive to the error in the calibration parameters always providing errors in pixels lower than arrangements A and B. The error was computed with a sub-pixel accuracy but it has been reported as an integer in Table 6.1 (consistent with the tolerance (in pixel) introduced in the matching procedure).

6.3. Algorithm Performances

The 3D positions of matched centroids output by the 3D-PTV algorithm, fed with the projections of the 3D trajectories for each arrangement, are compared to the synthetically generated data set to determine the percentage of successfully reconstructed object point locations. The tolerance may introduce ambiguities in determining the doublets (for the two-camera arrangements) or triplets (for the three-camera arrangements) corresponding to the same point in the 3D scene.

The analysis of synthetic data demonstrates the correctness of the matching algorithm since it provides 100 % of correctly matched doublets or triplets for all stereo arrangements, all particle densities and no error in the calibration parameters. The

algorithm performances strongly decrease when the projection error in pixels becomes larger than the tolerance, set to 3 pixels in all cases.

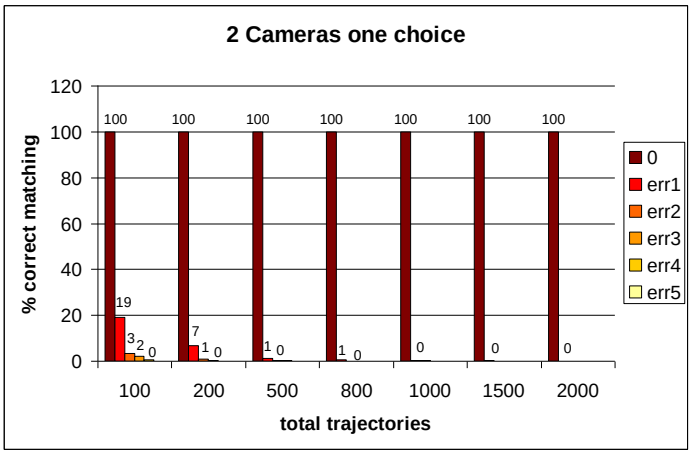

(a)

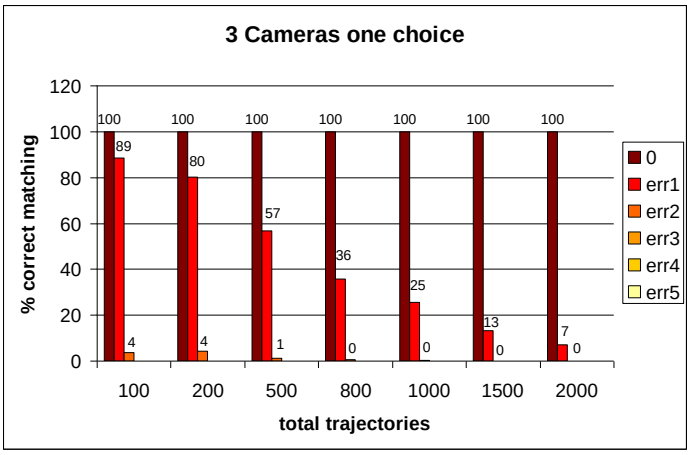

(b)

Fig. 6.4 Matching performances for the one-choice strategy and arrangement A with two cameras (a) and three cameras (b) as a function of increasing error in the calibration parameters and increasing particles feeding the illumination volume

6.3.1. One-choice Strategy

The results of the analysis of synthetic data with two-camera arrangements and one-choice strategy are synthesized in Figs 6.4a (arrangement A), 6.5a (arrangement B) and 6.6a (arrangement C). The number of doublets of the algorithm output equals the number of particles filling the observation volume for all the arrangements and set of

calibration parameters employed, but the number of correctly matched doublets decreases with both increasing particle density and error in the calibration parameter set.

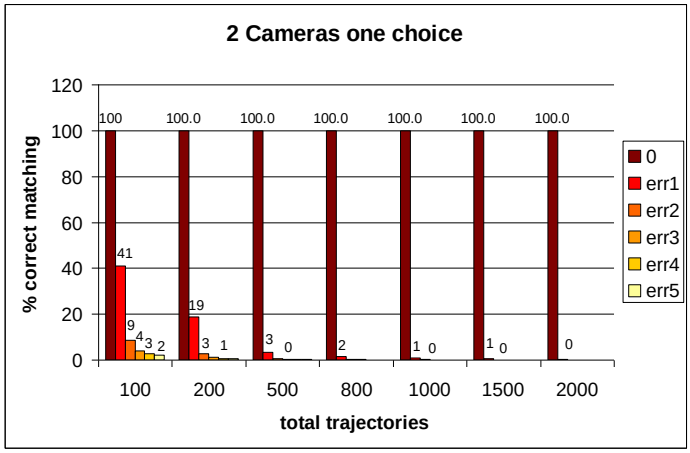

(a)

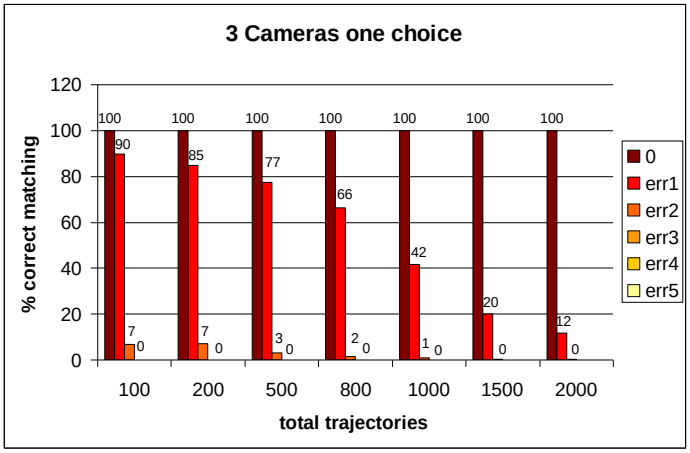

(b)

Fig 6.5 Matching performances for the one-choice strategy and arrangement B with two cameras (a) and three cameras (b) as a function of increasing error in the calibration parameters and increasing particles feeding the illumination volume.

The smallest error in the calibration parameters ("err1") yields a strong decrease in the algorithm performance for Arrangements A and B (i.e. when 100 particles are inserted in the observation volume, the percentage of correctly matched doublets is 19 % for Arrangement A, 41 % for Arrangement B and 99 % for Arrangement C; when 200 particles are processed, 7 % (14 particles) are properly matched with Arrangement A, 19% (38 particles) with Arrangement B and 99 % (198 particles) with Arrangement C). This result does not change if the tolerance is increased. Arrangement C yields better

performance of the matching algorithm, confirming it is less sensitive to error in the calibration parameters (Table 6.1).

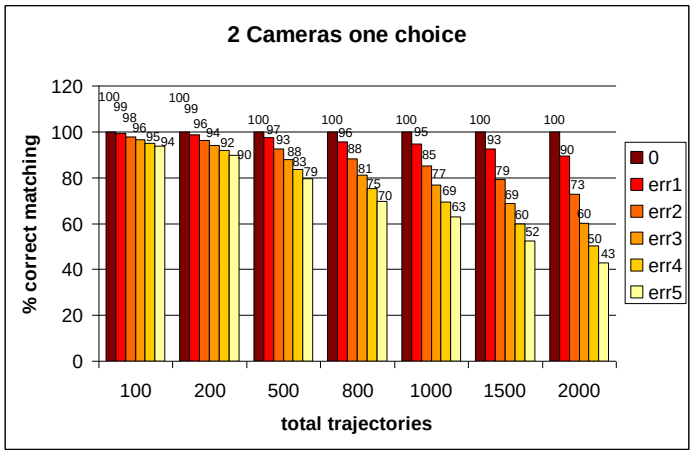

(a)

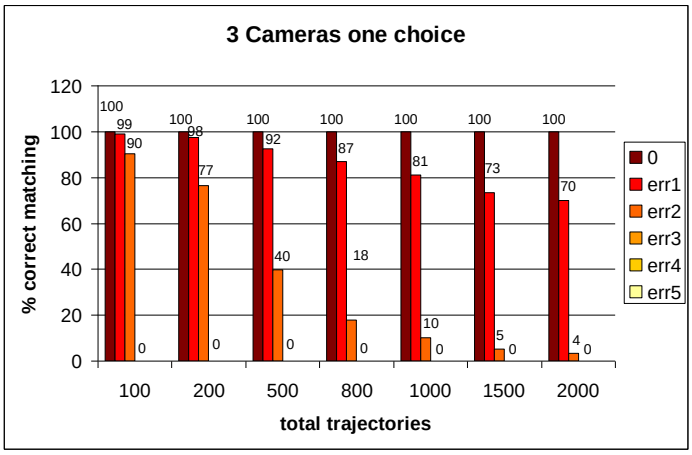

(b)

Fig. 6.6 Matching performances for the one-choice strategy and arrangement C with two cameras (a) and three cameras (b) as a function of increasing error in the calibration parameters and increasing particles feeding the illumination volume

It should also be noted that Arrangement C is more suitable to reconstruct the 3D position of our designed synthetic data set when 2 cameras are employed because of the shape of the trajectories which present similar features when projected according to Arrangements A and B but are substantially different in the Arrangement C because it is the only one that presents a top view of the scene. We believe this does not challenge the

validity of our test because Table 6.1 clearly shows Arrangement C was influenced the least by the calibration parameter errors on the data set employed.

The results of the analysis of synthetic data with three-camera arrangements and one-choice strategy are synthesized in Figs 6.4b (arrangement A), 6.5b (arrangement B) and 6.6b (arrangement C).

The number of triplets the algorithm outputs equals the number of particles within the observation volume for all the arrangements and sets of calibration parameters with an error less than the tolerance employed. Arrangements A and B perform better, with a percentage of correctly matched triplets always larger than the corresponding case with the two-camera arrangements. When 100 particles are inserted within the observation volume, 19 particles are correctly matched with the two camera Arrangement A, whereas 89 are correctly matched with the three camera Arrangement A.

6.3.2. Multiple-choice Strategy

The results of the analysis of synthetic data with two-camera arrangements and multi-choice strategy are summarized in Figs 6.7a (arrangement A), 6.8a (arrangement B) and 6.9a (arrangement C). The number of doublets of the algorithm output is much greater than the number of particles filling the observation volume for all the arrangements and set of calibration parameters employed.

The matching algorithm performances largely improve, with the percentage of correctly matched doublets always larger than 90 % for errors “err1”, “err2”, “err3” and all arrangements. On the other hand, the number of doublets output by the matching algorithm increases by more than one order of magnitude for low particle densities (until 200 particles) and more than two orders of magnitude for high particle densities (more than 500 particles) for arrangements A and B, increasing the computational costs and producing possible ambiguities in the tracking procedure. This is clearly shown in Figs 6.10a,b and c which present the difference of doublets and particles within the observation volume divided by the number of particles filling the observation volume in percentage vs. the number of particles for arrangements A, B and C respectively and no errors in the calibration parameters.

The performance of the matching algorithms when three-camera set-ups are employed largely improves, demonstrating the need for more than two views for the correct reconstruction of a 3D scene.

The results of the analysis of synthetic data with three-camera arrangements and multi-choice strategy are synthesized in Figs 6.7b (arrangement A), 6.8b (arrangement B) and 6.9b (arrangement C). Also in this case, the matching algorithms perform better because even if the percentage of correct triplets drops for large errors in the calibration parameter set, the significantly lower number of triplets (i.e. ambiguous particles to be tracked, see Fig.6.10) output by the algorithm compensates for the lower performance if compared to the two-camera case, and suggests the introduction of a third view. On the other hand, the multi-choice strategy, compared to the one-choice strategy, always

allows 100% of correctly matched triplets for small calibration errors producing projection errors in pixels lower than the tolerance. This motivates the three camera multi-choice strategy is employed to match the real data.

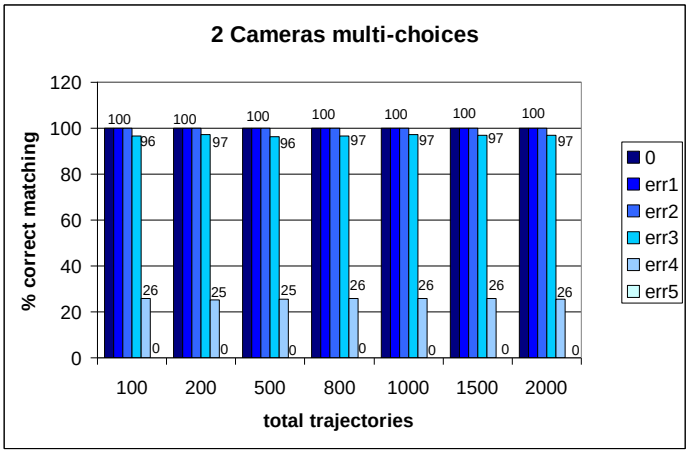

(a)

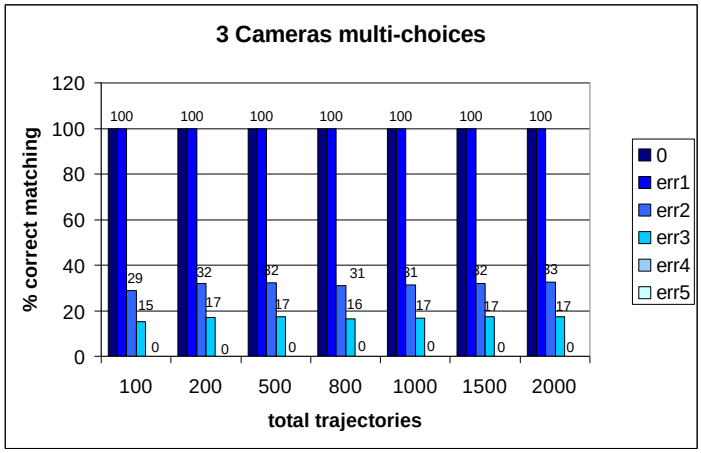

(b)

Fig. 6.7 Matching performances for the multi-choice strategy and arrangement A with two cameras (a) and three cameras (b) as a function of increasing error in the calibration parameters and increasing particles feeding the illumination volume.

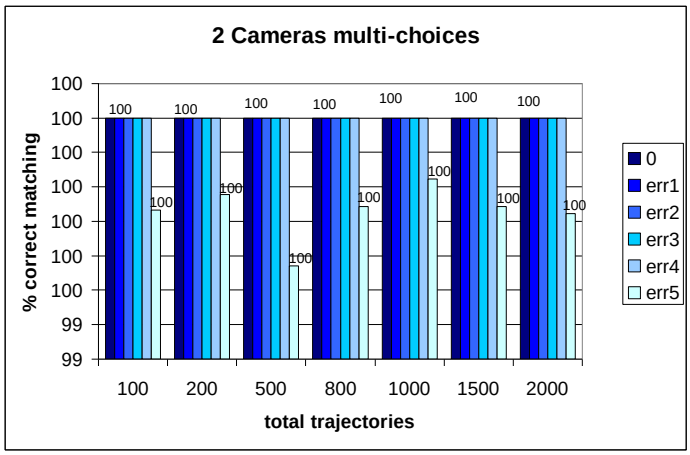

(a)

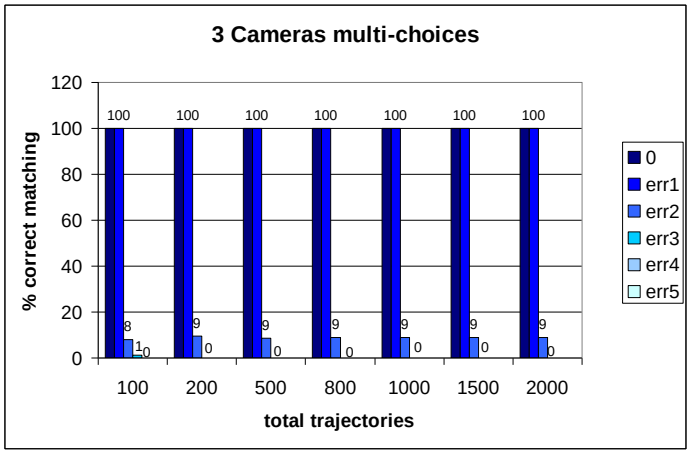

(b)

Fig. 6.8 Matching performances for the multi-choice strategy and arrangement B with two cameras (a) and three cameras (b) as a function of increasing error in the calibration parameters and increasing particles feeding the illumination volume.

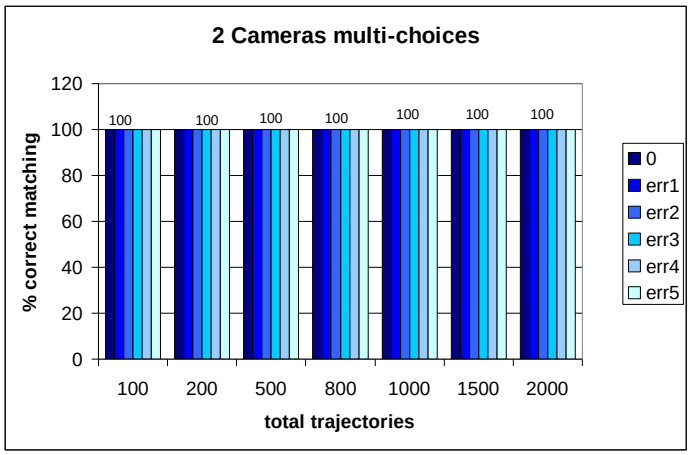

(a)

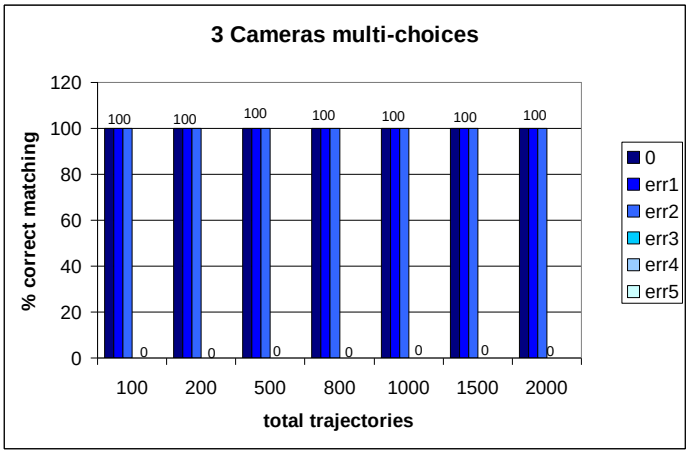

(b)

Fig. 6.9 Matching performances for the multi-choice strategy and arrangement B with two cameras (a) and three cameras (b) as a function of increasing error in the calibration parameters and increasing particles feeding the illumination volume.

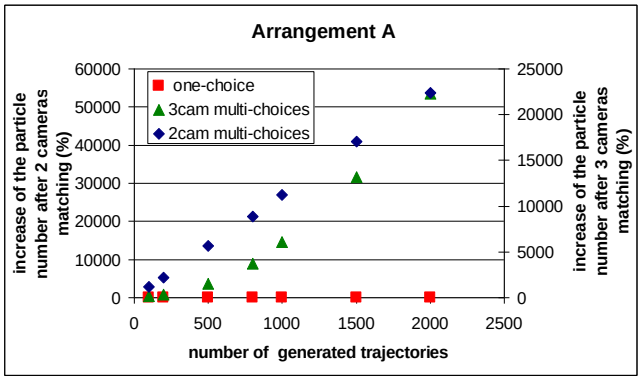

(a)

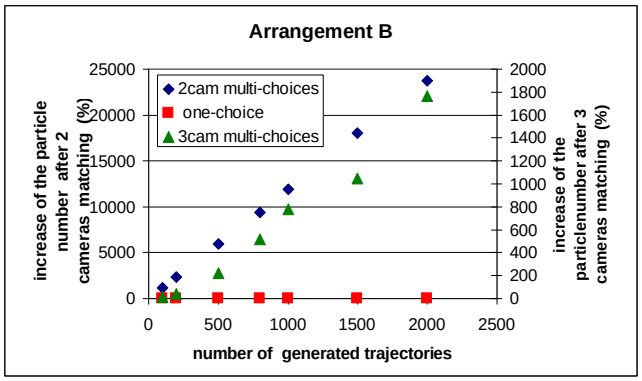

(b)

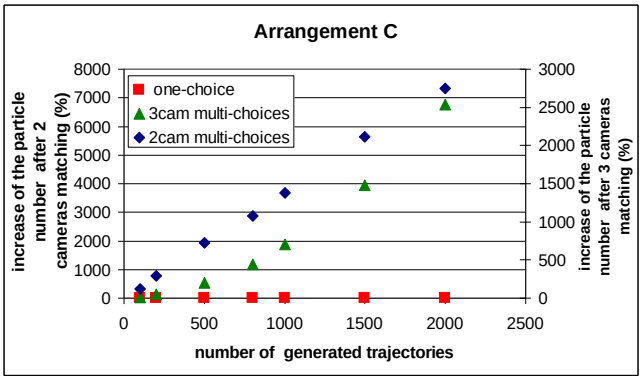

(c)

Fig 6.10 (a) Increase of the number of matched couples (without errors in the calibration parameters) relative to the number of particles feeding the observation volume in percentage vs. the number of particles for arrangement A; (b) the same for arrangement B; (c) the same for arrangement C.

7

3D Model: Application to Real Images

Among the experimental data set in table 4.4 characterized by initial condition in Fig. 4.12, two experiments with significantly different temperature gradient and similar to those analysed in chapter 5 (exp#17 and #18) will be presented in detail as representative of the 3D model. Exp #17 presents a temperature gradient (γ) lower than exp #18, while the final value of temperature reached at the test section bottom is the same for both the experiments. In this chapter the data processing will be mainly focused on the application and validation of the three-dimensional tracking technique described in chapter 6 rather than physics. Driven by this aim comparison between different methods in terms of their accuracy, between two dimensional and three dimensional measurements and between experimental models and numerical results will be presented

7.1. Experimental Data-set

Two experiments are presented in this chapter (exp#17 and exp18 of table 4.4). Fig. 7.1 displays the initial temperature profiles before heating starts. The measured profiles overlay to a linear interpolation that is very close to the experimental data in both cases. When heating from below begins, the temperature profile changes with time as the phenomenon evolves (Fig. 7.2) as we have already described in Section 5.2.1.

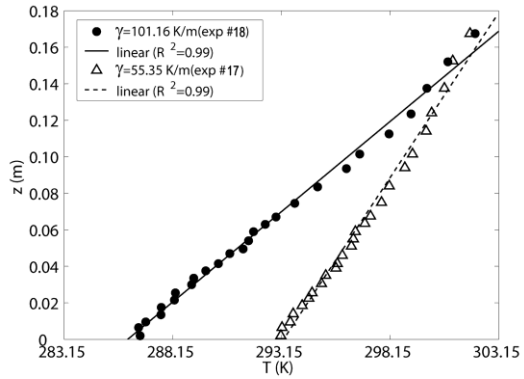

Fig. 7.1 Initial temperature profiles for experiments #17 and #18 of table 4.4

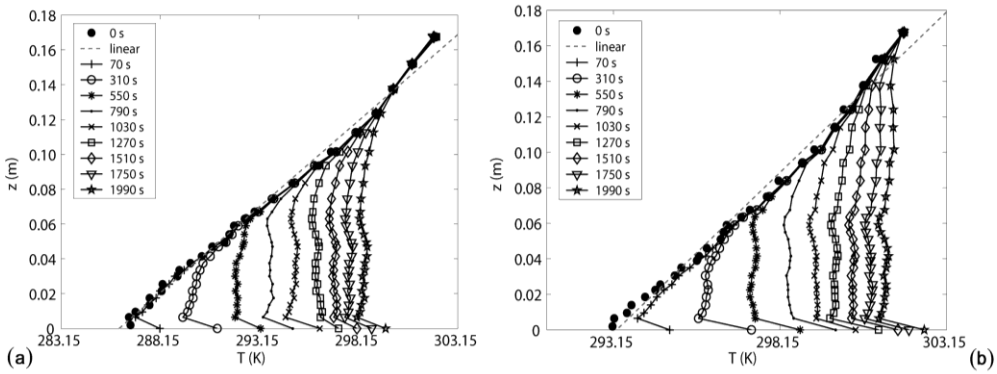

Fig. 7.2 (a) Vertical temperature profiles during heating for experiment #18 and (b) experiment #17

7.2. Centroids and Trajectories

The stereoscopic system, properly calibrated as described in section 4.2.1, and the matching-reconstruction algorithms, tested and optimized with synthetic data as described in the previous chapter, have been applied to real images to track tracer particles in penetrative convection experiments.

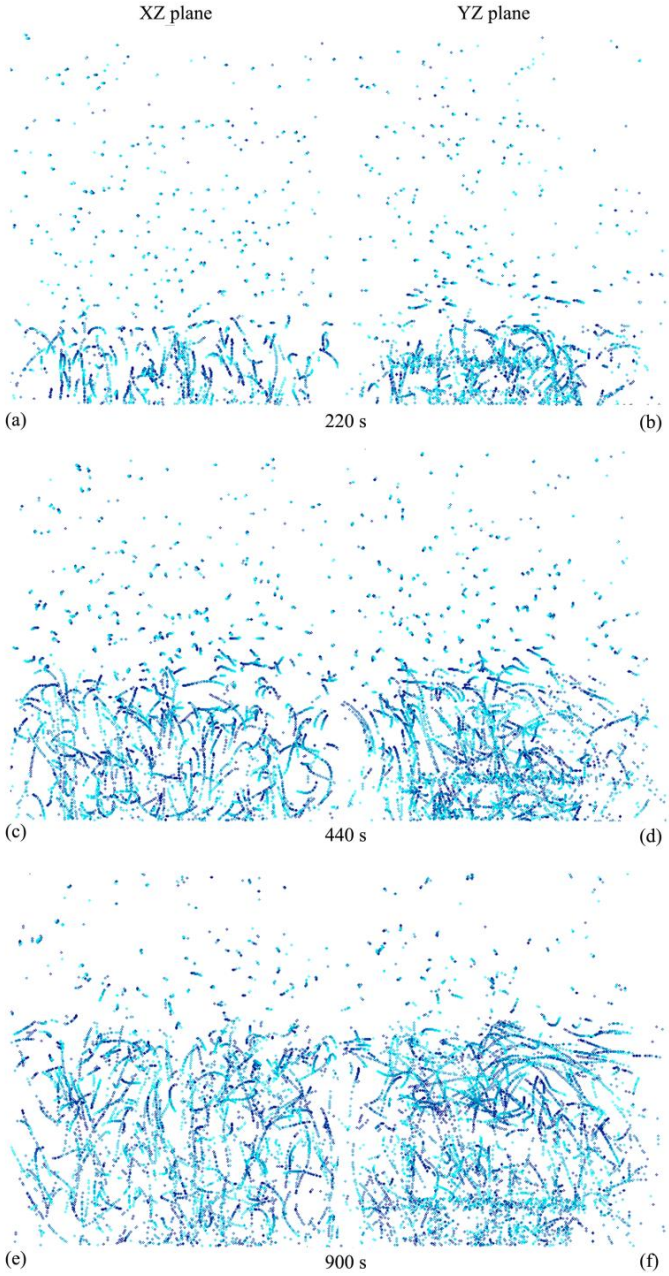

Fig. 7.3 Projections on the XZ plane (a, c, e) and YZ plane (b, d, f) of matched centroids after 220 s (a, b), 440 s (c, d), 900 s (e, f) from the beginning of experiment #18. In both pictures, 50 s are overlaid and dark colour refers to later times (exp#18 of Table 4.4).

Figure 7.3 shows matched centroids projected on the XZ plane (a, c, e) and the YZ plane (b, d, and f) inside both the stable and the unstable layers after 220 s, 440 s and 900 s from the beginning of experiment #18 and tracked for at least 50 seconds. Darker colours have been linked to later times, while lighter colours to earlier times. The algorithm finds an order of magnitude of 1000 trajectories longer than 20 spots. From both projections it can be clearly seen that the turbulent region below is moving upward against the almost quiet stable layer. The 3D-PTV procedure is suitable for reconstructing the displacement field (i.e. particle trajectories) in both the mixing and the stable layer.

7.3. CBL Growth

The velocity data obtained from the 3D trajectories have been used to obtain quantitative results for the CBL height evolution. Since dispersion in turbulent convective phenomena is mostly due to transport by large organized structures, the knowledge of the vertical extension of the structures dominating the flow field, associated to the CBL height, is a necessary requirement (Chapter 5).

The CBL growth is computed from the vertical velocity standard deviation profiles (Fig. 7.3) employing the method described in section 5.2.3 and equation 5.2. Three dimensional measurements give us the possibility to obtain more robust statistics in each horizontal layer in which the domain has been subdivided.

The CBL height evolution found exploiting standard deviation profiles is plotted in Fig. 7.5. Results using velocity data are compared to the ones obtained using the temperature data, showing good agreement. Error bars of z_i are also plotted for both the two methods employed. They are computed starting from the 90% confidence interval for the vertical velocity standard deviation $\left(\sqrt{\mu_2}\right)_w$ based on the sample standard deviation σ_w and the chi-square function, and from the 90% confidence interval for the mean temperature μ_T based on the sample mean $\overline{T}$ and t-Student function (Bendat and Pearsol, 1971). The number of independent samples is computed by observing the autocorrelation coefficient. The evaluation of z_i by using temperature data seems to be statistically more accurate for later times, but it is not for earlier times due to the low number of samples. On the contrary the velocity-based method is very sensitive to the irregular shape of standard deviation profiles.

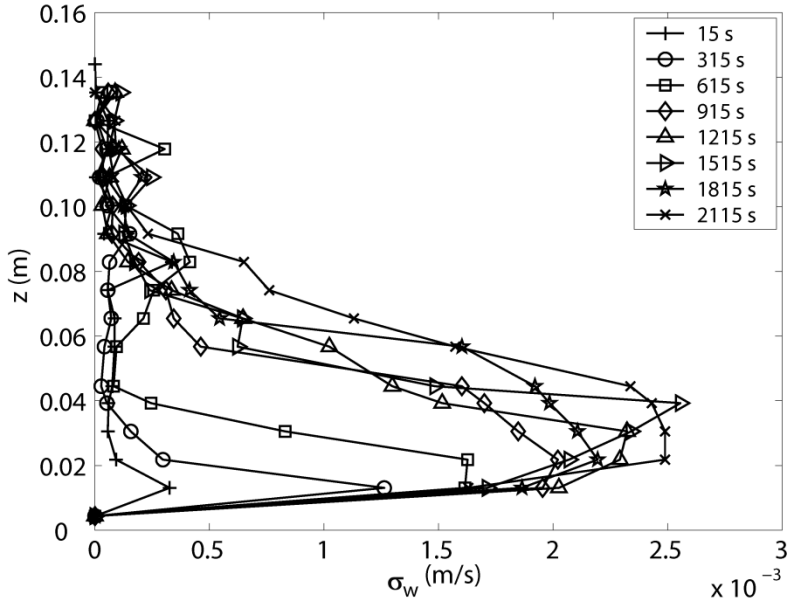

Fig. 7.4 Standard deviation profiles of the vertical velocity at different times for experiment #18

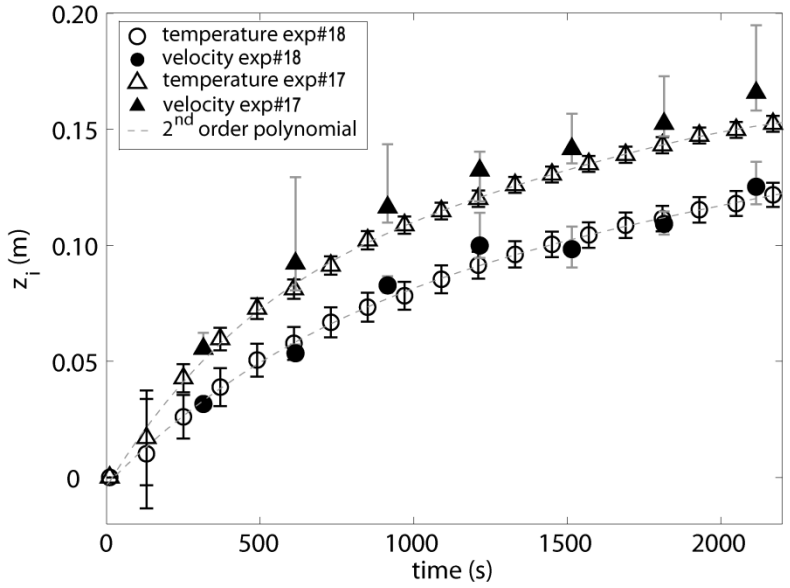

Fig. 7.5 Comparison of the CBL height evolution computed by temperature (empty markers) and velocity (full markers) measurements for exp #17 and #18.

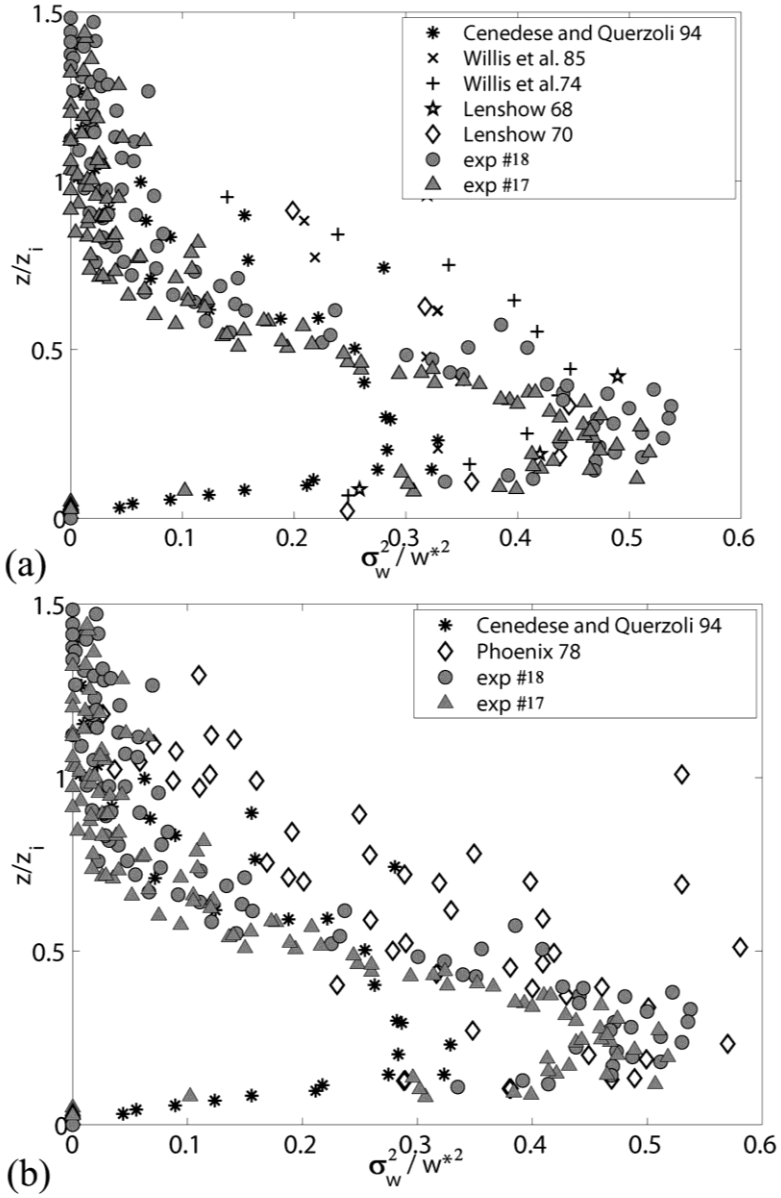

Fig 7.6. Standard deviation of vertical velocity profiles normalized accordingly the Deardorff mixed layer similarity (Willis and Deardorff, 1974) compared with (a) atmospheric models and 2D tank experiments and (b) 2D tank experiments and field measurements.

7.4. Comparisons

Figure 7.6 presents the standard deviation profiles normalized accordingly the Deardorff mixed layer similarity (Deardorff, 1970), by employing the convective velocity, w*, and the mixing layer height, z_i, found through temperature measurements. After normalization, all profiles collapse on the same curve, losing the dependence on time and particular conditions of the experiment. The observation of normalized profiles proves that the mixing layer upper limit is located where the standard deviation became about 7% of the maximum value. Once we prove the phenomenon is self similar, that percentage depends neither on experiment conditions nor on time.
Our present results are also compared with the same literature data used to compare results of the 2D model in Fig. 5.7. The comparison shows a fairly nice agreement, demonstrating the validity of our 3D experimental technique.

7.4.1. Comparison with Large Eddy Simulations (LESs)

In a scaled experimental model the control of scale effects, boundary and initial conditions allows the similarity with the real phenomenon to be verified. The confidence in the results highly depends on the above mentioned issues and verifying them has to be a compulsory effort for the experimentalists. The numerical modelling, thus, can help in the validation and/or verification of a laboratory model offering prompt, less costly and repeatable results. Nevertheless the main strength of the experimental models is mostly related with their empirical and wholly physical basis. For this reason experimental runs are commonly used for the validation of numerical models, especially when an analytical solution is not available or it is too complicated to be modelled. Validating one to each-other, coupled experimental-numerical investigations might be then the most complete and reliable studies.

Motivated by those considerations, the present results have been compared to a validated LES model in order to estimate scale and wall effects, which might invalidate the results. The LES is based on the WRF meteorological model developed by Skamarock et al. in 2008. A newly developed sub-grid scheme based on the solution of the TKE equation has been added to the original code and a stretched vertical grid has been employed in order to increase the vertical resolution near the ground (Catalano and Cenedese, 2009). Initial conditions similar to those occurring during the experimental runs have been imposed. The vertical dimension of the domain is 2500 m, the spatial resolution along the horizontal is fixed at 50 m, while it ranges from 2 m to 90 m along the vertical when the stretched grid is employed. The temporal resolution is 1 s, the Brunt-Väisälä frequency for the initial stratification is $1.6 \cdot 10^{-4}$ s^{-2} and a step difference of 5 K is applied to the ground to trigger the penetrative convection.
Some runs with different boundary conditions and horizontal dimensions of the domain have been performed and their features are displayed in table 7.1.

	5km p ns	5km p	5 km w	2km p	2km w
N_x, N_y, N_z	100x100x58	100x100x58	100x100x58	40x40x58	40x40x58
Δz (m)	≈ 41	Stretched: 2 – 90	Stretched: 2 – 90	Stretched: 2 – 90	Stretched: 2 – 90
L.B.C.	periodic	periodic	wall	periodic	wall

Table 7. 1 Features of LESs. N refers to the number of grid points, Δz is the vertical resolution and L.B.C refers to the boundary conditions applied.

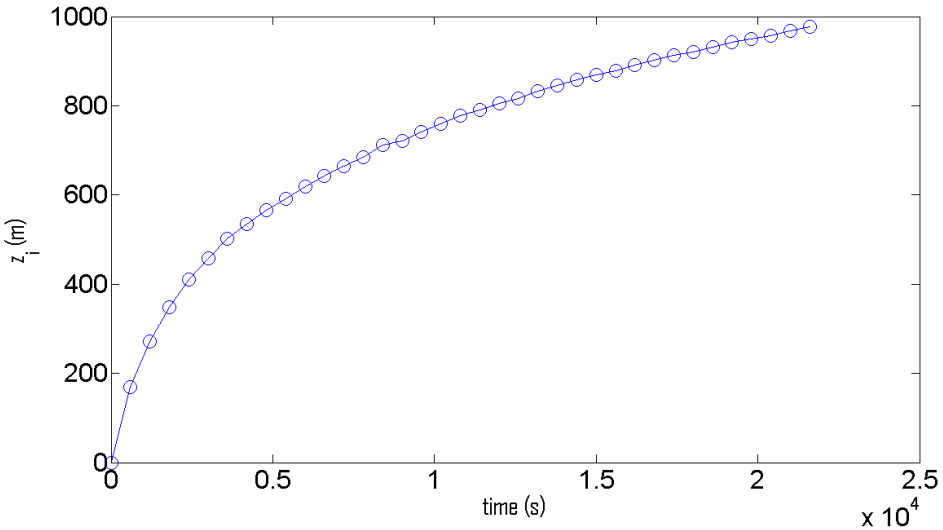

Fig 7.7. CBL growth for the 5km p simulation found using the maximum gradient method applied to the temperature profiles. The CBL height has been averaged over the x and y directions.

Testing different aspect ratio of the domain allows us to be aware of possible scale effect of the experimental test section. Since the horizontal resolution is fixed at 50 m, the three cases with 100x100x58 grid points have an aspect ratio very close to that one of the

domain inside the tank (H/L=0.5), while the aspect ratio increases up to 1.5 times for the last two simulation with 40x40x58 grid points.
In Fig. 7.7 the CBL growth found applying the maximum gradient method to the temperature profiles is plotted. Its trend is qualitatively similar to that in Fig. 5.5 and 7.5, but obviously data cannot be compared quantitatively, because of the scaling up of the numerical model. Figure 7.8 displays vector velocities mapped on the xz plane at a y=50 (middle of the domain). The values of the vertical velocities are overlapped according to a pseudo-color scale. The cores of thermals are highlighted by the highest values of positive vertical velocities, while downward plumes cover a larger area. The vertical velocity mapping from the top view allows recognizing the typical pattern of the convective cells, as shown in Fig. 7.9. Slicing the domain at different height (z/z_i=0.08, z/z_i=0.5 and z/z_i=1) one can clearly see how the cell pattern became less regular from the bottom to the top of the CBL with the highest value of vertical velocities in the middle of the convective region. At the bottom of the CBL (Fig. 7.9A) the velocities are low and the cells are nearly hexagonal in shape as in Rayleigh Benard convection experiments (Fig 2.1A). All the results presented in Fig. 7.7, 7.8 and 7.9 are related to the simulation labeled 5km p, but all the simulations gave the same results both increasing the aspect ratio and using wall boundary condition.

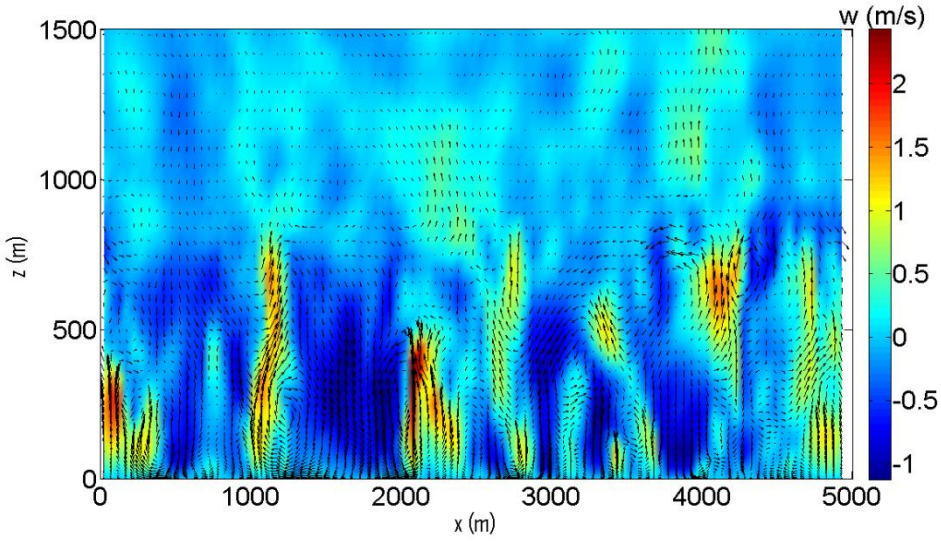

Fig. 7.8 Velocity vector mapping on the XZ plane for the 5km p simulation after 4 hours. The absolute value of the vertical velocity is overlapped in pseudo-colour scale.

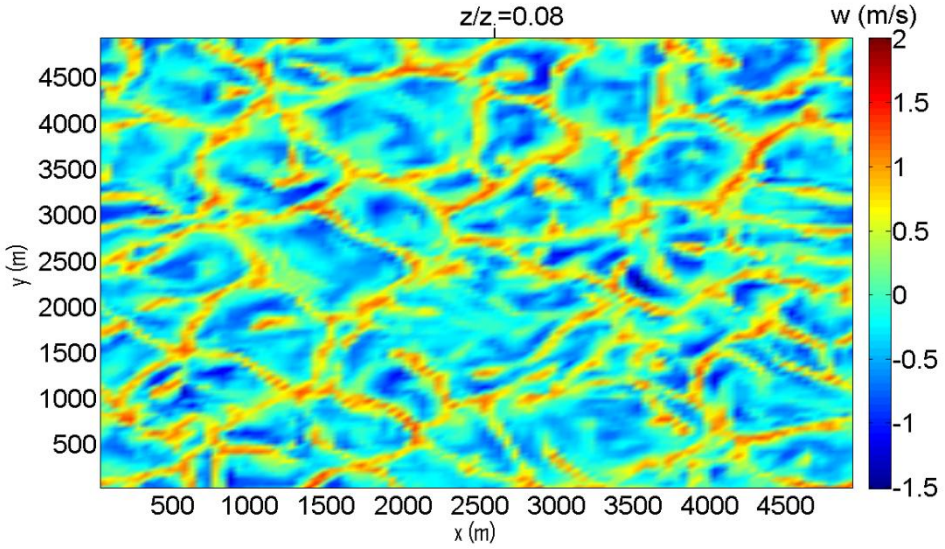
z/z_i=0.08
w (m/s)
2
1.5
1
0.5
0
-0.5
-1
-1.5
4500
4000
3500
3000
2500
2000
1500
1000
500
y (m)
500 1000 1500 2000 2500 3000 3500 4000 4500
x (m)

(A)

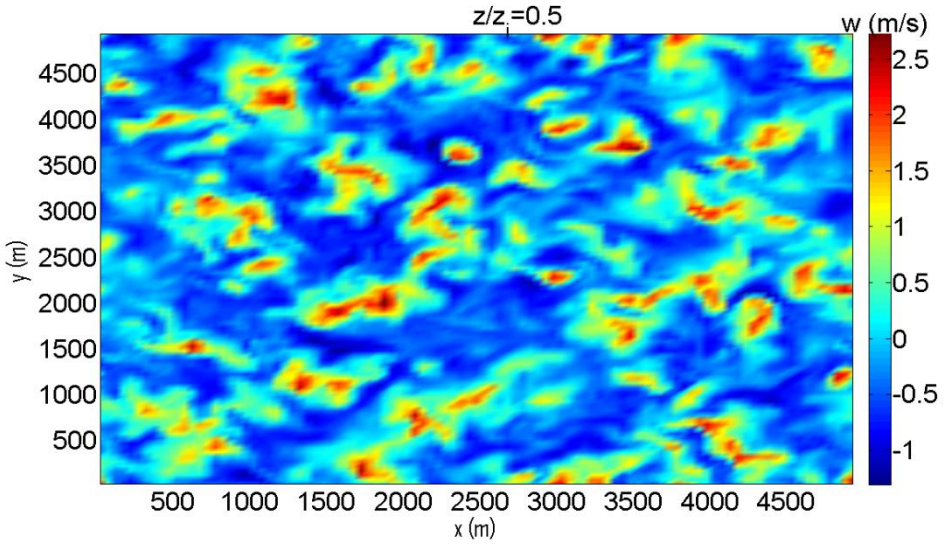
z/z_i=0.5
w (m/s)
2.5
2
1.5
1
0.5
0
-0.5
-1
4500
4000
3500
3000
2500
2000
1500
1000
500
y (m)
500 1000 1500 2000 2500 3000 3500 4000 4500
x (m)

(B)

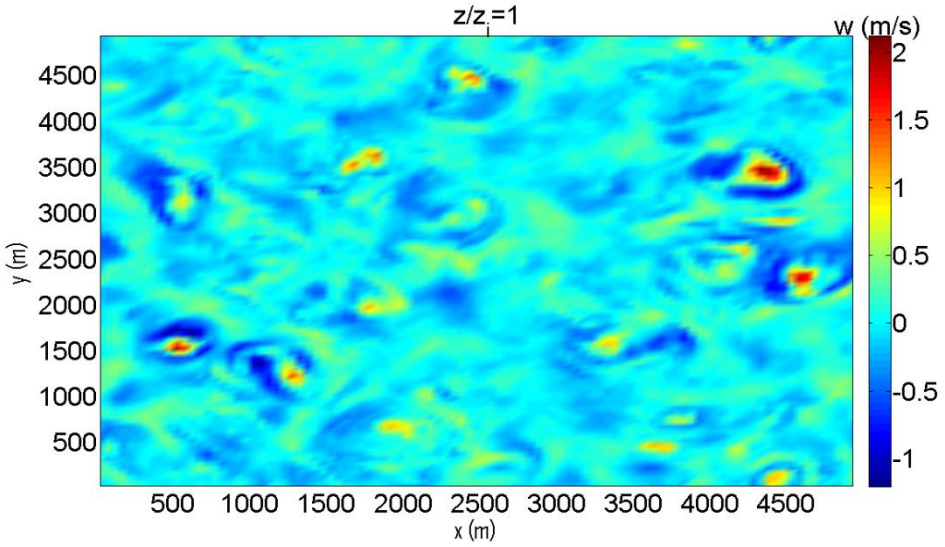

(C)

Fig 7.9. Top view of the vertical velocity mapped on a continuous pseudo-colour scale for the 5km p simulation after 4 hours. (A) XY section at z/zi=0.08. (B) XY section at z/zi=0.5. (C) XY section at z/zi=1

Finally a summary comparison is displayed in Fig. 7.10, where results of the present three-dimensional model, results of the present two-dimensional model, results of LESs in table 7.1 and literature field data (Young, 88) are overlapped. Moreover Since a fairly good agreement between all the results can be noticed, we can exclude that both scale and wall effects could invalidate our experimental results, if experimental data are not processed for too long time, as already discussed in section 5.3.

Three dimensional models (both experimental and numerical) output less dispersed profiles compared with two dimensional measurements. Plots in XZ plane are in fact real projections for 3D models, but rough approximation for 2D models as the real flow is three-dimensional.

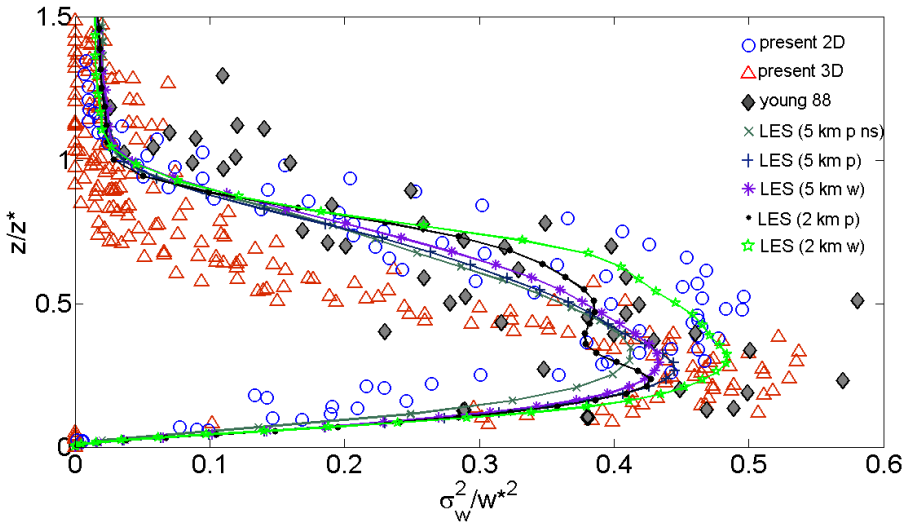

Fig. 7.10 Standard deviation of vertical velocity profiles normalized accordingly the Deardorff mixed layer similarity (Willis and Deardorff, 1974) compared with 2D model results three dimensional LES models and field data. In the legend "p" refers to periodic boundary conditions, "w" to wall boundary conditions and "ns" to non-stretched vertical discretization.

Conclusions

Shear free convection experiments in a stably stratified environment were performed in a thermally controlled convection chamber. The experimental set up was arranged in different optical configurations to ensure the two components and three components of velocity to be measured in an illuminated plane and volume respectively through different image analysis techniques with sub-pixel accuracy. Temperature measurements were simultaneously acquired using thermocouples of accuracy less than 0.1 °C. The experiments highlighted the time evolution of the convective structure characteristic spatial scales (CBL height and horizontal spacing between thermals) and the non local description of transport and mixing inside the growing CBL.

Given the great applicability of the topic in several scientific and engineering fields, large amount of experimental, theoretical and numerical investigations on CBL development in a continuously and linearly stratified fluid setting had been conducted in the past since sixties (see Fedorovich *et al.*, 2004 for a complete review). The large amount of literature, well established knowledge on the physics and the availability of large experimental data for the 2D model gave us the possibility to test dynamical similarity for our experimental runs and find a time scaling law to outline the correspondence between bench and real scales. The experimental set up is well designed and likely scales the phenomenon in nature.

Rather than bringing new insights into the physics of the CBL dynamics and entrainment, the main novelty of the present contribution covers the improvement of techniques and methods to achieve more reliable, statistically robust and likely results. The experimental effort based on image analysis techniques (mainly Feature Tracking and photogrammetric 3D-PTV) resulted suitable for reconstructing longer trajectories (always more than 10^3 trajectories longer than 20 consecutive snapshots) and analyzing larger particle density images (reliable results for more than 2000 particles in a volume of 15X15X15 cm^3 for 3D-PTV). Velocity statistics are then more robust than those from classical Particle Tracking Velocimetry.

Moreover, for the first time, a fully three-dimensional particle tracking technique has been applied to penetrative convection experiments. 3D-PTV allows a more realistic description of the velocity field, which occurs during the evolution of the convective mixed layer, than more traditional 2D techniques. Furthermore, photogrammetric 3D-PTV rather than "scanning" 3D-PTV (Moroni and Cushman, 2001) results in more

accuracy when the tracer particle density is high, because particles may be tracked directly in the 3D space rather than through matching of 2D projections.

Sensitivity tests conducted on the matching algorithm proved that the calibration accuracy is fundamental to obtain the correct matching and particle tracking; small errors in calibration parameters or neglecting water refraction effects reduce matching performance. On the other hand, accuracy less than 1 pixel was reached with our calibration procedure ensuring good results in the matching procedure. Tests on synthetic data demonstrated a multi-choice strategy with a 3 camera arrangement is the best solution for matching data. It is less sensitive to errors in the calibration data set when both the percentage of correctly matched triplets and the number of outputs of the algorithm were considered.

Original and cross-validating methods to compute the CBL height and horizontal scale of thermals were applied based on temperature, velocity and fluorescence imaging. The spatial covariance of the velocity field, providing the plume horizontal spacing, allows the spatial extension of the mixed region to be determined. Dome characteristic vertical dimension is of the same order of magnitude as the mixing layer height, while their horizontal dimension becomes similar to the vertical one at the end of the experiment when the structure dimensions are comparable to the test section side and border effects are not negligible anymore.

The mixing layer growth was computed by exploiting both temperature and velocity data. Outputs were then compared to more classical methods as the zero-order mixed-layer model and the zero-heat flux level method (Weill et al., 80). The accuracy of our methods was computed as well.

Present results, normalized accordingly to the Deardorff similarity for free convection (1970), were compared with literature data and LES meteorological models (Catalano et al., 2009). Outcomes from different experimental configurations, literature and LES models are in fairly good agreement.

The comparison with literature data at real scale demonstrates the validity of our experimental task and its applicability for the study of the real atmospheric boundary layer and its monitoring for environmental purposes. On the other hand the agreement with LES models at different boundary conditions and domain aspect ratios proves that both scale and border effects of the experimental model are negligible if data are not processed for too long time.

References

Becker J, Bosemann W, Bopp R (1999) Photogrammetric methods applied to fluid motion within a fluid matrix. Meas. Sci. Technol. 10: 914-920.

Bendat, J. S., and Piersol, A.G., *Random data analysis and measurement procedures*, 3rd ed., pp, John Wiley and sons, Inc., USA, 374-376, 2000.

Catalano, F., A. Cenedese, High resolution numerical modeling of thermally driven slope winds in a valley with strong capping, submitted to J. *Appl. Meteor. Clim*., 2009.

Cenedese, A., and Querzoli, G., A laboratory model of turbulent convection in the atmospheric boundary layer, *Atmospheric Environment*, vol. 28, no. 11, pp. 1901-1923, 1994.

Cenedese A., and Querzoli G., Lagrangian statistics and transilient matrix measurements by PTV in a convective boundary layer, *Meas. Sci. Technol,* vol. 8, pp.1553, 1997.

Chang T, Taterson G (1983) Application of image processing to the analysis of three-dimensional flow fields. Opt Eng 23:283–287.

Cowen E, Monismith S (1997) A hybrid digital particle-tracking velocimetry technique. Exp in Fluids 22:199–211.

Deardorff, J.W., Willis, G.E., and Lilly, D.K., Laboratory investigation of non-steady penetrative convection, *J. Fluid Mech.*, vol. 32, no1, pp 7-31, 1969.

Deardorff, J.W., Convective velocity and temperature scales for the unstable planetary boundary layer and for Rayleigh convection, *J. Atmos. Sci,* vol.27, pp.1211-1213, 1970.

Deardorff, J.W., and Willis, G.E., Further results from a laboratory model of the convective planetary boundary layer, *Boundary-Layer Met,* vol. 35, pp 205-236, 1985.

Di Giuseppe E, Funiciello F, Moroni M (2009) Investigating subduction mechanism through image analysis technique. (in preparation).

Doh DH, Hwang TG, Saga T (2004) 3D-PTV measurements of the wake of a sphere. Meas. Sci. Technol. 15: 1059-1066.

Dore, V., Moroni, M., Le Menach, M., and Cenedese, A., Penetrative Convection in Stratified Fluids Through 3D-PTV, *Exp. in Fluids*, Vol.47, Issue 4 (2009), 811-825, DOI:10.1007/S00348-009-0716-4.

Dore V., Moroni M. and Cenedese A. (in press). Quantifying Mixing in a Convective Boundary Layer, *Heat Transfer Engineering*, ISSN: 0145-7632

Fedorovich, E:, and Conzemius R., Convective entrainment into a shear-free, linearly stratified atmosphere: bulk models reevaluated through Large Eddy Simulations, *J. Atmos. Sci*., vol.61, pp. 281-295, 2004.

Guezennec YG, Brodkey RS, Trigui N, Kent JC (1994) Algorithms for fully automated three-dimensional Particle Tracking Velocimetry. Exp. in Fluids 17: 209-219

Haynes PH, Shuckburg EF (2000) Effective diffusivity as a diagnostic of atmospheric transport. Part II: troposphere and lower stratosphere. J. Geophys. Res. 105:22795-22810.

Haynes, P. H., Transport and mixing in the atmosphere, *Proc. Of 21st ICTAM '04 congress*, August 15-21 2004, Warsaw, Dordrecht, Kluwer Academic Publishers.

Heikkila J, Silven O (1997) A Four Camera Calibration Procedure with Implicit Image Correction. In Proceedings of the 1997 Conference on Computer Vision and Pattern Recognition (CVPR '97).

Hinsch KD, Hinrich H (1996) Three-dimensional Particle Velocimetry. In: Dracos Th. (ed.) Three-Dimensional Velocity and Vorticity Measuring and Image Analysis Technique, Kluwer Academic Publishers.

Imberger, J., and Ivey, G.N., On the Nature of Turbulence in a Stratified Fluid. Part II: Application to Lakes, *Journal of Physical Oceanography*, vol.21, pp. 659-680, 1991.

Kasagi N, Nishino K (1990) Probing Turbulence with Three-Dimensional Particle Tracking Velocimetry. In: Proceedings of International Symposium on Engineering Turbulence – Methods and Measurements.

Kato, H., and Phillips, O.M., On the penetration of a turbulent layer into stratified fluid, *J. Fluid Mech,* vol. 37, no. 4, pp.643, 1969.

Kieft RN, Schreel KRAM, Van der Plas GAJ, Rindt CCM (2002) The application of a 3D PTV algorithm to a mixed convection flow. Exp in Fluids 33: 603–611.

Lenschow, D. H., Model of the height variation of the turbulence kinetic budget in the unstable boundary layer, *J. Atmos. Sci*., vol.31, pp 465-474, 1974.

Lenschow, D. H., Wyngaard, J.C., and Pennel , W.T., Mean-field and second moment budgets in a baroclinic, convective boundary layer, *J. Atmosl. Sci*., vol. 31, pp 465-464, 1980.

Maas H (1992) Complexity analysis for the establishment of image correspondences of dense spatial target fields. In: International Archives of Photogrammetry and Remote Sensing, XXIX B5: 102-107

Maas H, Gruen A, Papantoniou D (1993) Particle-tracking velocimetry in three-dimensional flows. Exp in Fluids 15:133–146.

Malik N, Dracos T Papantoniou D (1993) Particle Tracking in three-dimensional turbulent flows - Part II: Particle tracking. Experiments in Fluids 15:279-294.

Miozzi, M., Particle Image Velocimetry using Feature Tracking and Delauny Tessellation, *Proc. 12th International Symposium Application of laser techniques to fluid mechanics*, Lisbon (Portugal), 2004.

Miozzi, M., Jacob, B., Olivieri A., Performances of Feature Tracking in turbulent boundary layer investigation, *Exp. in Fluids*, vol. 45, no. 4, pp. , 547-780, 2008

Moroni M, Cushman JH (2001) Three-Dimensional Particle Tracking Velocimetry Studies of the Transition from Pore Dispersion to Fickian Dispersion for Homogeneous Porous Media. Water Resour. Res 37(4): 873-884.

Moroni, M., and Cenedese, A., Comparison among Feature Tracking and More Consolidated Velocimetry Image Analysis Techniques in a Fully Developed Turbulent Channel Flow, *Measurement Science and Technology* , vol.16, pp.2307-2322, 2005

Moroni, M., and Cenedese, A., Penetrative convection in stratified fluids: velocity measurements by image analysis techniques, *Nonlinear process in Geophysics*, vol.13, pp. 353-363, 2006.

Moroni M, Cushman JH, Cenedese A (2009) Application of Photogrammetric 3D-PTV Technique to Track Particles in Porous Media. To appear in Transport in Porous Media.

Querzoli G., A Lagrangian study of particle dispersion in the unstable boundary layer. *Atmospheric Environment*, vol. 30, no.16, pp. 2821, 1996

Skamarock, W. C., J. B. Klemp, J. Dudhia, D. O. Gill, D. M. Barker, M., G. Duda, X.-Y Huang, W. Wang, J. G Powers, A description of the advanced research WRF version 3.NCAR/TN-475, 125 pp, 2008.

Stuer H, Maas HG, Virant M, Becker J (1999) A volumetric 3D measurement tool for velocity field diagnostic in microgravity experiments. Meas. Sci. Technol. 10: 904-913.

Stull, R.B., Internal gravity waves generated by penetrative convection, *J. Atmos. Sci*., vol.33., pp 1279-1286, 1976.

Stull, R.B. and Driedonks, A.G.M., Application on the transilent turbulent parameterization to atmospheric boundary layer simulations, *Boundary Layer Meteorol.* , 40, pp 209-239,1987

Stull, R.B., *An Introduction to Boundary Layer Meteorology*, Kluwer, Dordrecht, 1988.

Stull, *R. B.*, Review of transilient turbulence theory and nonlocal mixing. Bound.-Layer Meteor., 62, pp 21-96, *1993*

Sullivan, P.P, Moeng, CH., Stevens, B., Lenshow, D.H., and Mayor S. D., Structure of the entrainment zone capping the convective atmospheric boundary layer, *J. Atmos. Sci*., vol.55.pp 3042-3064, 1988.

Suzuki Y, Ikenoya M, Kasagi N (2000) Simultaneous measurement of fluid and dispersed phases in a particle-laden turbulent channel flow with the aid of 3-D PTV. Exp in Fluids 29:185-193.

Weill, A., Klapisz, C., Strauss, B., Budin, F., and Jaupart, C., Measuring heat flux and structure functions of temperature fluctuation with an acoustic doppler sodar, *J. Appl. Meteor.,* vol. 19, pp. 199-205, 1980.

Willert CE, Gharib M (1992) Three-dimensional particle imaging with a single camera. Exp. in Fluids 12: 353-358

Willis GE, and Deardorff JW (1974) A laboratory model of the unstable planetary boundary layer. J. Atmos. Sci. 31:297-1307.

Willneff J, Gruen A (2002) A new spatio-temporal matching algorithm for 3D-Particle Tracking Velocimetry. 9th International Symposium on Transport Phenomena and Dynamics of Rotating Machinery. Honolulu, Hawaii (USA), February 10-14.

Young, G.S: Turbulence structures of the convective boundary layer. Part I: variability of normalized turbulence statistics, *J. Atmos. Sci*., vol.45, pp 719-726, 1988.

Zhang J, Tao B, Katz J (1997) Turbulent flow measurement in a square duct with hybrid holographic PIV. Exp. in Fluids 23: 373–381

Appendix A

Least Square Estimation for Photogrammetric Equations

The least square estimation is well-known when the relation among "observations" and "unknowns" is linear. In fact, we have a system of linear equations:

$$l_m = a_{m1}x_1 + a_{m2}x_2 + \ldots + a_{mu}x_u = a_{mk}x_k \qquad (A.1)$$

where
x_k are unknowns;
l_m are the observations;
a_{mk} are coefficients.

If the number of observations is equal to u, then we have a system of u linear equations to determine u unknowns x_k. The solution of the system (in matrices) $\mathbf{l = Ax}$ is $\mathbf{x = A^{-1}l}$. If the number of observations is n, where n>u, as it should be to check the observations and to increase the accurateness of the unknowns determined, the problem of compensation arises. It can be solved by forcing the sum of the square of the corrections **v** to be minimum. Let us rewrite the system $\mathbf{l = Ax}$ in the form of "observation equations"

$$\mathbf{v} = \mathbf{A\hat{x}} - \mathbf{l}$$

The unknown x_k can be obtained forcing the minimum condition:

$$\mathbf{v}^T\mathbf{v} = \min = (\mathbf{A\hat{x}} - \mathbf{l})^T(\mathbf{A\hat{x}} - \mathbf{l}) = \hat{\mathbf{x}}^T\mathbf{A}^T\mathbf{A\hat{x}} - 2\mathbf{l}^T\mathbf{A\hat{x}} + \mathbf{l}^T\mathbf{l}$$

The solution is:

$$\frac{\partial(\mathbf{v}^T\mathbf{v})}{\partial\hat{\mathbf{x}}} = 2\hat{\mathbf{x}}^T\mathbf{A}^T\mathbf{A} - 2\mathbf{l}^T\mathbf{A} = 0$$

$$\hat{\mathbf{x}} = (\mathbf{A}^T\mathbf{A})^{-1}\mathbf{A}^T\mathbf{l} \quad (A.2)$$

The matrix $(\mathbf{A}^T\mathbf{A})$ is called matrix of "normal equations" (or normal matrix); the matrix **A** is called matrix of the "observation equations" (or draw matrix).

It stands to reason that equations of photogrammetry (eqs 4.1 and 4.2) describe a non-linear relation between coordinates in image plane (observations) and calibration parameters (unknowns); thus, in order to solve the calibration problem we need to extend the least square compensation method described above to a more general non-linear system as:

$$\overline{l_m} = f_m(x_1, x_2, \ldots, x_u) \qquad \text{(A.3)}$$

Since the compensation algorithm applies to linear equations, a Taylor expansion of (A.3) is required, with starting values $x_1^0, x_2^0, \ldots, x_u^0$:

$$\overline{l_m} = f_m(x_1^0, x_2^0, \ldots, x_u^0) + \left(\frac{\partial f_m}{\partial x_1}\right)^0 dx_1 + \left(\frac{\partial f_m}{\partial x_2}\right)^0 dx_2 + \ldots + \left(\frac{\partial f_m}{\partial x_u}\right)^0 dx_u \quad \text{(A.4)}$$

where the partial derivatives are computed at the approximate values $x_1^0, x_2^0, \ldots, x_u^0$.

Comparing (A.4) and (A.1), the following correspondences can be highlighted:

$$a_{mk} \rightarrow \left(\frac{\partial f_m}{\partial x_k}\right)^0$$

$$l_m \rightarrow \bar{l}_m - f_m(x_1^0, x_2^0, \ldots, x_u^0)$$

$$x_k \rightarrow dx_k$$

From the above it follows that the indirect observation compensation method coupled with the least squares method requires equations 4.1 and 4.2 to be partially derived:

$$\frac{\partial \xi}{\partial X_0} = -\frac{c}{N^2}(r_{13}Z_x - r_{11}N) = a_2 \qquad \text{(A.5)}$$

$$\frac{\partial \eta}{\partial X_0} = -\frac{c}{N^2}(r_{13}Z_y - r_{12}N) = b_2 \qquad \text{(A.6)}$$

$$\frac{\partial \xi}{\partial Y_0} = -\frac{c}{N^2}(r_{23}Z_x - r_{21}N) = a_3 \qquad \text{(A.7)}$$

$$\frac{\partial \eta}{\partial Y_0} = -\frac{c}{N^2}(r_{23}Z_y - r_{22}N) = b_3 \qquad \text{(A.8)}$$

$$\frac{\partial \xi}{\partial Z_0} = -\frac{c}{N^2}(r_{33}Z_x - r_{31}N) = a_4 \qquad \text{(A.9)}$$

$$\frac{\partial \eta}{\partial Z_0} = -\frac{c}{N^2}(r_{33}Z_y - r_{32}N) = b_4 \qquad \text{(A.10)}$$

$$\frac{\partial \xi}{\partial \omega} = -\frac{c}{N}\left\{\left[(Y - Y_0)r_{33} - (Z - Z_0)r_{23}\right]\frac{Z_x}{N} - (Y - Y_0)r_{31} + (Z - Z_0)r_{21}\right\} \qquad \text{(A.11)}$$

$$\frac{\partial\eta}{\partial\omega} = -\frac{c}{N}\left\{\left[(Y-Y_0)r_{33}-(Z-Z_0)r_{23}\right]\frac{Z_y}{N}-(Y-Y_0)r_{32}+(Z-Z_0)r_{22}\right\} \qquad \text{(A.12)}$$

$$\frac{\partial\xi}{\partial\varphi} = \frac{c}{N}\left[\left(Z_x\cos\kappa - Z_y\sin\kappa\right)\frac{Z_x}{N}+N\cos\kappa\right] \qquad \text{(A.13)} \qquad \frac{\partial\xi}{\partial\kappa} = -\frac{c}{N}Z_y \qquad \text{(A.14)} \qquad \frac{\partial\xi}{\partial c} = -\frac{Z_x}{N} = a_\xi \qquad \text{(A.15)}$$

$$\frac{\partial\eta}{\partial\varphi} = \frac{c}{N}\left[\left(Z_x\cos\kappa - Z_y\sin\kappa\right)\frac{Z_y}{N}+N\sin\kappa\right] \qquad \text{(A.16)} \qquad \frac{\partial\eta}{\partial\kappa} = \frac{c}{N}Z_x \qquad \text{(A.17)} \qquad \frac{\partial\eta}{\partial c} = -\frac{Z_y}{N} = b_\xi \qquad \text{(A.18)}$$

Each point P_i of unknown or known coordinates (X_i, Y_i, Z_i) and known image coordinates $(\bar{\xi}_i, \bar{\eta}_i)$, provides an equation

$$\begin{aligned} v_{\xi i} = {} & \left(\frac{\partial\xi}{\partial X_0}\right)^0 dX_0 + \left(\frac{\partial\xi}{\partial Y_0}\right)^0 dY_0 + \left(\frac{\partial\xi}{\partial Z_0}\right)^0 dZ_0 + \left(\frac{\partial\xi}{\partial c}\right)^0 dc + \left(\frac{\partial\xi}{\partial\omega}\right)^0 d\omega + \\ & \left(\frac{\partial\xi}{\partial\varphi}\right)^0 d\varphi + \left(\frac{\partial\xi}{\partial\kappa}\right)^0 d\kappa - (\bar{\xi}_{ij} - \bar{\xi}_{ij}^0) \qquad \text{(A.19)} \\ v_{\eta i} = {} & \ldots \quad \text{(analogous)} \end{aligned}$$

Equations (A.19) corresponds to (A.4). The partial derivatives $(\,)^0$ are computed for approximate values of the unknown. $\bar{\xi}_{ij}^0$ and $\bar{\eta}_{ij}^0$ are the approximate coordinates computed by (4.1) and (4.2).